From time-lapse seismic inversion to history matching of water flooded oil reservoirs

From time-lapse seismic inversion to history matching of water flooded oil reservoirs

PROEFSCHRIFT

ter verkrijging van de graad van doctor
aan de Technische Universiteit Delft,
op gezag van de Rector Magnificus prof.ir. K.C.A.M. Luyben,
voorzitter van het College voor Promoties,
in het openbaar te verdedigen op 10 december om 12:30 uur

door Mario TRANI

Master of Geological Science from "La Sapienza" University of Rome, Italïe
geboren te Latina, Italïe.

Dit proefschrift is goedgekeurd door de promotor:
Prof. Dr. Ir. R.J. Arts

Samenstelling promotiecommissie:

Rector Magnificus,	TUD, voorzitter
Prof. Dr. Ir. R. J. Arts,	TUD & TNO, promotor
Prof. Dr. Ir. J. T. Fokkema,	TUD
Prof. Dr. M. Landrø,	NTNU, Trondheim, Noorwegen
Prof. Dr. Ir. J. D. Jansen,	TUD
Prof. Dr. Ir. A. W. Heemink,	TUD
Prof. Ir. C. P. J. W. van Kruijsdijk,	TUD & Shell
Dr. Ir. O. Leeuwenburgh,	TNO

This research was carried out within the context of the Integrated Systems Approach to Petroleum Production (ISAPP) knowledge centre. ISAPP is a joint project between Delft University of Technology (TU Delft), Shell International Exploration and Production (SIEP), and the Dutch Organization for Applied Scientific Research (TNO).

ISBN 978-94-6203-211-8

Printed in the Netherlands by: CPI Wöhrmann Print Service, Zutphen

Contents

Chapter 1

Introduction

The robust worldwide economic growth is progressively leading to a significant boost in the energy consumption (IEO, 2011). As a consequence, the demand for fossil fuels, by far the first energy source, is expected to increase. The oil exploration and production (E&P) industry is trying to keep up with this growing demand, leading to the raise in crude oil prices seen in the last years.

1.1 Oil production and recovery

The constantly increasing energy demand worldwide in combination with the decrease in easily accessible fossil fuel resources has stimulated a.o. research and development to the optimization of hydrocarbon recovery from existing reservoirs over the last decade. Typically for the production of oil reservoirs, three stages of recovery, generally referred to as primary, secondary and tertiary recovery, can be distinguished.
During primary recovery the reservoir drive consists of only the natural reservoir pressure forcing the oil to the surface through the production wells. With this approach the so-called recovery factor is in (worldwide) average lower than 15% (Dake, 1978). Secondary recovery is often applied to improve this factor by artificially induced processes. When the driving natural reservoir pressure drops below a certain threshold and the production becomes uneconomical, the secondary recovery stage starts, in which external energy is supplied into the system by injecting gas or water (waterflooding) in the reservoir. In particular, waterflooding is by far the most successful and widely applied method for improved oil recovery, increasing the recovery up to several tens of percent (Jansen *et al.*, 2008). Ultimately, when secondary recovery is not sufficient to maintain the appropriate production level, ter-

tiary oil recovery techniques are considered. These methods aim specifically at raising the mobility of the oil. This can be achieved either by decreasing the viscosity through an increase of the temperature (thermally enhanced oil recovery), through gas injection (mostly CO_2), or through a reduction of the surface tension of the left heavy oil (microbial or chemical injection). In this thesis the main focus will be on improving the characterization of the secondary recovery process using both production data and time-lapse seismic data.

1.2 The value of 4D seismic in oil production

Oil is produced from the pores or fractures in reservoir rocks (mostly sandstones or limestones) situated at depths ranging from a few hundred meters up to a few thousands of meters. In general, the deeper the reservoir, the higher the pressure and temperature due to the weight of the overlying rock. A reservoir can be considered either as a frame of small mineral grains with open pore space in between (siliciclastic or sandstone reservoirs), or as an ensemble of rigid rock blocks divided by numerous fracture systems (carbonatic or limestone reservoirs) and combinations thereof. Our focus will be mainly on sandstone reservoirs, though most of the methods can easily be applied to limestones as well.
Most rocks in the subsurface are saturated with water, of which the salinity tends to increase with depth. In a reservoir rock hydrocarbons have migrated due to buoyancy forces from deeper source rocks over geological times into the porespace and accumulated there due to the presence of an impermeable caprock above it. Therefore the fluids present in the pores/fractures of these rocks are often a mixture of brine, hydrocarbons and non-hydrocarbon gasses. Each of these components influences the bulk properties such as compressibility and density of the rock differently. Since seismic data are sensitive exactly to those two bulk properties, in principle one can learn more about the pore content from seismic data.
A drawback is, that the pore content is not the only parameter influencing the bulk properties and hence the seismic response. Other parameters like texture, cementation, lithology, pore size, pore shape, effective stress, and temperature do so as well and the ensemble of all these parameters determines the final rock properties in terms of bulk density and compressibility.
However, changes in these bulk properties as a consequence of hydrocarbon production are essentially induced by changes in saturation and pore pressure, whereas the other parameters can in most cases be considered more or less stable. This makes time-lapse seismic data appealing for monitoring the

effects of fluid flow in the reservoir.
The repetition of seismic surveys (time-lapse or 4D seismic), in order to detect short-term, human related changes in the reservoir, was introduced in the late 1980's (Greaves & Fulp, 1987), and it represents a key instrument for reservoir characterization. In fact, during the secondary recovery process of waterflooding, one can imagine that water "pushes" the oil towards the producing wells causing a change in reservoir saturation and pressure along the way. The consequence is a change in compressibilities and densities of the reservoir rocks. With time-lapse seismic data it is possible to measure those changes and to identify the areas where those changes occur. Time-lapse seismic surveys were (and actually still are) essentially used to qualitatively track migration fronts and bypassed zones. Developments over the last decade with a drastic improvement in acquisition and processing techniques, allow for a more quantitative interpretation of time-lapse seismic data in terms of distributions of fluids and pressures establishing a direct link to reservoir simulations (Tura & Lumley, 1999; Landrø, 2001; Trani *et al.*, 2011). Inversion of time-lapse seismic data into saturation and pressure changes requires additional knowledge in terms of rock physics relations. To link saturation changes to seismic changes (i.e. compressibility and density of a saturated rock) the Gassmann model is probably the most widely used relation (Gassmann, 1951). Alternatively direct measurements from time-lapse log data or from laboratory experiments on core data can be used to derive empirical relations. The latter is generally used to determine the effects of pore pressure changes.

1.3 Field development and reservoir management

Traditionally seismic data plays an important role in geological model building together with well log information, cores and geological knowledge. Seismic data provide both structural information (horizons, faults) and properties (such as lithologies, porosities, saturations). Both types of information have a large degree of uncertainty. Since seismic data is recorded in time, the interpretation for model building suffers from uncertainties in the time-depth conversion and the underlying velocity model. Properties are essentially derived from seismic amplitude information. These amplitudes also suffer from large uncertainties due to the complex acquisition and processing schemes required to reduce the vast amounts of seismic pre-stack data to an interpretable post-stack form. However, calibration of seismic data to well log information measured in depth and directly at the rock under in-situ conditions helps to decrease the uncertainty again. The resulting geological model

is then transformed into a reservoir flow simulation model. This step often includes upscaling, since flow simulations can be very demanding on computational power and therefore can not handle the fine gridded geological model. These reservoir flow simulations are then matched to existing production (and injection) data and, in case available, to time-lapse seismic data. The latter, as already mentioned, are often used in a qualitative manner essentially looking at the shape of time-lapse changes assumed to represent flow patterns at specific timesteps (snapshots). Finally, when a proper history match has been obtained by adjusting model parameters like the permeability, it is assumed that the proper model has been obtained. This model is then used for predicting or forecasting the future production and to determine the optimal settings at the production wells to maximize the production. Throughout this thesis we will use the term state parameters for dynamically varying properties such as pressure and saturation and model parameters or simply parameters for the (assumed) static parameters like permeability. When new data become available in time, this entire workflow has to be followed again in order to update the model. Major drawbacks of this process are, that generally uncertainty and non-uniqueness are not well handled and that it is very cumbersome to update models with latest data.
These drawbacks have resulted in a new integrated approach based on methods developed for oceanography and weather forecasting, where also large models have to be updated continuously with new information and measurements taking uncertainties into account. In this methodology no longer a single best model is used, but an ensemble of realizations representing the true reservoir. By using multiple realizations throughout the whole process, a better estimate of the uncertainties and the non-uniqueness can be obtained. The following paragraphs summarize developments in this field. In this thesis the main focus is on how to optimally use time-lapse seismic data in this workflow.

1.4 Closed-loop control

In reservoir management we try to optimize the production of a hydrocarbon field, requiring representations or models of the reservoir. In the traditional approach, reservoir models are revised only every few years and plans are based on the most recent model. Jansen *et al.* (2005) presented reservoir management as a model-based, closed-loop controlled activity, in which reservoir states and parameters are continuously estimated as new measurements become available. Subsequently, the updated model is used to calculate new settings that are expected to optimize the reservoir production.

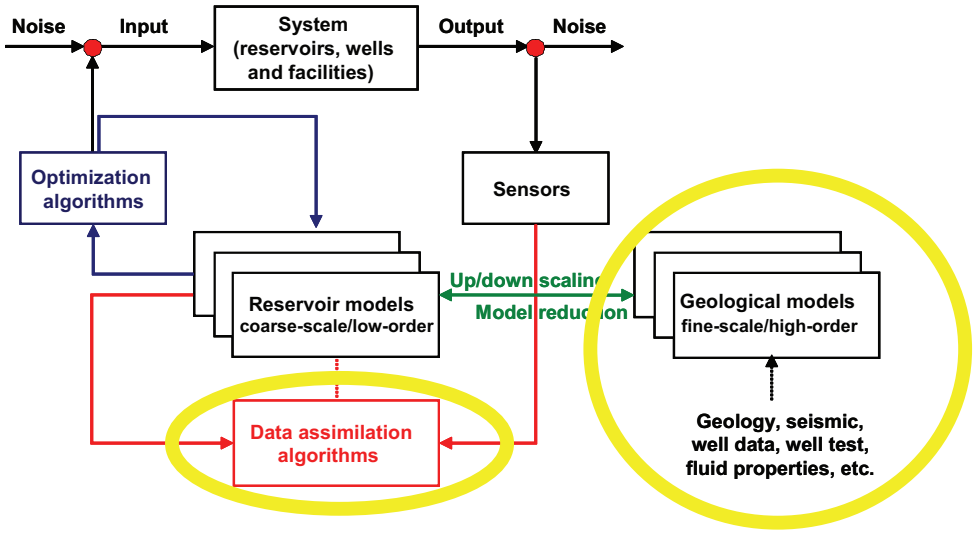

Figure 1.1: *Closed-loop reservoir management as presented in Jansen* et al. *(2005). The traditional workflow including the system and the measurements (top part of the picture) is closed by a data assimilation (red) and by an optimization loop (blue). The yellow circles indicate the contribution of this thesis with respect to the loop, as described in section 1.6*

.

The main idea of the closed-loop, integrated approach (often called 'closed-loop' or 'real-time' reservoir management) is explained in figure 1.1. The system at the top of the picture (in black) consists of one or more reservoirs, wells and facilities, the state of which is estimated from the measured data available. The associated uncertainty is related to the limitations or even lack of measurements and observations and to the uncertainties in measurements. However, this open process can be closed by two smaller loops: the data assimilation loop (in red) and the optimization loop (in blue). In the red loop, system models based on data from different sources are updated using the available measurements in order to decrease the uncertainty on state and parameters (see next section for a detailed description of the process). In the blue loop, the updated model (or models, if the assimilation process is based on multiple realizations) is used to optimize hydrocarbon production by changing production strategies: the reservoir performance can be maximized by manipulating the well rates or pressures (Jansen *et al.*, 2009b; Van den Hof *et al.*, 2009).
It has been demonstrated (Nævdal *et al.*, 2006; Sarma *et al.*, 2006; Jansen *et al.*, 2009a) that closed-loop reservoir management has the potential to con-

siderably improve the reservoir performance, as with frequent updates the estimated models become more reliable and are able to predict the future behavior with fairly high accuracy. In particular, with the Brugge benchmark (Peters *et al.*, 2009) three improvements can be observed compared to a traditional reservoir management approach:

- Models become more reliable with more frequent updates;
- Uncertainty is taken into account properly;
- The improved history match seems to lead to better forecasts.

.
With respect to the innovative integrated approach illustrated in figure 1.1, the contribution of this thesis can be split into two parts: the first part of this study, as mentioned in section 1.2, is dedicated to time-lapse seismic inversion and therefore to the improvement of reservoir characterization (left yellow circle in the picture); the second part of the thesis is focused on an innovative manner to improve the use of production and seismic observations in the automated history matching process (lower yellow ellipse).

1.5 Data Assimilation and History match

This section provides a more detailed description of the data assimilation loop in order to understand the role of the thesis with respect to the closed-loop framework.
In reservoir engineering the process of data assimilation is often referred to as 'History Matching' (HM). This name is explained by the objective of the process itself: obtaining a model that fits historical observations.
Originally HM was performed manually, using good reservoir and production engineering experience. Manual HM was done following a workflow which has been developed through years of experience and adopted within most oil companies.
A good description of this workflow is given in Williams *et al.* (1998). The first step of the workflow is to obtain a good match of the pressure field, as it represents the reservoir energy. This can typically be done by tuning a number of key parameters such as: aquifer pore volume factors, aquifer transmissibility and size, permeability multipliers, rock compressibilities and the ratio between horizontal and vertical permeabilities. Once a good match with the global pressure behavior is achieved, pressures at individual wells have to be matched. This match can be obtained by adjusting the properties

of individual flow units and layers, followed by the adjustment of well properties or properties in near well areas.
Once the pressure match is satisfactory, the production rates (oil and water rates or water cuts) are matched. In Williams *et al.* (1998) it is suggested that relative permeability curves can be tuned at this stage, as this would help in matching well rates without affecting much the already matched reservoir energy. If tuning relative permeabilities is not enough, further improvement in matching saturations can be obtained by adjusting locally the vertical transmissibilities, and horizontal permeabilities.
It is quite obvious that achieving a good HM for large models with many wells is a major effort (Agarwal *et al.*, 2000). A serious drawback of a manual HM is, that it only results in a single solution, lacking information on the associated uncertainty.
With the evolution of faster computational capabilities, HM has become progressively computer-assisted (automated HM or AHM) and it has been more and more approached as an 'inverse' problem. An inverse problem is a general framework used to deduce information about a physical system from observed data (adapted from Wikipedia). The name 'inverse' is due to the nature of the approach, typically reversed to what is called a 'forward' problem. A forward problem, in fact, consists of predicting observations from given conditions.
In the AHM the results from a numerical reservoir prediction model (the forecast) are combined with observations of the current (and possibly, past) reservoir state to produce an updated description of the reservoir. Essentially, the analysis step tries to balance the uncertainties in the data and in the forecast, which are expressed in terms of mean and standard deviation. In order to represent the pdf of the uncertainties multiple realizations are needed. The mean of the update is considered as 'the best' estimate of the current state of the system. This process, based on the measurement information is also called 'Data Assimilation'. Data Assimilation has been introduced first in environmental sciences like oceanography (Evensen, 1994; Wunsch, 1996; Bennett, 2002; Keppenne & Rienecker, 2003; Leeuwenburgh, 2007), and weather forecast (Courtier *et al.*, 1998; Lorenc, 1981; Talagrand & Courtier, 1987). Unlike in the traditional HM, where only a very limited number of predictions are made, AHM generates a large range of predictions that are updated in a consistent manner. Several model predictions, or realizations, are generated with the aim of capturing the range of possible outcomes. However, in the AHM, the multiple realizations not only describe the uncertainty at a certain time step, but they are used to propagate the uncertainty in time and reduce it when new observations become available.

Data Assimilation problems can be formulated in a Bayesian framework (Tarantola, 2005). Bayes theorem states that we can estimate the state of nature $\mathbf{A}$ given the observations $\mathbf{D}$. It reads as:

$$f(\mathbf{A}|\mathbf{D}(t_i) : i = 1, ..N_o) = f(\mathbf{D}(t_i) : i = 1, ..N_o|\mathbf{A})f(\mathbf{A})/f(\mathbf{D}(t_i) : i = 1, ..N_o) \tag{1.1}$$

$f(\mathbf{D}(t_i) : i = 1, ..N_o|\mathbf{A})$ is the conditional probability of the data given the state of nature. This term indicates how likely the measurements are, given a certain parameter. $f(\mathbf{D}(t_i) : i = 1, ..N_o)$ is the probability of the measurements and it does not depend on $\mathbf{A}$. The ratio between these two terms represents the impact of the measurements on the confidence in $\mathbf{A}$ and it is called the 'Likelihood'. $f(\mathbf{A})$ is the prior information, that is the uncertainty associated to the state $\mathbf{A}$ before the measurements are acquired. $f(\mathbf{A}|\mathbf{D}(t_i) : i = 1, ..N_o)$ is the maximum a posteriori estimate of $\mathbf{A}$ that represents the confidence in the estimated parameters after the data are acquired.
Basically Bayes theorem tries to minimize the mismatch between observed and predicted data. From Bayes theorem two main groups of data assimilation approaches have originated: variational methods, based on optimal control theory (also referred to as 'optimal methods'), and sequential methods, based on the theory of optimal statistical estimation. The first class was first introduced in meteorology (Le Dimet & Talagrand, 1985; Lewis & Derber, 1985; Courtier & Talagrand, 1987) and more recently in oceanography (Thacker & Long, 1988; Sheinbaum & Anderson, 1990; Schroter *et al.*, 1993; Moore, 1991). Statistical methods were introduced in oceanography slightly later (Ghil, 1989; Ghil & Malanotte-Rizzoli, 1991).
Variational methods start from the definition of a cost-function $\mathcal{J}$ measuring the discrepancy of the solution of the model associated to the control vector and the acquired observations (Aurox, 2006). In the cost-function the a priori information is included. These methods try to minimize the cost-function by calculating its gradient. Because of the large dimension of the model state vector, it is not possible to compute directly the gradient by using discretization methods, such as finite differences. The gradient vector is then obtained by the adjoint method (Le Dimet & Talagrand, 1985; Talagrand & Courtier, 1987). The determination of the most probable state of nature, that is the one that minimizes the cost-function, is carried out by running a descend-type optimization method. Given an initial estimation (prior information), an iterative algorithm, either conjugate gradient or Newton-type method, searches for the minimum of the cost-function.

A major disadvantage associated with optimal methods is that in case of nonlinear problems it requires several evaluations of $\mathcal{J}$, hence several integrations of the model. Furthermore, in case of non-linear problems $\mathcal{J}$ may not be convex, and it can present several local minima. The optimization algorithm may then converge to a local minimum rather than the global minimum, depending on the choice of the first estimate. A second drawback of these methods is the implementation of the adjoint model. In the minimization of $\mathcal{J}$, the transpose of the matrix containing the partial derivative of the model operator (mapping parameters to the observation space) with respect to the state vector entries is required to be known. This matrix is called the Jacobian, or 'Adjoint'. Provided full access to the code, the procedure can be quite long and cumbersome, limiting the use of these methods to small case studies.
The second type of methods consists of the sequential methods. Because of the limited applicability of variational methods, the sequential method family has received recently growing attention (see chapter 3 for detailed references). This type of methods has been proven useful for time-dependent problems where new observations are assimilated sequentially in time as they become available (Evensen, 2009). The first sequential method to be introduced was the Kalman Filter -KF- (Kalman, 1960). The method is based on the assumptions that:

1. The measurement noise is not time-dependent;
2. The model and the measurements are unbiased, and their associated noise is white;
3. The model is linear;
4. The true model error covariance is known;
5. The conditional probability is Gaussian and therefore fully described by the first two point statistics.

As can be understood from assumption 3,the KF is not suitable for nonlinear cases. Furthermore, from assumption 4 it is clear that the prior and the posterior error covariances have to be known at every assimilation step. This means that the covariance matrices, need to be stored and propagated in time; however, since those matrices have equal size as the square of the state vector, the method is not easily applicable to high dimensional models.
A derivation of the KF which overcomes those two main drawbacks of the KF is the Ensemble Kalman filter -EnKF- (Evensen, 1994). In the EnKF the

covariance matrices are propagated using sample points (ensemble) to represent the uncertainty and apply forward simulations of each of the sample points with nonlinear model equations. In the forward step of the EnKF, the model equations are applied to each of the ensemble members. The update step is computed using the form of the KF equation, but it avoids the computation and the storage of the full covariance matrices for model and measurement uncertainties, as the error covariance matrices are built from the ensemble. In the EnKF, the analysis step, same as in KF, is still based on the first two-points statistics of the distributions (although the model variable distributions are finite), limiting the performance of the filter when the Gaussian assumption is strongly violated.
Because of the mentioned characteristics, the EnKF is computationally feasible for large systems and is relatively simple to implement making use of existing simulators. Furthermore, the method presents other attractive features for history matching: consistent time-evolving weighting of model and data contributions based on model and measurement error covariances, flexible treatment of any kind and number of data or uncertain parameters, a large and active research community, and a rigorous theoretical basis. For these reasons the EnKF has become popular in the Data Assimilation literature and it has been chosen in this thesis to update the reservoir model.
Despite its numerous advantages, the EnKF approach presents also some disadvantages: one is that, as it is derived from the KF, it only allows linear updates and therefore it can only preserve Gaussian distributions. A second one is its inability to deal with large numbers of independent observations. Chapter 3 provides a detailed description of the EnKF and adjustments to the filter aimed at improving its performance.

In HM, the reservoir engineer is generally forced to estimate parameters for the entire reservoir model only based on the information related to sparsely distributed production data. It is obvious that the number of observations is much smaller than the number of variables to estimate. Therefore HM is generally considered as a strongly ill-posed problem (Tavassoli *et al.*, 2004). The additional information acquired from (time-lapse) seismic data can be utilized to narrow the solution space down when minimizing the misfit between gathered measurements and their forecasts from numerical models. Chapters 3, 4,5,and 6 of this thesis investigate the possibility to assimilate time-lapse seismic data, using the EnKF, in order to achieve a better constrained and more accurate reservoir model.

1.6 Research objective

In the previous sections it has been mentioned that time-lapse seismic observations, within a data assimilation framework, have the potential to reduce uncertainty on model parameters and states in order to optimize oil production in a closed-loop reservoir management approach. However, currently it remains unclear in the literature, what the optimal way of incorporating seismic data in such a scheme would be, particularly in a quantitative manner. This has lead to the following research objectives of this thesis:

Research objective:
Provide accurate estimates of changes in saturation and pore pressure induced by waterflooding with 4D seismic inversion, and investigate the possibilities to obtain an accurate model update through the assimilation of seismic measurements with the Ensemble Kalman Filter.

The first part of this thesis is focused on a time-lapse seismic inversion scheme able to provide changes in fluid saturation and pressure resulting from production/injection, with no (or minimized) bias, a necessary prerogative for observations used in the EnKF update.
In the literature numerous time-lapse pre-stack seismic inversion methods are presented -a.o. Landrø (2001); Meadows (2001)-. Although these approaches are easy to implement, in some cases they suffer from bias and poor accuracy in the estimates. The first part of this thesis aims at improving the inversion schemes, primarily by adding the information contained in the time-shift as an additional constraint.

The second part of the thesis is focused on the optimal way to assimilate with the EnKF the estimated changes in bulk properties induced by fluid flow from seismic inversion. The goal of this process is to use seismic observations to increase the accuracy in the estimate of reservoir porosity and permeability, which both strongly condition the reservoir fluid flow. A good estimate in those parameters is reflected in a reliable production forecast which is necessary for optimization processes (like infill well drilling).
This thesis investigates the assimilation of time-lapse changes in saturation and pressure, providing indicative rules-of-thumb for the implementation of the EnKF when such measurements are available. These rules-of-thumb are inferred from a covariance study performed on a 2D model with a regular well pattern. The applicability of these rules on a larger, more realistic 3D model with an irregular well placement is also tested.

Alternatively this thesis proposes a new technique based on the time re-parameterization of saturation data at the front location estimated from 4D seismic data. This approach consists of transforming saturation data at the water front in water-phase arrival times for each gridblock. These arrival times are then used for the assimilation using the EnKF. The motivation is that fluid fronts can often be detected more robustly from time-lapse seismic data than inverted saturation changes. Furthermore, using saturation data directly as observations generally violates the Gaussian assumption underlying the EnKF; instead, water-phase arrival times, with a model forecast properly approximated by a normal function are more suited for an EnKF update. Results on a 3D synthetic reservoir are promising.

1.7 Thesis outline

The outline of this thesis is as follows:

- Chapter 2, based on Trani *et al.* (2011), presents an innovative time-lapse seismic inversion method for the estimation of time-lapse changes in fluid saturation and pore pressure from the combination of changes in seismic amplitudes and compressional and shear wave time-shifts. This chapter corresponds essentially to the yellow circle in the lower right part of the closed loop in figure 1.1 (building the model). The next chapters are dedicated to the data assimilation loop (yellow circle in the lowest part of the closed-loop in figure 1.1).

- Chapter 3 gives an introduction to the Ensemble Kalman Filter, the preferred method for data assimilation selected in this thesis. Both advantages and disadvantages of this method are introduced. This chapter also includes an introduction to the EnKF localization, a procedure required for the correct functioning of the filter for the assimilation of large amounts of time-lapse seismic observations.

- The first part part of chapter 4 is dedicated to a covariance study on a synthetic 2D model, indicating the model region to take into account when applying localization for the correct assimilation of seismic measurements as provided in chapter 2. The second part of the chapter presents results from the assimilation of 4D seismic measurements with the EnKF localization performed on a 2D synthetic model.

- Chapter 5 presents a comparison between the localized and the traditional EnKF update, similar as in chapter 4, but from a larger and more realistic 3D synthetic model.

- Chapter 6, based on Trani *et al.* (2012), presents the EnKF update performed with the time-reparameterization of saturation data, an alternative approach to covariance localization. Results are performed on the same model as used in chapter 5.
- Chapter 7 provides general conclusions from this thesis and recommendations for future research.

Chapter 2

Estimation of changes in saturation and pressure from 4D seismic AVO and time-shift analysis[i]

THIS chapter presents an innovative 4D seismic inversion scheme to estimate time-lapse changes in saturation and pressure induced during reservoir waterflooding. In general, a reliable estimate of reservoir pressure and fluid saturation changes from time-lapse seismic data is difficult to obtain. Existing methods generally suffer from leakage between the estimated parameters. The presented method uses different combinations of time-lapse seismic attributes based on four equations: two expressing changes in pre-stack AVO attributes (zero-offset and gradient reflectivities), and two expressing post-stack time-shifts of compressional and shear waves as functions of production induced changes in fluid properties. The effect of using different approximations of these equations is tested on a realistic, synthetic reservoir, where seismic data have been simulated during the 30 years lifetime of a waterflooded oil reservoir.
The estimated changes in saturation and pressure, provided by 4D seismic inversion will be used in the next chapters in a broader data assimilation process to update the reservoir model with the Ensemble Kalman Filter.

[i]This chapter has been published as a journal paper in *Geophysics*, **76**(2), C1-C17 (Trani *et al.*, 2011). Note that minor changes have been introduced to make the text consistent with the other chapters of this thesis.

2.1 Introduction

Several authors have introduced various 4D seismic inversion methods to estimate changes in pore pressure and saturation, each one taking into account different seismic attributes. Tura & Lumley (1999) presented a method to map and quantify those changes utilizing P- and S-wave impedances. Rojas (2008) proposed to use the P- and S-wave velocitities ratio as an indicator of lithologies, fluid saturation and pressure changes in gas sandstones reservoirs. Landrø (2001, 1999) introduced an elegant, straightforward inversion scheme which solves for pressure and saturation changes from seismic amplitude-versus-offset (AVO) data. The method relies on the fact that those variations in dynamic properties are detectable from changes in intercept and slope of the AVO response for the top reservoir reflector; the minimally required input consists of near- and far- offset stacked data from the baseline and the monitor surveys. Meadows (2001) slightly modified Landrø's method by introducing a quadratic approximation of compressional wave velocity changes as a function of changes in saturation, and by taking variations in P- and S-waves impedances as input, instead of differences in the noise sensitive AVO attributes.
The afore mentioned methods estimate variations in fluid properties from the information given by amplitude attributes only, not taking into consideration the time-shift below the producing reservoir. Different authors have demonstrated the added value of using time-lapse differences in arrival times to map, interpret and estimate changes in reservoir properties.
Landrø *et al.* (2001) noticed a good correlation between over-pressured areas and an increase in arrival times (push-down); the time-shift analysis also gave information about the vertical distribution of the production related changes within the reservoir. Landrø (2002) proposed a way to express changes in fluid properties as a weighted linear combination of the estimation coming from changes in AVO coefficients and from changes in P- and S-waves traveltimes. Arts *et al.* (2002, 2004) used a combination of the time-shifts together with changes in seismic amplitudes, to estimate variations in saturation and the extension of the CO_2 flooded area at Sleipner. Landrø & Stammeijer (2004), Røste *et al.* (2006), Ghaderi & Landrø (2009) presented different methods to estimate reservoir thickness variations from velocity changes, using differences in seismic amplitudes and time-shifts. Tura *et al.* (2005) used a closed loop workflow in which the static and dynamic reservoir model properties were updated with the objective of matching production data, time-lapse seismic amplitudes and time-shifts.
Despite the fact that Landrø's (2001) approach (or the enhanced version)

is quite straightforward and appealing, it provides estimates with large uncertainty; in fact, Landrø's method tends to overestimate real changes in saturation and the leakage between one parameter into the other masks different fluid effects. In this study an inversion scheme is presented, based on a modified form of Landrø's equations and extended with two extra equations expressing the time-shifts induced by P- and S-wave velocity changes as a function of pressure and saturation changes. The combined instantaneous information from AVO attributes and the averaging information contained in the time-shifts reduces the uncertainty in quantifying changes in pressure and saturation and reduces leakage from one parameter into the other, all under the assumption of negligible reservoir thickness changes (compaction or swelling). The aim is to render the methodology originally proposed by Landrø more robust and accurate.
Different factors having impact on the inversion results are evaluated and quantified; this is done using a synthetic, but realistic reservoir adapted from the Brugge Field model used as a benchmark study for closed loop reservoir management (Peters *et al.*, 2009).

2.2 Review and extension of Landrø's method introducing the time-shift as a constraint

Landrø (2001) proposed an elegant procedure to express changes in seismic amplitude attributes as a function of variation in reservoir saturation and pressure. The expressions are based on the Smith and Gidlow (Smith & Gidlow, 1987) equation for the P-wave reflection coefficient as a function of the angle of incidence. The equation reads

$$R_0(\theta) = \frac{1}{2}\left(\frac{\delta\rho}{\rho} + \frac{\delta\alpha}{\alpha}\right) - \frac{2\beta^2}{\alpha^2}\left(\frac{\delta\rho}{\rho} + \frac{2\delta\beta}{\beta}\right)\sin^2(\theta) + \frac{\delta\alpha}{2\alpha}\tan^2(\theta) \quad (2.1)$$

where α, β, ρ, indicate the mean P-, S-wave velocity and density, respectively, between the two layers (the overburden and the reservoir), and $\delta\alpha$, $\delta\beta$, $\delta\rho$ the difference in the respective seismic parameters. The first term in the equation represents the zero-offset reflectivity while the latter two terms, for angles up to 30° can be grouped together; they express the dependence of the reflection coefficient as the offset increases (gradient reflectivity). The change in reflectivity is calculated by subtracting $R_0(\theta)$ (at the initial time) from the reflection calculated at the time of the monitor survey (see eqs. B.1 and B.2). The time-lapse change in zero-offset reflectivity (neglecting higher order terms

in relative changes of seismic parameters or combination of them) reads

$$\Delta R_0 = \frac{1}{2}\left(\frac{\Delta\rho}{\rho} + \frac{\Delta\alpha}{\alpha}\right) \tag{2.2}$$

and the change in gradient reflectivity reads (again neglecting higher order terms in relative changes of seismic parameters or combination of them)

$$\Delta G = -\frac{2\beta^2}{\alpha^2}\left(\frac{\Delta\rho}{\rho} + \frac{2\Delta\beta}{\beta}\right) + \frac{\Delta\alpha}{2\alpha} \tag{2.3}$$

where $\Delta\alpha/\alpha$, $\Delta\beta/\beta$, $\Delta\rho/\rho$ indicate the relative variations in P-, S-wave velocity and density, respectively. These changes can be considered as the sum of the relative changes induced by the separate effects of fluid saturation and pore pressure changes (except for density, on which the effect of pressure changes is negligible) as

$$\frac{\Delta\alpha}{\alpha} = \frac{\Delta\alpha_F}{\alpha} + \frac{\Delta\alpha_P}{\alpha}, \tag{2.4}$$

$$\frac{\Delta\beta}{\beta} = \frac{\Delta\beta_F}{\beta} + \frac{\Delta\beta_P}{\beta}, \tag{2.5}$$

$$\frac{\Delta\rho}{\rho} = \frac{\Delta\rho_F}{\rho}. \tag{2.6}$$

Using a linear expansion with respect to saturation changes and a quadratic expansion with respect to pressure changes, the relative variations in seismic properties can be written as

$$\frac{\Delta\alpha}{\alpha} \approx k_\alpha \Delta S + l_\alpha \Delta P + m_\alpha \left(\Delta P\right)^2, \tag{2.7}$$

$$\frac{\Delta\beta}{\beta} \approx k_\beta \Delta S + l_\beta \Delta P + m_\beta \left(\Delta P\right)^2, \tag{2.8}$$

$$\frac{\Delta\rho}{\rho} \approx k_\rho \Delta S. \tag{2.9}$$

Where k_α, l_α, m_α, k_β, l_β, etc. are the regression coefficients of the empirical curves which express the relative variations of the seismic parameters vs relative variation of ΔS or ΔP.
The zero-offset reflectivity, using eqs. 2.7 and 2.9, can be rewritten as

$$\Delta R_0 \approx \frac{1}{2}\left(k_\rho \Delta S + k_\alpha \Delta S + l_\alpha \Delta P + m_\alpha \left(\Delta P\right)^2\right). \tag{2.10}$$

Using eqs. 2.7 to 2.9, and assuming -after Landrø (2001)- that under fluid substitution the shear modulus remains constant (meaning that $\beta^2\rho$ is constant and therefore $(\Delta\rho_F/\rho + 2\Delta\beta_F/\beta) = 0$), the gradient reflectivity can be rewritten as

$$\Delta G \approx \frac{1}{2}\left(k_\alpha \Delta S + l_\alpha \Delta P + m_\alpha (\Delta P)^2\right) - \frac{4\beta^2}{\alpha^2}\left(l_\beta \Delta P + m_\beta (\Delta P)^2\right). \quad (2.11)$$

By solving the system of two equations containing the AVO attributes, explicit expressions for changes in saturation and pressure are found.
By using second order approximations to express relative changes of P- and S-wave velocity as functions of ΔS and ΔP -as proposed by Meadows (2001)- eqs. 2.7 and 2.8 can be, respectively, rewritten as:

$$\frac{\Delta\alpha}{\alpha} \approx j_\alpha (\Delta S)^2 + k_\alpha \Delta S + l_\alpha \Delta P + m_\alpha (\Delta P)^2, \quad (2.12)$$

$$\frac{\Delta\beta}{\beta} \approx j_\beta (\Delta S)^2 + k_\beta \Delta S + l_\beta \Delta P + m_\beta (\Delta P)^2, \quad (2.13)$$

where j_α and j_β are the second order regression coefficients of the saturation induced relative changes, respectively, of P- and S-wave velocities. Using eqs. 2.12 and 2.9, the zero-offset reflectivity becomes

$$\Delta R_0 \approx \frac{1}{2}\left(k_\rho \Delta S + j_\alpha (\Delta S)^2 + k_\alpha \Delta S + l_\alpha \Delta P + m_\alpha (\Delta P)^2\right). \quad (2.14)$$

Using eqs. 2.12 and 2.13 and again assuming no variation of the shear modulus during fluid substitution, the gradient reflectivity becomes

$$\Delta G \approx \frac{1}{2}\left(j_\alpha (\Delta S)^2 + k_\alpha \Delta S + l_\alpha \Delta P + m_\alpha (\Delta P)^2\right) - \frac{4\beta^2}{\alpha^2}\left(l_\beta \Delta P + m_\beta (\Delta P)^2\right). \quad (2.15)$$

Figure 2.1 presents the modeled relationship between relative changes in P-wave velocity and water saturation; the relationship has been calculated using a rock physics model calibrated to typical North Sea reservoir values. Initial water saturation is 0.2 potentially increasing to 0.5 as a result of production and water injection; leading to changes in water saturation (ΔS) varying between 0 and 0.3. The 'true' modeled relationship is in black and it can be approximated by a linear (as in Landrø) or by a quadratic function (as in Meadows). Figure 2.1b illustrates the relative P-wave velocity changes as a function of net pressure. The net pressure is equal to the overburden pressure minus the pore pressure with the coefficient of internal deformation

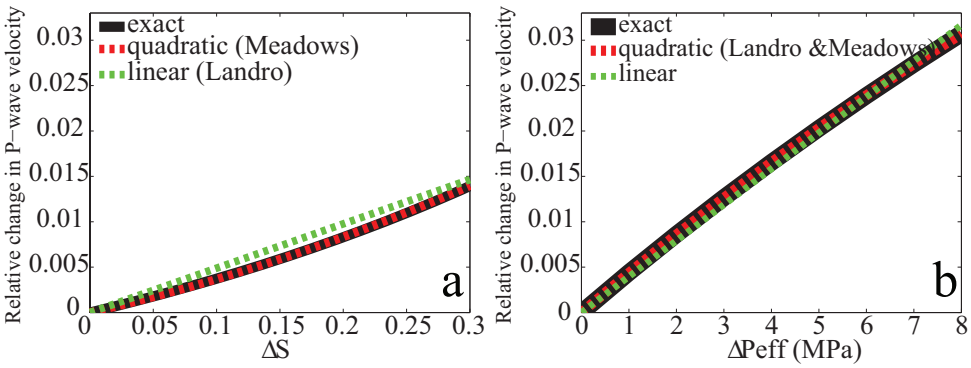

Figure 2.1: *Relative change in P-wave velocity versus change in water saturation (a) and in pressure (b) for different approximations; the black line is the truth case. A quadratic approximation (red) shows high accuracy in figure a. In plot b, the quadratic approximation (red), as Landrø proposed, overlaps with the exact curve.*

being equal to 1. Initial net pressure is 17 MPa and changes (ΔP) from 0 to + 8 MPa are expected as a consequence of production. The green and the red lines show, respectively, the linear and quadratic approximations of the 'truth' case (in black). For this case study, a quadratic function moderately improves the accuracy of the approximation of relative changes in P-wave velocity versus saturation changes; for the approximation versus differences in net pressure, minor improvements are observed, as the relative change in P-wave velocity induced by variations in pressure presents an almost linear behavior.

Despite the use of a quadratic approximation, Meadows (2001) did not solve two problems related to Landrø's method: the bias in the estimation of changes in saturation and the leakage between different parameters. In this chapter solutions to minimize these effects are proposed. The quantitative estimation of changes in dynamic properties in Landrø (2001) and in Meadows (2001) is based only on the information related to the top reservoir reflection amplitude characteristics. A way to further constrain Landrø's method (or the enhanced version) and to make it more robust is to extend it with an additional equation expressing the P-wave time-shift, induced by variations in seismic velocity, as a function of changes in pressure (ΔP) and in saturation (ΔS). This time shift reads

$$\Delta T_{pp} = -\frac{2D}{\alpha_0^r + \delta\alpha_0^r}\frac{\delta\alpha_0^r}{\alpha_0^r}. \tag{2.16}$$

where D is the reservoir thickness, α_0^r the reservoir interval velocity at the time of the baseline survey (time 0), $\delta\alpha_0^r$ the absolute change in the reservoir velocity between the times of the baseline and the monitor survey, $\delta\alpha_0^r/\alpha_0^r$ its relative change. The latter can be expressed as a function of changes in pressure and saturation (see eq. 2.12); inserting eq. 2.12 into eq. 2.16 the P-wave time-shift can be expressed as a function of ΔS and ΔP as

$$\Delta T_{pp} \approx -\frac{2D}{\alpha_0^r + \delta\alpha_0^r}\left(j_\alpha\left(\Delta S\right)^2 + k_\alpha \Delta S + l_\alpha \Delta P + m_\alpha\left(\Delta P\right)^2\right). \quad (2.17)$$

With the addition of time-shift data, expressions for ΔP and ΔS cannot be found in a simple way as presented in Landrø (2001); the non-linear, over-determined system composed of the second order approximations of change in vertical reflectivity (eq. 2.14), change in gradient reflectivity (eq. 2.15) and P-wave time-shift (eq. 2.17), is solved with the Gauss-Newton algorithm (see Appendix A).
If shear wave or converted wave data (SS- or PS-waves) through multi-component data are available, another equation expressing the time-shift induced by shear wave velocity changes as a function of ΔP and ΔS can be added to the non-linear system. The S-wave time-shift reads

$$\Delta T_{ss} \approx -\frac{2D}{\beta_0^r + \delta\beta_0^r}\left(j_\beta\left(\Delta S\right)^2 + k_\beta \Delta S + l_\beta \Delta P + m_\beta\left(\Delta P\right)^2\right), \quad (2.18)$$

obtained the same way as eq. 2.17. The Gauss-Newton convergence algorithm used to solve the system of three non-linear equations can be used to solve the system of 4 quadratic equations.
Note that the time-shift represents an integrated change over the reservoir thickness, whereas the reflection response represents a more localized response associated to the top of the reservoir. In case the reservoir thickness is within the order of a wavelength it is reasonable to assume that the changes at the top of the reservoir and those integrated over the reservoir interval do not differ too much.

2.3 The effect of approximating the rock-physics model

The relationships between changes in reservoir dynamic properties and relative changes in seismic parameters are in general derived from laboratory measurements performed on cores representative of the whole reservoir. In this synthetic study these relationships are forward modeled using a rock-physics model based on the Gassmann (1951) and Mindlin (1949) equations.

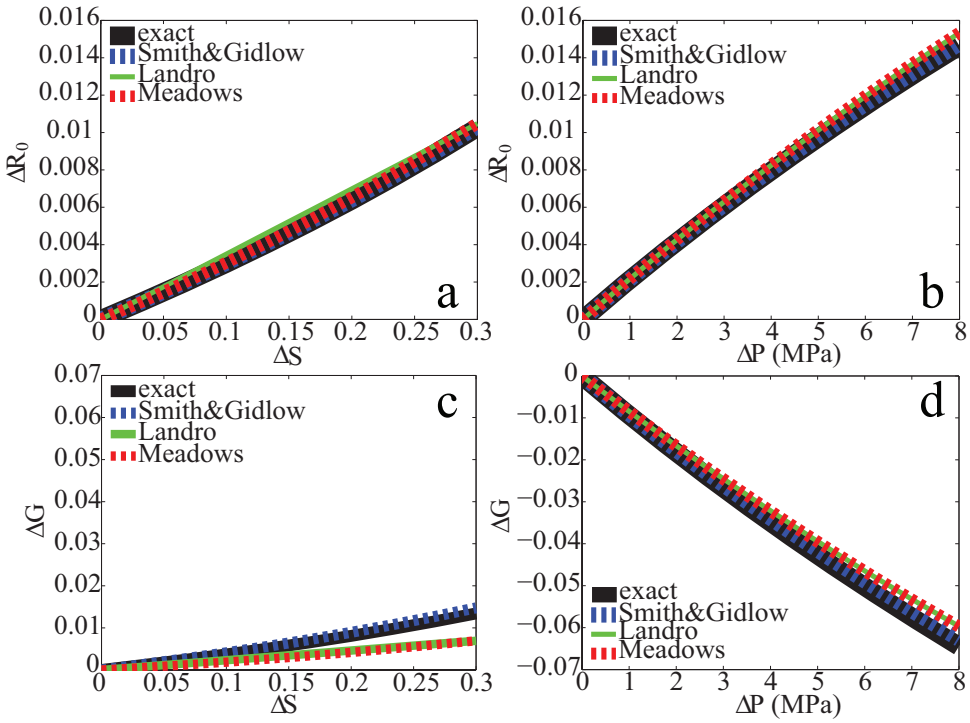

Figure 2.2: *At the top, ΔR_0 versus changes in saturation (a) and versus changes in effective pressure (b) for different approximations. The initial reflection coefficient is positive and increases with water saturation and net pressure increase. At the bottom, ΔG versus changes in water saturation (c) and versus changes in effective pressure (d) for different approximations. In plot c there seems to be a systematic error in the Smith & Gidlow and in the Landrø approximations, which cannot be solved by using a second order regression. When pressure is changing (plot d) the error seems not to occur.*

The Mindlin theory (Mindlin, 1949) calculates effective bulk and shear moduli assuming a dry dense random pack of identical spherical grains subject to hydrostatic pressure at the initial porosity of 0.36; the Hashin and Shtrikman lower bound (Hashin & Shtrikman, 1963) estimates the effective moduli at the reservoir porosity, with the assumption that the rock is everywhere isotropic, linear, elastic.

The Gassmann equation (Gassmann, 1951) predicts the seismic parameters for the saturated rock with the assumption of using long wavelengths and low frequencies (corresponding to the seismic range), in a medium where all pores are connected and fluids do not interact with the matrix.

Since for the real case studies the exact relations between changes in fluid

properties and changes in AVO coefficients are unknown, different approximations are tested in the inversion process. Figures 2.2a&b present changes in zero-offset reflectivity (ΔR_0) as a function of changes in water saturation and in pore pressure, respectively. Initial water saturation, initial effective pressure and their respective changes are the same as in figure 2.1. The overburden consists of relatively soft clay, leading to an initial positive reflection coefficient. When increasing water saturation, the zero-offset reflectivity also increases, with a trend closely resembling the P-wave velocity behavior in figure 2.1a. This was to be expected since changes in zero-offset reflectivity are mainly determined by changes in P-wave velocity and density, of which the latter is closely related to P-wave velocities again. In figure 2.2b, as for figure 2.1b, the reflection coefficient, positive at time 0, increases as the effective pressure increases. It appears evident that eq. 2.2, introduced by Smith & Gidlow (1987), approximates changes in zero-offset reflectivity almost perfectly, and the zero-offset reflectivity approximations as introduced by Landrø (2001) and Meadows (2001), respectively eqs. 2.10 and 2.14, present accuracy comparable to the zero offset reflectivity introduced by Smith & Gidlow (1987).
Figures 2.2c&d show the changes in gradient reflectivity (ΔG) as a function of changes in saturation and pressure, respectively. In figure 2.2c, the Smith & Gidlow equation (eq. 2.3) does not approximate changes in gradient reflectivity with the same accuracy as it does for zero-offset reflectivity, and the gradient expression introduced by Landrø (2001), eq. 2.11, deviates even more from the truth. This seems to be a systematic error that cannot be solved by a higher order regression as proposed by Meadows (2001), in eq. 2.15. For pressure changes, figure 2.2d, the problem does not occur.
In general, the quadratic equations better approximate variations in seismic attributes. However, in real data examples the question remains of course, whether the uncertainty on the rock physics framework justifies the use of higher order approximations. In that case the simple linear approximation provides insight in the uncertainty range. Note that in a real case, the regression coefficients for changes in pressure are in general estimated from core data, and for changes in saturation a calibrated rock physics model based on the Gassmann equation is used, as in Landrø (2001).
Figures 2.3a-b present, respectively, the differences between the 'exact' ΔR_0 and Landrø's approximation (eq. 2.10) and the difference between the 'exact' ΔR_0 and Meadows' approximation (2.14), in a region of perturbation ranging between 0 and 0.3 for changes in saturation (ΔS) and between 0 and +8 MPa for changes in net pressure (ΔP); initial water saturation and pore pressure are the same as in the previous figures. Figures 2.3c show the differences

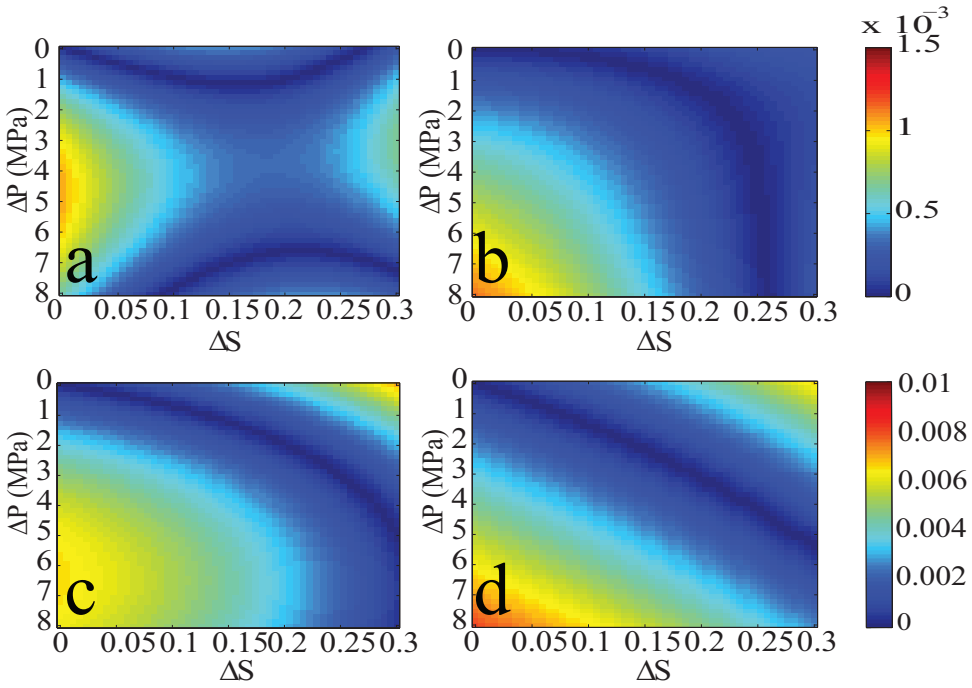

Figure 2.3: *Differences between the truth ΔR_0 and the approximated change in zero-offset reflectivity as a function of pressure and saturation changes, according to Landrø's formula (plot a) and Meadows' approximation (plot b). As expected, the quadratic approximation from Meadows provides the smallest mismatch. In the second row, differences between the true ΔG and the approximated change in gradient as a function of pressure and saturation changes according to Landrø's formula (plot c), and Meadows' approximation (plot d). Both the approximations reveal similar, quite poor accuracies.*

between the real and the gradient reflectivity using Landrø's approximation (2.11), and figure 2.3d the difference between the real and and the gradient reflectivity estimated with Meadows'approximation (eq. 2.15) in the same perturbation space as for figures 2.3a-b. The approximation of ΔR_0 is very accurate over the entire range, especially when a quadratic approximation is used, but the approximation of ΔG is less accurate, mainly at high values of changes in saturation.

In figure 2.4a the 'exact' P-wave time-shift and its quadratic approximation (eq. 2.17) are expressed as a function of ΔS and in figure 2.4b as a function of ΔP. Initial water saturation and pressure values, as well as the changes in both properties are the same as in the previous figures.

Figures 2.4c&d illustrate the timeshift in shear wave velocities and its quad-

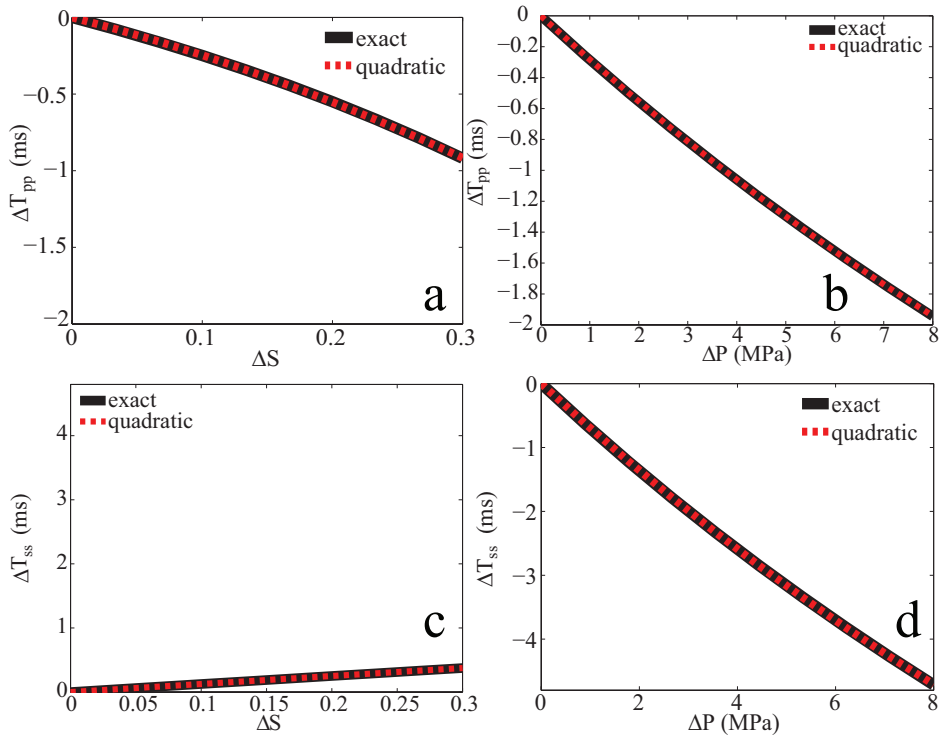

Figure 2.4: *P-wave velocity induced time-shifts as a function of changes in saturation (a) and effective pressure (b). As water saturation and/or net pressure increases, the time shift decreases since the P-wave velocity increases. The black line represents the truth case, the red line a quadratic approximation. At the bottom, S-wave velocity induced time-shifts as a function of changes in saturation (c) and in effective pressure (d) are presented. Initial water saturation is 0.2 and initial reservoir net pressure is 17 MPa.*

ratic approximation (eq. 2.18) both versus a ΔS increase (c) and versus a ΔP change (d). Initial water saturation and pressure conditions again are identical to the values presented in figures 2.1a&b, and the reservoir thickness is about 30 m. In all cases, a second order approximation presents very high accuracy.

2.4 Results

2.4.1 Description of the model

In order to evaluate the accuracy of the different proposed approximations, a synthetic reservoir model has been used. This is a 74 x 24 x 7 gridblock simulation model, with gridblock size of 150 x 150 x 4.5 m corresponding to an area of 11.1 x 3.6 km. The reservoir model has an anticlinal structure, the same as in the synthetic Brugge Field (Peters *et al.*, 2009). The reservoir is entirely composed by unconsolidated, loose sand; its porosity, normally distributed, ranges between values of 0.04 and 0.35, and its permeability, correlated to porosity ranges between 2 and 5000 md. The reservoir is divided into seven layers, each of them presenting two high porosity/permeability structures on the western flank of the anticline, surrounded by low permeability areas; such a permeability contrast is expected to cause preferential flow patterns and therefore preferential changes in seismic attributes. The porosity distribution is the result of a conditioned sequential Gaussian simulation obtained using an exponential variogram with 5000 m major correlation length, 500 m minor correlation length, nugget effect of 0.1 and azimuth of 80°W. Figures 2.5a&b present the porosity fields for two different layers, and figures 2.5c&d the associated permeability fields. The green arrows point towards the North.
The top of the reservoir lies at a depth of 1590 m; the overburden pressure is around 37 MPa and the initial pore pressure is hydrostatic, with a mean value of 17MPa. Two fluid phases are present in the model: water and undersaturated oil. Initially the oil is above the bubble point and during production, occurring simultaneously to water injection, pressure is maintained high so that the gas remains totally dissolved. Figures 2.5e&f show the initial saturation, for two different layers, before production starts: the oil-water contact lies at 1678 m depth; in the water saturated zone water saturation is 1, while in the oil zone connate water saturation and residual oil saturation are both 0.2. In total 30 wells penetrate the reservoir: a crown of 10 water injectors in the lower part of the anticline and 20 producers on the crest, the position being the same as in the Brugge Field (Peters *et al.*, 2009). The over- and the underburden seal the reservoir completely allowing in- and outflow only at the wells. During the simulation, the producers are constrained on total liquid rates, and the injectors on fixed injection pressure.
Pre-stack time-lapse seismic data have been modeled using ray tracing; the baseline survey has been acquired before production starts and the monitor survey after 30 years production. The seismic properties at each reservoir gridblock are determined from the rock physics model given the saturation and pressures resulting from the reservoir simulation. Given the large grid

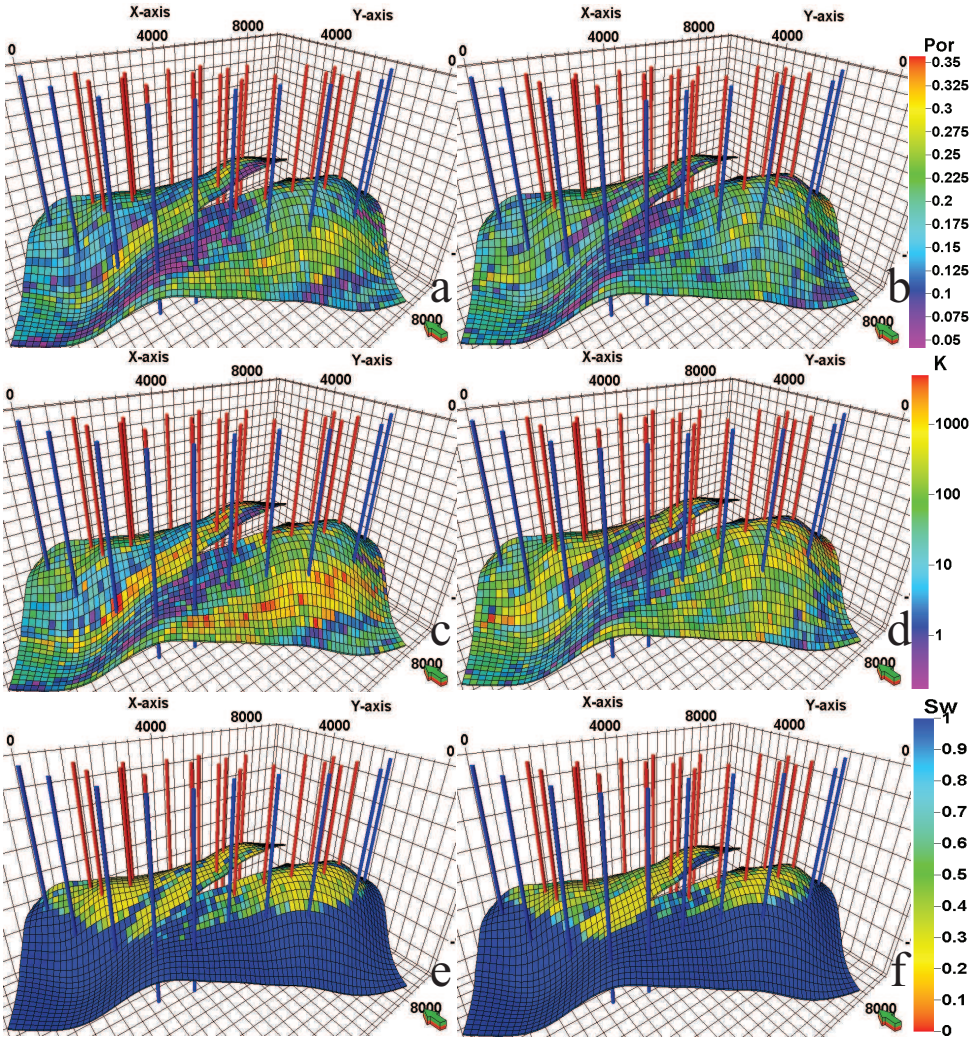

Figure 2.5: *Porosity field for layer 1 (a) and layer 5 (b), and the associated permeability field in mD (c&d). In all layers, two low porosity and low permeability elongated structures can be observed in the western part of the anticline. At the edges of these structures, porosities and permeabilities reach higher values. At the bottom, initial water saturation values for the same layers (e&f). In blue are indicated the injectors, in red the producers.*

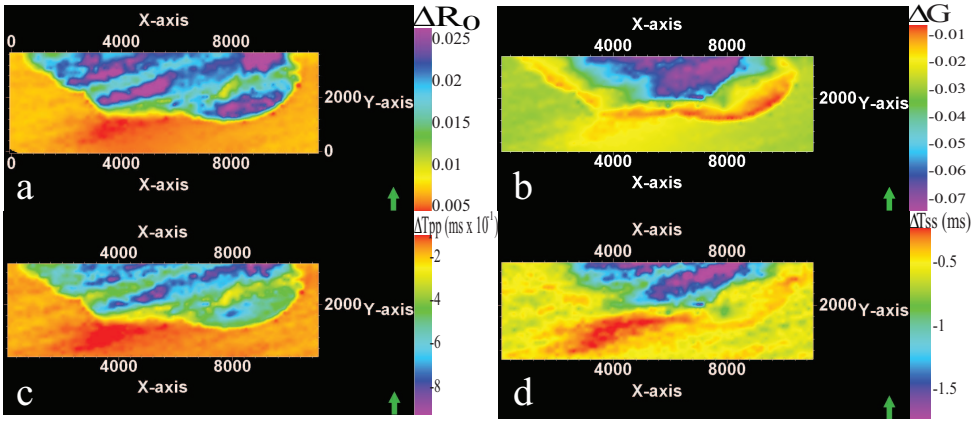

Figure 2.6: *ΔR_0 (a) and ΔG (b) determined at the top reservoir reflector. Changes in different AVO coefficients relate to changes in different reservoir fluid properties. In plots c and d are plotted, respectively, the P- and the S-wave time-shifts; both the time-shifts are picked at the bottom reservoir reflector. Note the similarity between ΔR_0 and ΔT_{pp}, and between ΔG and ΔT_{ss}. ΔR_0 and ΔT_{pp} are the combined effects of ΔS and ΔP; ΔG and ΔT_{ss} are essentially related to ΔP and only to a minor extent to ΔS through a change in density.*

dimensions compared to the bin size, seismic measurements from different common-midpoints (CMP) are averaged over the entire gridblock.
For computational reasons, with respect to the original Brugge Field, the lateral and the vertical sizes of the reservoir model used in this study have been reduced, resulting in a thickness of about 30 meters. The use of a realistic frequency of 45 Hz has been chosen; given an average interval velocity of about 3500 m/s, the corresponding tuning thickness (a quarter of the wavelength) is about 20 m, smaller than the reservoir thickness. In this way the AVO coefficients for the top reservoir reflector and the time-shifts picked at the bottom (input for the inversion) can be correctly estimated. The effect of frequency on the picked AVO coefficients and time-shifts has not been further investigated in this study.
Figures 2.6a&b show, respectively, the differences in zero-offset and gradient reflectivity picked at the top reservoir reflector: variations in seismic attributes are the expressions of changes in reservoir saturation and pressure. Figures 2.6c&d illustrate the time-shifts induced by, respectively, compressional and shear wave velocities. The P-wave time-shift, legacy of saturation and density changes, presents a trend similar to the variations in zero-offset reflectivity, while the pattern of the S-wave time-shift, more related to pressure changes, emulates the one seen for ΔG.

methods	ΔR_0	ΔG	ΔT_{pp}	ΔT_{ss}
method 1	linear in ΔS quad. in ΔP	linear in ΔS quad. in ΔP	NA	NA
method 2	quad. in ΔS quad. in ΔP	quad. in ΔS quad. in ΔP	quad. in ΔS quad. in ΔP	NA
method 3	quad. in ΔS quad. in ΔP	quad. in ΔS quad. in ΔP	quad. in ΔS quad. in ΔP	quad. in ΔS quad. in ΔP
method 4	quad. in ΔS quad. in ΔP	NA	quad. in ΔS quad. in ΔP	quad. in ΔS quad. in ΔP
method 5	quad. in ΔS quad. in ΔP	complete in ΔS complete in ΔP	quad. in ΔS quad. in ΔP	NA

Table 2.1: *Characteristics of the different methods in approximating seismic attributes.*

2.4.2 Results with spatially invariant porosity

From the extracted seismic attributes, vertically averaged changes in pore pressure and saturation have been estimated with different combinations of the four presented equations. Method 1 corresponds to the traditional Landrø's (2001) scheme (using eq. 2.10 and 2.11), method 2 makes use of quadratic equations related to ΔR_0, ΔG, and ΔT_{pp} (eq. 2.14, 2.15, and 2.17), method 3 is similar to method 2 but it uses additionally the equation related to the S-wave time-shift (eq. 2.18), method 4 is identical to method 3 except that the gradient equation is neglected (eq. 2.14, 2.17, and 2.18), method 5 makes use of quadratic equations of ΔR_0, ΔT_{pp} and a linear approximation of ΔG including second order terms (equations 2.14, 2.17, and B.5, respectively). Table 2.1 summarizes the differences in the methods.
Figure 2.7a shows the real ΔS after 30 years of production/injection; note that the relatively modest change in water saturation from 0.2 to a maximum of 0.5 in 30 years production is a consequence of the vertical averaging of the 7 reservoir layers. Individual layers might have a higher residual oil saturation after flushing due to a low sweep efficiency. Figures 2.7b, c, f, g present, respectively, the estimated ΔS with the methods one to four; below each estimation, the differences with respect to the truth case are plotted. Although all estimations are able to capture perfectly the real trend of saturation changes, they all present a bias. The bias is positive in the rim where changes in saturation occur, and negative outside the rim, in the lower part of the reservoir, probably caused by a leakage from ΔP. From the comparison between figures 2.7b, c, f and figure 2.7a it can be argued that by including P- and S-wave time-shifts in the inversion, the positive bias slightly

methods	ΔS	ΔP
method 1	1.16	6.35
method 2	1.62	6.93
method 3	1.31	6.63
method 4	0.33	7.18

Table 2.2: *RMSE for the four methods in estimating ΔS and ΔP.*

decreases. By eliminating the gradient (figure 2.7g), both the positive bias for the estimated changes in ΔS and the negative bias for the gridpoints in the aquifer are reduced, but still there is room for improvement for the estimated changes in saturation on the top of the reservoir.

Figure 2.8 presents the real and the estimated ΔP with different approximations, the order being the same as in figures 2.7; below each estimation the differences with the truth are plotted. In all the estimations taking into account the gradient reflectivity (figs.2.8b, c, f) a leakage effect from ΔS is clearly visible as a halo in the central part of the reservoir; in figure 2.8g, where the information related to the gradient is neglected, ΔP presents no saturation signatures. The comparison of figure 2.7g to the other estimations of ΔS (figs. 2.7b, c, f), and the comparison between figure 2.8g to the other estimations of ΔP (figs. 2.8b, c, f) suggests that the poor approximation of the gradient reflection could be one of the causes of the leakage between the two variables.
The root mean square error (RMSE) represents a way to evaluate the performance of the different inversions. It is defined as

$$J = \sqrt{\frac{1}{N_g}\sum_{i=1}^{N_g}\left(\alpha_i^T - \alpha_i^E\right)}, \tag{2.19}$$

where α_i^T is the true value of the parameter α at the gridcell i, α_i^E the estimated value at that gridcell, and N_g the total gridcells number.
Table 2.2 lists the RMSE for ΔS and ΔP for the different methods. The information from the S-wave time-shift does not improve the inversion if this attribute is combined with the other three (method 3 vs method 2); however it becomes a real advantage in the case the S wave time-shift replaces the gradient reflectivity (method 4). In fact, the exclusion of the gradient, slightly increases the error for the ΔP estimate, but it largely reduces the error for the estimate of ΔS.
All the pictures show evident East-West oriented lineaments, that seem

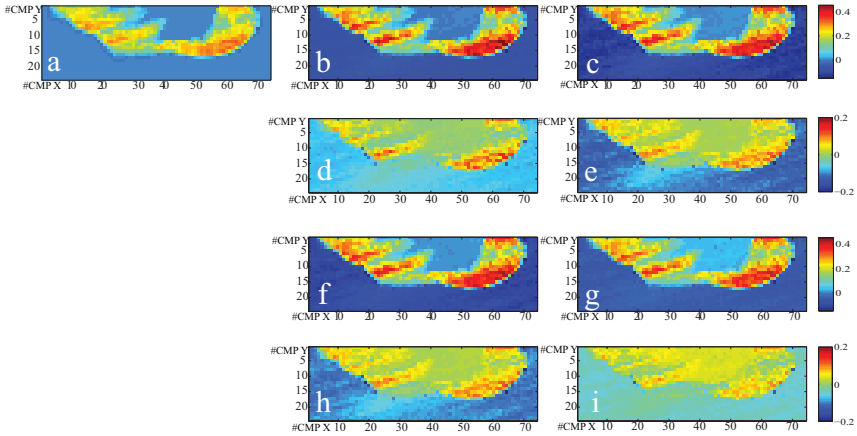

Figure 2.7: *Exact vertically averaged changes in saturation (a) versus changes in saturation estimated with method 1 (b), with method 2 (c), method 3 (f), method 4 (g). Below each estimation, the respective difference with the truth are plotted (plots d,e,h,i). The labels indicate the CMP numbers on the X and Y directions. Including P- and S-wave timeshifts slightly reduces the positive bias; by eliminating the gradient reflectivity equation, the positive bias, together with the pressure leakage outside the ΔS rim, decreases.*

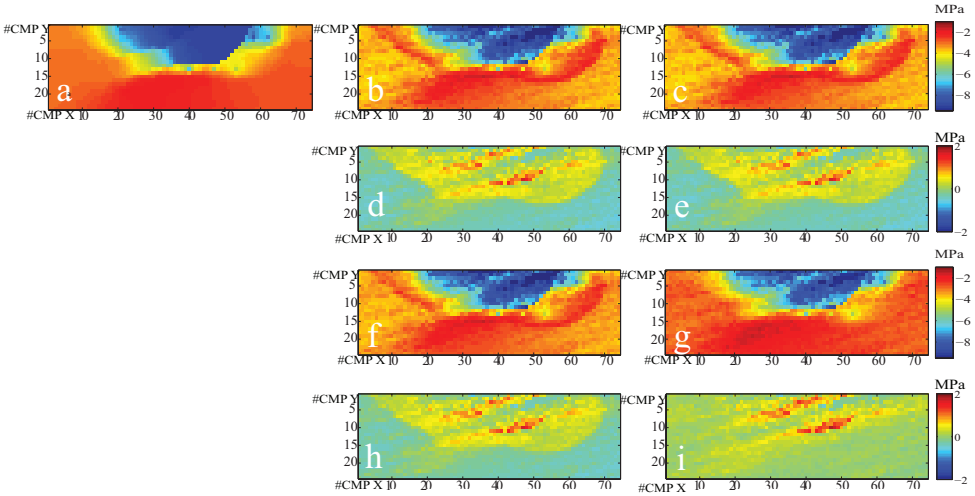

Figure 2.8: *Exact vertically averaged changes in pore pressure (a) versus changes in pressure estimated with method 1 (b), with method 2 (c), method 3 (f), method 4 (g). Below each estimation, the respective difference with the truth are plotted (plots d,e,h,i). Remarkable is the similarity between the trend in pressure changes and the trend shown by the gradient and S-wave time-shift (figs. 2.6b&d). Eliminating the gradient reflectivity equation (g) zeros the leakage from* ΔS.

strongly related to the porosity/permeability field. In the current analysis, the coefficients used in the approximations are calculated using only the mean reservoir porosity. In the next section the effect of a more detailed knowledge of the porosity field is investigated, leading to somewhat different results.

2.4.3 Results with more accurate Porosity Information

The coefficients used in the approximations are calculated from the relative change in seismic properties induced by changes in fluid saturation and in pore pressure (eqs. 2.4-2.6). These are defined as the time-lapse variation in density and velocities, consequence of production and/or injection, normalized on the mean of the respective property between the overburden and the reservoir at the initial time. The total porosity is an important parameter in the calculation of density and velocities as it enters in the Mindlin (1949) and the Gassmann (1951) equations. Also, the total porosity acts as a scaling

factor for changes in seismic properties, induced by changes in pore pressure and fluid saturation, as it determines the weight between the fluid and the rock terms in the Gassmann equation. Hence, the value of the total porosity is proportional to the relative time-lapse variations in density and seismic velocities described in eqs. 2.4-2.6.
In the previous section it was assumed that the total porosity was constant over the entire reservoir. In fact, only the mean porosity value entered in the Mindlin and Gassmann equations in order to calculate relative changes in seismic properties for different CMPs; the consequence is that the coefficients introduced in eqs. 2.7-2.9, which relate relative changes in seismic properties to ΔS and ΔP, are spatially uniform. Neglecting lateral variations of porosity results in remarkable porosity leakage, with a noticeable decrease on the results accuracy. In this section, the inversion is performed with the same methods and approximations as in the previous section, the only difference being the use of spatially variant coefficients. These are in fact calculated independently at each CMP location, assuming that the exact vertically averaged (using the arithmetic mean) porosity is known.
Figure 2.9a presents the true ΔS (the same as fig. 2.7a) and the figures b-c & f-g the estimated ΔS with methods 1, 2, 3, 4, respectively. Below each estimation the differences between the estimated and the true ΔS are plotted. In the waterflooded areas a positive bias appears evident with methods 1 to 3; although the use of quadratic approximations and of P and S-wave time-shifts (figures 2.9c&f) decreases this positive bias, the negative bias below the original oil-water contact (probably a leakage from ΔP) remains strong. Leaving out the gradient term in the inversion (figure 2.9g) largely reduces the positive bias for the real ΔS and zeros the negative bias seen in the water saturated zone, meaning that the leakage from the changes in pressure is eliminated.
Figure 2.10a shows the real changes in pressures (the same as fig. 2.8a) and the figures b-c & f-g the estimated changes using different method, the order being the same as in figure 2.8. Below the estimated ΔP, the differences with the true ΔP are plotted. In all the estimations making use of the gradient equation, a halo characterized by a positive bias appears, its shape suggests that it might be caused by a leakage from the ΔS variable; the halo disappears if the gradient is removed, as well as the negative bias for the gridpoints outside the oil rim. However, removing the changes in the gradient reflectivity means losing some information about the reservoir changes in pressure: at the top of the reservoir, where changes in pressure are stronger, the predicted ΔP are smaller than the real changes in pressure.
From the comparison between the estimates from pictures 2.9 and 2.10 to

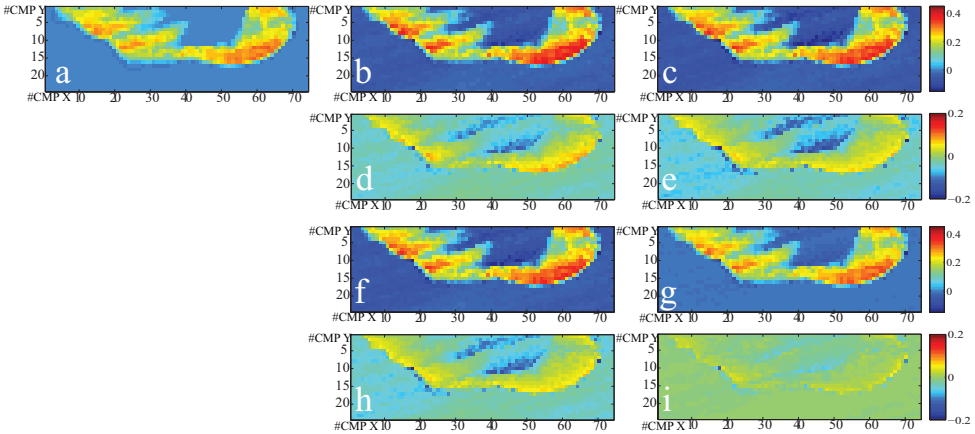

Figure 2.9: *Exact vertically averaged changes in saturation (a) versus changes in saturation estimated with method 1 (b), with method 2 (c), method 3 (f), method 4 (g). Below each estimation, the respective difference with the truth are plotted (plots d,e,h,i). The labels indicate the CMP numbers on the X and Y directions. At each CMP location the vertically averaged porosity is known; excluding the gradient reflectivity improves the estimation considerably.*

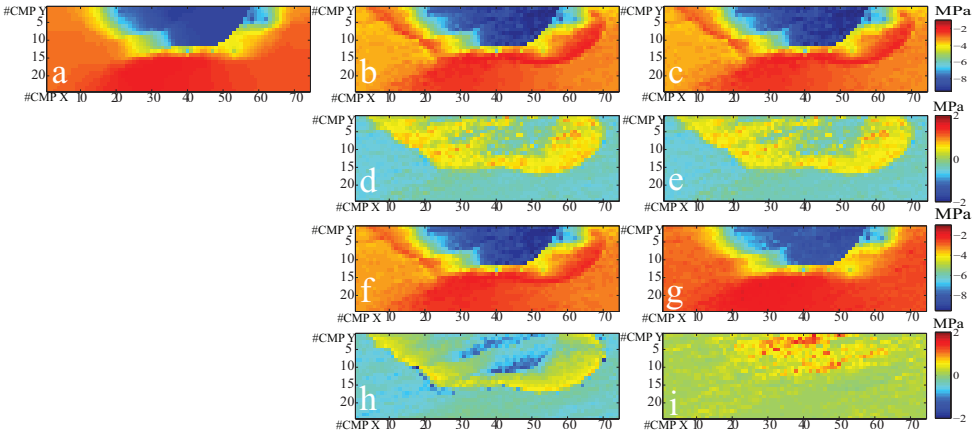

Figure 2.10: *Exact vertically averaged changes in pore pressure (a) versus changes in saturation estimated with method 1 (b), with method 2 (c), method 3 (f), method 4 (g). Below each estimation, the difference with the truth are plotted (plots d,e,h,i). The labels indicate the CMP numbers on the X and Y directions. At each CMP location the vertically averaged porosity is known. Excluding the gradient reflectivity results in overall moderate differences, although at the top of the reservoir the error can be quite large.*

methods	ΔS	ΔP
method 1	1.06	4.47
method 2	1.30	4.25
method 3	1.16	4.26
method 4	0.29	4.81

Table 2.3: *RMSE for the four methods in estimating ΔS and ΔP.*

those of figures 2.7 & 2.8 it seems that the porosity leakage decreases. Table 2.3 summarizes the performance of the different methods. The RMSE reveal that an initial investment for an accurate knowledge of the reservoir porosity field has the benefit of improved inversion results.

2.4.4 Reducing the leakage

Previous results indicate that a poor approximation of changes in gradient reflectivity leads to strong leakages between ΔS and ΔP. However, in many real cases S-waves data are not available and the equation related to the slope reflection, providing information about changes in pressure, cannot be neglected.
Compared to the approximations of the other seismic attributes presented in the inversion, the one related to the gradient reflectivity is by far the least accurate, especially when water saturation increases (figure 2.2c). The cause of this inaccuracy lies in the fact that, for computational reasons, the higher order terms in $\Delta\alpha/\alpha$, $\delta\alpha/\alpha$ (same holds for β and ρ) have been neglected, as suggested in Landrø (2001). However, if second order terms in relative changes in seismic properties, or combinations thereof, are included (for a complete derivation see Appendix B) the accuracy of the forward approximation of the gradient reflectivity increases leading to an improvement of the inversion results.
Figure 2.11 is exactly the same as figure 2.2c, except that a new curve is added (and the vertical scale exaggerated): the dotted yellow line represents changes in gradient reflectivity as a function of changes in saturation (the initial water saturation and the change in the property are the same as in figure 2.2c).

Figure 2.12a shows the true ΔS field (the same as in fig. 2.9a), figure 2.12b the estimated ΔS field using method 2 (the same as in figure 2.9c), and figure 2.12c the estimated ΔS with method 5. The vertically averaged porosity is

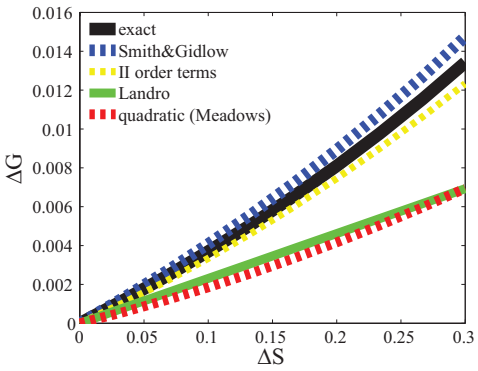

Figure 2.11: *ΔG versus change in water saturation for different approximations. The dotted yellow line represents Landrø's approximation including second order terms in relative variation of seismic properties expressed as linear function of ΔS and ΔP (see Appendix B).*

methods	ΔS	ΔP
method 2	1.30	4.25
method 5	1.24	4.23

Table 2.4: *RMSE for method 2 and 5 in estimating ΔS and ΔP.*

known at every CMP location. Figures 2.12d&e show the differences between the estimated and the true ΔS (fig. 2.12d is the same as fig. 2.9e). Although including higher order terms results in an unchanged negative bias for the CMPs in the aquifer, it decreases the positive bias for the estimated ΔS in the waterflooded areas and slightly reduces the negative bias for ΔS estimated on the top of the reservoir.
Figures 2.12f-h present the true and the estimated ΔP with the same methods as for figures 2.12a-c (fig. 2.12f is the same as fig. 2.10a, and fig. 2.12g is the same as fig. 2.10c). Figures 2.12i&j illustrate the differences between the estimated and the true ΔP in the same order as for figures 2.12d&e (fig. 2.12i is the same as fig. 2.10e). The halo characterized by positive variations in pressure almost disappears (plot j), proving that the inaccuracy of the gradient approximation is one of the causes of the leakage from ΔS into ΔP. Table 2.4 lists the RMSE for methods 2 and 5.

2.4.5 The effect of random and systematic noise

The previous sections explained the validity of the inversion scheme from an ideal case where no noise on seismic measurements is present. This section

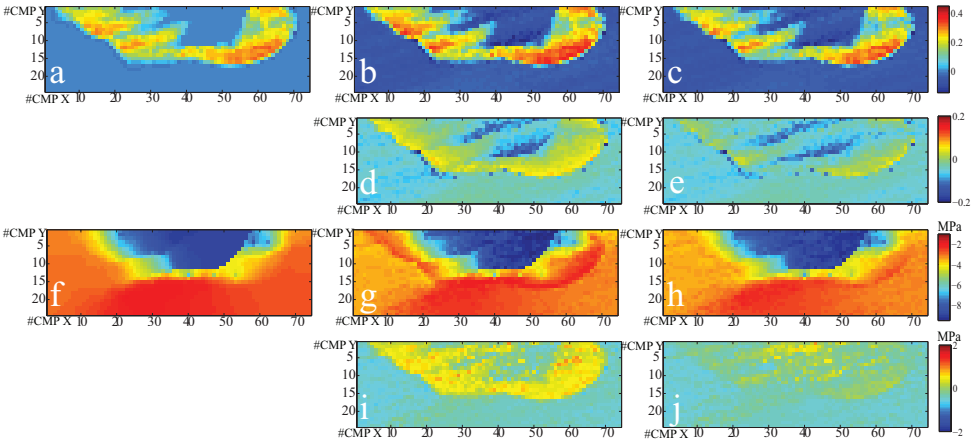

Figure 2.12: *Exact vertically averaged changes in saturation (a) versus changes in saturation estimated with method 2 (b) and 5 (c). The figures below each estimate represent the respective difference with the truth case (plots d and e). The labels indicate the CMP numbers on the X and Y directions. At each CMP location the vertically averaged porosity is known. Including the higher order terms leads to a reduction of the positive bias for the saturation changes in the waterflooded areas. In the third line, exact vertically averaged changes in pressure (f) versus changes in pressure estimated with method 2 (g) and 5 (h); below each estimate are plotted the respective differences with the truth (plots i and j). Including the higher order term in the gradient equation results in a strong decrease of the saturation leakage into the pressure changes.*

deals with a more realistic scenario as it indicates the effect of adding random and systematic noise on the observed inputs.
Figures 2.13a (the same as fig. 2.9a) illustrates the true ΔS field and figures 2.13b-c,f-h the estimates obtained with, respectively, methods 1,2,5,3,4 in case random noise up to 15% is added to the measurements. Below each figure, the differences with the truth estimates are plotted. The vertically averaged porosity is known at each CMP location. Although the images are not as sharp as in the free noise case, the advantage of using a complete approximation of the gradient or the advantage of replacing this attribute with the S-wave time-shift is still evident. Figure 2.14 presents the true and the estimated ΔP with the five methods, and their deviations from the the truth, in the same order as in figure 2.13 (plot a is the same as fig. 2.10a). Also for ΔP, despite the noise, the same features as in the noise free case are recognized.
The estimates look quite robust in the presence of random noise (up to 15%);

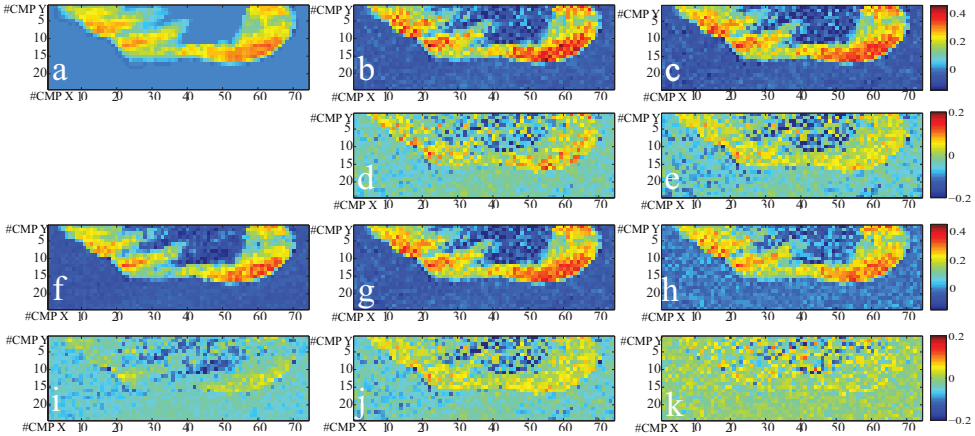

Figure 2.13: *Exact vertically averaged changes in saturation (a) versus changes in saturation estimated with method 1 (b), method 2 (c), method 5 (f), method 3 (g) and method 4 (h). The figures below each estimate represent the respective difference with the truth (plots d,e,i,j,k). The labels indicate the CMP numbers on the X and Y directions. Seismic measurements contain random noise up to 15%. Although the general quality of the different estimates decreases because of the noise, all the features seen in figure 2.9 can be recognized.*

however, this kind of noise, in reality, can be combined with systematic noise which can be easily introduced by numerous factors (like the characteristics of the source, of the receiver and of the cable characteristics, processing, energy attenuation and absorption, tuning, etc.). The next pictures show estimates when random noise up to 10% is combined with an error of +5% in ΔR_0, +15% in ΔG, and +10% on the time-shifts. Figure 2.15 illustrates the real ΔS (same as in fig. 2.9a), the estimated ΔS, and their deviation from the truth in the same order as in the previous pictures. The characteristics of each method are still relatively clear, although the magnitude of the leakages between different parameters and of the bias in estimated ΔS have changed. The same can be said for figure 2.16, presenting the situation for changes in pressure (plot a is the same as fig. 2.10a). Note that a systematic error in the inputs leads to a change in sign of the error for the ΔP estimated with method 4 at the top of the reservoir (see figure 2.10i). Table 2.5 and 2.6 present a list of the RMSE values in case of random noise and random plus systematic noise, respectively.

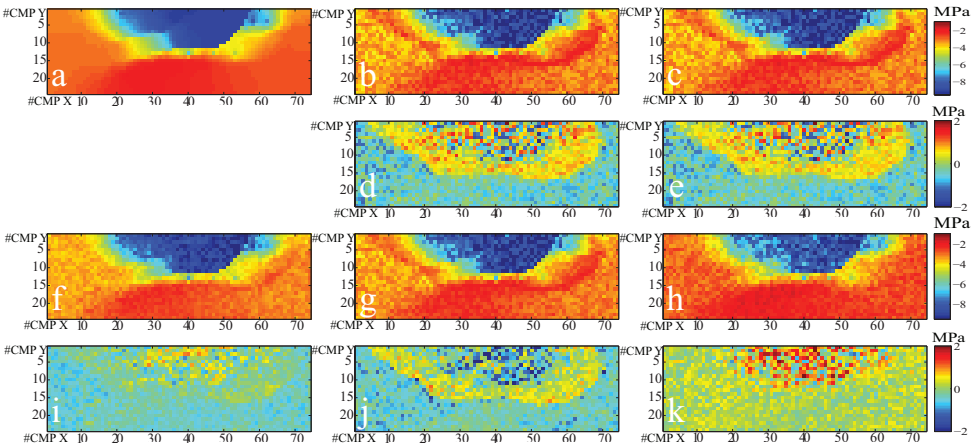

Figure 2.14: *Exact vertically averaged changes in pressure (a) versus changes in pressure estimated with method 1 (b), method 2 (c), method 5 (f), method 3 (g) and method 4 (h). The figures below each estimate represent the respective difference with the truth (plots d,e,i,j,k). The labels indicate the CMP numbers on the X and Y directions. Seismic measurements contain random noise up to 15%. Although the general quality of the different estimates decreases because of the noise, all the features seen in figure 2.10 can be recognized.*

methods	ΔS	ΔP
method 1	1.09	6.25
method 2	1.38	7.23
method 3	1.19	5.53
method 4	0.33	6.32
method 5	1.42	7.28

Table 2.5: *RMSE for the five methods in presence of random noise with 15%standard deviation.*

methods	ΔS	ΔP
method 1	1.84	43.15
method 2	2.41	44.46
method 3	2.01	40.60
method 4	0.50	20.21
method 5	2.37	21.19

Table 2.6: *RMSE for the five methods in presence of random noise with 15%standard deviation and systematic noise up to 15% in the observed measurements.*

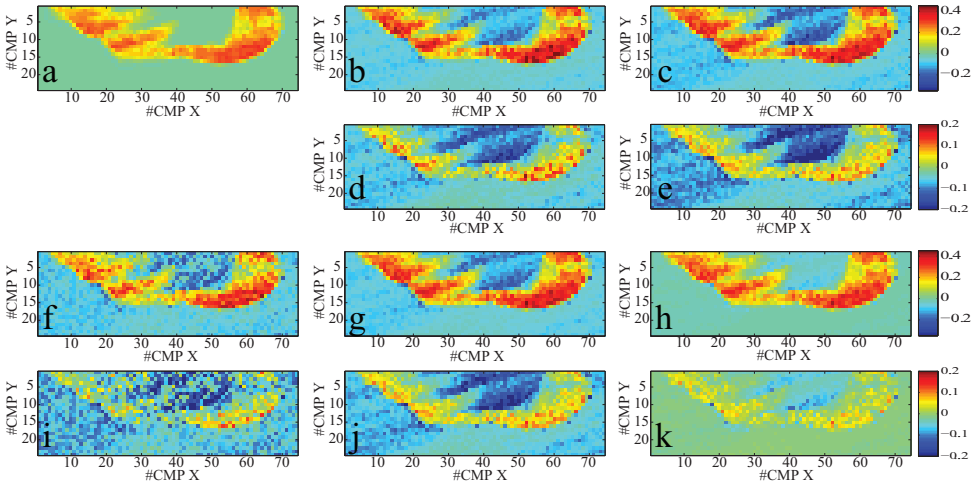

Figure 2.15: *Exact vertically averaged changes in saturation (a) versus changes in saturation estimated with method 1 (b), method 2 (c), method 5 (f), method 3 (g) and method 4 (h). The figures below each estimate represent the respective difference with the truth (plots d,e,i,j,k). The labels indicate the CMP numbers on the X and Y directions. Seismic measurements contain random noise up to 15% and systematic noise up to 15%. Systematic noise has a strong impact on the quality of the estimates, in some cases enhancing the leakage and the bias present in the different methods.*

2.5 Discussion

Spatial variations in mineralogy and temperature are expected to have a smaller impact on the inversion results than variations in porosity.
In this study, the reservoir is composed entirely of unconsolidated, loose sand, allowing to use the Mindlin, Hashin-Strikman and Gassmann equations to calculate seismic properties in every cell. In this scenario the fluid term of the Gassmann equation plays a relevant role in determining the seismic properties of the whole rock, while in consolidated sands production/injection related fluid effects might be more difficult to detect, jeopardizing the validity of the inversion method. However, if time-lapse changes in seismic attributes even in case of deep-buried consolidated sands, are above the detection threshold, the presented scheme can still be successfully applied. In case of consolidated sandy reservoirs or of clay intrusions, the simple Hertz-Mindlin model (Mindlin, 1949) cannot be used and the dry rock moduli need to be estimated with different models (Dvorkin & Nur, 1996; Dræge *et al.*, 2006).
It is important to note that reflection derived properties are very local, op-

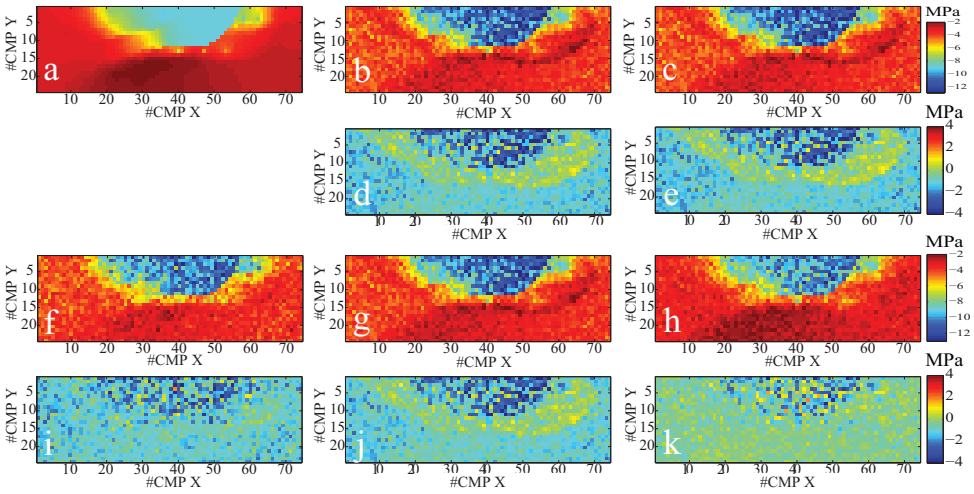

Figure 2.16: *Exact vertically averaged changes in pressure (a) versus changes in pressure estimated with method 1 (b), method 2 (c), method 5 (f), method 3 (g) and method 4 (h). The figures below each estimate represent the respective difference with the truth (plots d,e,i,j,k). The labels indicate the CMP numbers on the X and Y directions. The systematic noise has a strong impact on the estimates aspect, changing the magnitude or in some cases the sign of the biases present in the different methods.*

posed to the time-shift derived properties, as they are averaged over the whole reservoir thickness. In this study, a relatively homogeneous vertical distribution of porosity, pressure and saturation has been assumed; violation of this condition will deteriorate the results. A way to circumvent this problem is by using a stochastic approach with multiple realizations having different internal reservoir parameter distributions; however, the latter solution has not been explored in this chapter.

The inversion scheme presents the theoretical advantage of replacing the gradient reflectivity, generally showing a low S/N ratio and requiring careful log calibration (Whitcombe, 2002), with time-shift data. In fact, this substitution results in a large reduction of the error in changes in saturation that compensates a relatively small increase for the error in ΔP. However, the method is not applicable for reservoirs at or below the tuning thickness, as the time-shifts cannot be correctly estimated.

The presented scheme, as every 4D seismic inversion method, strictly relies on the quality and the accuracy of the measurements. In this case study, the effect of 30 years production combined with waterflooding are quite easy to

detect on seismic attributes. Note that the method works also outside the reservoir, where changes in saturation are zero and changes in pressure moderate. This demonstrates that the method will also work at much smaller time intervals, that is smaller time-lapse differences.

2.6 Conclusions

In this chapter, a 4D seismic inversion scheme which solves for time-lapse changes in pore fluid and pressure has been presented; it is based on a modified form of Landrø's (2001) equations and extended with two additional equations expressing the time-shift induced by P- and S-wave velocity changes as functions of pore pressure and saturation changes.
The results show that assuming spatially invariant coefficients used in the approximations of changes in seismic attributes leads to less accurate results as porosity leakage affects the final estimates; if the porosity field is known, or at least the vertically averaged porosity at each CMP location, the quality of the inversion improves considerably and the porosity imprint is attenuated.
Final estimates generally suffer from leakage between changes in saturation and changes in pressure caused by the inaccuracy of the forward approximation of the gradient reflectivity changes. By replacing this equation with the approximation related to the time-shift equation, the leakage almost disappears. If time-shift data are not available, the leakage effect is strongly reduced if, in the gradient equation, the second order terms in relative changes in seismic properties are added. The leakage problem, as mentioned by Landrø (2001) and Meadows (2001), is exacerbated by the lack of repeatability, uncertainty in the scaling factor between different angle-stacks, or the validity of the rock-physics model. In this synthetic case, where the uncertainty in the rock-physics model is the only source of error, it is demonstrated that the inaccuracy of the gradient approximation is a major cause of the leakage between different parameters.
The final estimates seem to be relatively robust to seismic noise. Changes in saturation and pressure present fairly high accuracy in the presence of random noise up to 15%; in the presence of systematic noise up to the order of 10%, final estimates show biased errors but their main features can still be recognized clearly.
The presented scheme shows good results in case the impedance contrast between the overburden and the reservoir is high. A weaker contrast will represent a limitation of the method as the relative noise level in the extracted attribute increases.
In the next chapters the presented inversion scheme is included in an as-

similation scheme based on the Ensemble Kalman Filter; the objective is to fully understand the added value of 4D seismic inversions for better reservoir properties estimation and for an improved production forecast.

Chapter 3

The Ensemble Kalman Filter: origin and evolution

This chapter provides an introduction to the EnKF, including an overview of proposed improvements in the literature. Particular attention is given to methods circumventing the problem of filter divergence, often observed in case large datasets, such as time-lapse seismic data, are assimilated with the EnKF.

3.1 The origin of the Ensemble Kalman Filter: the Kalman Filter

Introduced by Evensen (1994) in oceanography, the EnKF has been applied in petroleum engineering only recently (Lorentzen *et al.*, 2001). Since it has gained an increasing interest for solving history matching problems.
The EnKF is based on the classical Kalman filter (KF) introduced by Kalman (1960). This section introduces the KF and the derivation of the EnKF.

KF is an ideal tool when all the dynamics and noise statistics are exactly known. In order to introduce the KF, we define two concepts. The "truth" is the actual physical system that we are interested in. The model is the mathematical description, which is used for the filter design stage.
Kalman filtering represents the link between a model and measurements. This technique processes the measurements in a physically consistent way, taking into account the model. This is achieved by extending the deterministic model represented by:

$$\mathbf{x_{k+1}} = \mathbf{M}(\mathbf{x_k}) \tag{3.1}$$

to a stochastic model:

$$\mathbf{x_{k+1}} = \mathbf{M}(\mathbf{x_k}) + \mathbf{w_k} \tag{3.2}$$

In the equations $\mathbf{x}$ indicates the true state vector -that is the vector containing the variables to estimate like for example permeability, porosity, OWC, etc- , $\mathbf{M}$ represents one time step of the numerical simulation model, the subscript refers to the time at which a vector is considered (time k or time k+1), and $\mathbf{w_k}$ represents the model forecast error at timestep k. This is assumed to be a stochastic perturbation with zero mean $\overline{\mathbf{w_k}} = \mathbf{0}$ and covariance matrix $\overline{\mathbf{w_k}\left(\mathbf{w_k}\right)^T} = \mathbf{C}_{xx}^f$.
All the available data for time k are stored in a vector $\mathbf{d_k}$. The "true" data or the "true" values measured without errors are supposed to be related to the true state according to a linear observation model:

$$\mathbf{d_k} = \mathbf{H_k}{\mathbf{x_k}}^T \tag{3.3}$$

Through the observation model operator $\mathbf{H}$, a forecast for the observed data locations can be made from the forecast of the state. Uncertainties in the measurements need to be specified as well. Therefore, the vector $\mathbf{d_k}$ from equation (3.3) is expanded as follows:

$$\mathbf{d_k} = \mathbf{H_k}{\mathbf{x_k}}^T + \boldsymbol{\epsilon}_k \tag{3.4}$$

where $\boldsymbol{\epsilon}_k$ is the observation error. It consists of the measurements error due to imperfect measurements and the representation error caused by the discretization of the dynamics. This vector is assumed to be of zero mean ($\overline{\boldsymbol{\epsilon}(t_k)} = \mathbf{0}$). Its covariance matrix is defined as $\mathbf{C}_{\epsilon\epsilon} = \overline{\boldsymbol{\epsilon_k}\boldsymbol{\epsilon_k^T}}$ and it is assumed to be uncorrelated with the model error $\overline{\mathbf{w_k}\boldsymbol{\epsilon_k})^T} = \mathbf{0}$ (Hanea, 2005).
Kalman filtering tries to combine the information from the model and from observations to update the state vector. Using Bayes theorem (1.5) as in Cohn (1997) and Maybeck (1979), the posterior density function of the analyzed state $\mathbf{x}^a$ can be expressed as

$$f(\mathbf{x}^a|\mathbf{d}) \propto exp\left(-\frac{1}{2}J[\mathbf{x}^a]\right) \tag{3.5}$$

where

$$J[\mathbf{x}^a] = \left(\mathbf{x}^f - \mathbf{x}^a\right)^T \left(\mathbf{C}_{xx}^f\right)^{-1} \left(\mathbf{x}^f - \mathbf{x}^a\right) + \left(\mathbf{d} - \mathbf{H}\mathbf{x}^a\right)^T \left(\mathbf{C}_{\epsilon\epsilon}\right)^{-1} \left(\mathbf{d} - \mathbf{H}\mathbf{x}^a\right) \tag{3.6}$$

The function J can be read as in section 1.5: the first part represents the prior information, or the initial guess about the state, while the second term is the conditional probability of the data given the state of nature. The minimum of J is found by differenciating it with respect to $\mathbf{x}^a$. The minimum of this function, which corresponds to the maximum likelihood estimate is

$$\mathbf{x}^a = \mathbf{x}^f + \mathbf{K}\left(\mathbf{d} - \mathbf{H}\mathbf{x}^f\right) \tag{3.7}$$

The matrix $\mathbf{K}$ is called the Kalman gain and it is expressed as

$$\mathbf{K} = \mathbf{C}_{xx}^f \mathbf{H}^T \left(\mathbf{H}\mathbf{C}_{xx}^f \mathbf{H}^T + \mathbf{C}_{\epsilon\epsilon}\right)^{-1} \tag{3.8}$$

The Kalman gain is the ratio between the covariance of the model error with the observations and the sum of the covariance of the predicted observations with the forecast error covariance matrix. This can be interpreted as the ratio between the model uncertainty and the sum of the uncertainties related to the model and to the observations.
The analyzed (posterior) model error covariance analysis is expressed as

$$\mathbf{C}_{xx}^a = (\mathbf{I} - \mathbf{K}\mathbf{H})\,\mathbf{C}_{xx}^f \tag{3.9}$$

which can be derived as the minimum error variance of the analyzed estimate (Evensen, 2009). Therefore, the Kalman filtering seeks for the maximum likelihood estimate which coincides with the minimum variance estimate in case of Gaussian priors and model linearity.

3.2 The EnKF: introduction

The KF was adapted to work with nonlinear modes with the introduction of the extended Kalman Filter (EKF). The EKF uses linearizations of the model and observation equations around the estimated mean of the state (tangent linear model, TLM). This algorithm was used for parameter estimation in hydrology (Eigbe *et al.*, 1998), but the quality of the EKF update is severely jeopardized in case of highly nonlinear models. Another important shortcoming of the EKF (and of the KF in general) is that the prior and the posterior true error covariances need to be stored and propagated in time. This gives rise to two limitations. First,the true error is never known; second, since those matrices have equal size as the square of the state vector, the method is not easily applicable to high dimensional models. Therefore, during the last decades, several alternatives to the EKF have been developed.

The EnKF (Evensen, 1994) is a Monte Carlo, sequential method which circumvents these two important limitations of the KF by representing the error covariance matrix with an ensemble of model realizations. Unlike in the KF or EKF, in the EnKF N realization representing the state vectors (called 'ensemble members') are treated as a sample from the prior distribution of the model state at a certain time, and their mean is treated as the state estimate from the forecast model in the standard KF (Anderson, 2009). On the other hand the spread in the ensemble (standard deviation) represents the initial model uncertainty around the mean.
In the forward step of the EnKF, the model equations are applied to each of the ensemble members (see eq.3.2 in case of linear models). The update step is computed using the form of the KF equation but avoids the computation and the storage of the full covariances matrices for model and measurement uncertainties. As the initial realizations are drawn randomly from the prior model variables distribution, the EnKF circumvents the limitation of assuming an infinite distribution (as a real Gaussian distribution would be). However, the analysis step, same as in KF, is still based on the first two-points statistics of the distributions, limiting the performance of the filter when the Gaussian assumption is strongly violated.
The first application of the EnKF in reservoir engineering was presented in Lorentzen *et al.* (2001), where, using well measurements, improved predictions of pressure behavior were obtained. The successful application of the EnKF in this paper, motivated Nævdal *et al.* (2002) to apply the EnKF to the update the permeability field in near-well reservoir models. The authors obtained improved production forecasts.
After these initial studies, the number and the complexity of the case studies where the EnKF was implemented, rapidly increased (Naevdal *et al.*, 2005; Gu & Oliver, 2005). Skjervheim *et al.* (2007) for the first time proved the added value of 4D seismic in the data assimilation process based on the EnKF on a 2D synthetic model and on a 3D field case. In the 2D case, with the assimilation of changes in elastic impedances, the permeability estimate largely improved; in the 3D case, the assimilation of changes in Poisson's ratios, added to production data, led to a different estimation of the permeability field, with respect to the case where only production data were used. Skjervheim & Ruud (2006) applied the EnKF method to assimilate production and waveform data on a 2D synthetic model with the result of an improved production forecast and porosity/permeability estimate compared to the base case.

3.3 The EnKF formulation

In section 3.1, the measurement operator was assumed linear and therefore indicated with $\mathbf{H}$. In the EnKF, the measurement operator relating the true model state to the observations is nonlinear and therefore indicated with $\mathcal{H}$. Hence, the EnKF analysis equation reads:

$$\mathbf{A^a} = \mathbf{A} + \mathbf{P}^f \mathcal{H}^T \left(\mathcal{H} \mathbf{P^f} \mathcal{H}^{\mathbf{T}} + \mathbf{R} \right)^{-1} \left(\mathbf{D} - \mathcal{H} \left(\mathbf{A} \right) \right), \tag{3.10}$$

In this equation $\mathbf{A}$ indicates the matrix comprising the state vectors (or augmented state vectors, that is the vectors containing state and parameters to update) of the N ensemble forecasts (in the KF corresponding to the vector $\mathbf{a}$). $\mathbf{A}$ is defined as:

$$\mathbf{A} = (\mathbf{x_1}, \mathbf{x_2}, ..., \mathbf{x_N}) \tag{3.11}$$

with x_1, x_2, x_N being the state vectors for all the N members. The term $\mathbf{P}^f$ indicates the ensemble forecast covariance matrix defined as:

$$\mathbf{P}^f = \frac{\mathbf{A'A}^T}{N-1}, \tag{3.12}$$

with $\mathbf{A'}$ being the ensemble perturbation matrix. It is expressed as:

$$\mathbf{A'} = \mathbf{A} - \overline{\mathbf{A}} = \mathbf{A}(\mathbf{I} - \mathbf{1}_N) \tag{3.13}$$

with $\overline{\mathbf{A}}$ being the matrix storing the ensemble mean in each column and $\mathbf{1}_N$ being the matrix with all elements equal to 1/N. The ensemble forecast covariance matrix corresponds to the model error covariance matrix defined in section 3.1 $\mathbf{C}_{xx}^f$.
The term $\mathbf{P}^f \mathcal{H}^T$ is the ensemble cross-covariance matrix between modeled parameters/states and observations while $\mathcal{H} \left(\mathbf{P}^f \right) \mathcal{H}^T$ indicates the ensemble-based error covariance matrix of simulated measurements.
$\mathbf{D}$ denotes the ensemble matrix of perturbed measurement vectors, defined as

$$\mathbf{D} = (\mathbf{d_1}, \mathbf{d_2}, ..., \mathbf{d_N}) \tag{3.14}$$

with $\mathbf{d_j}$ being the N vectors of observations perturbed with white noise. These are given as

$$\mathbf{d_j} = \mathbf{d} + \epsilon_j \quad \text{j=1,...,N} \tag{3.15}$$

From the ensemble perturbations ϵ_j the measurement error covariance $\mathbf{R}$ can be constructed in a stochastic way (Evensen, 2004; Skjervheim *et al.*, 2006). This is done by storing the ensemble perturbations in the matrix $\mathbf{E}$:

$$\mathbf{E} = (\epsilon_1, \epsilon_2, ..., \epsilon_N) \tag{3.16}$$

and multiplying $\mathbf{E}$ by its transpose divided by N-1:

$$\mathbf{R} = \frac{\mathbf{E}\mathbf{E}^T}{N-1}. \tag{3.17}$$

The matrix $\mathbf{R}$ in the EnKF replaces the true observation error covariance matrix $\mathbf{C}_{\epsilon\epsilon}$ in the KF equation.
However, in the following experiments the observation error matrix has been constructed differently. The standard deviation for each measurement error is specified upfront. The reservoir simulator generates N samples of a Gaussian distribution centered around the true measurement value and with a standard deviation equal to the one specified.
The term $\mathbf{P}^f\mathcal{H}^T\left(\mathcal{H}\mathbf{P^f}\mathcal{H}^\mathbf{T} + \mathbf{R}\right)^{-1}$ is the Kalman gain and it can be read in the same way as described in section 3.1. From the EnKF analysis equation it can be observed that the term $\mathbf{A^a}$ is a weighted linear combination between the model prediction $\mathbf{A^f}$ and an adjustment related to the observations; hence, $\mathbf{A^a}$ inherits the predictor-corrector structure from the KF analysis.
Evensen *et al.* (2007) describes the EnKF as a method for solving the general state and parameter estimation problem in a Bayesian framework. The main objective of the EnKF is to sample from the posterior state distribution conditioned to observation data using Monte Carlo integration in time. If this distribution is conditioned to data from all the previous timesteps then the 'smoother' solution is obtained (Ensemble Kalman Smoother or EnKS). The EnKS equation can be derived in a bayesian framework as

$$f(\mathbf{A_0}, ..., \mathbf{A_k} \mid \mathbf{d_1}, ..., \mathbf{d_k}) = \frac{f(\mathbf{A_0}, ..., \mathbf{A_{k-1}} \mid \mathbf{d_1}, ..., \mathbf{d_{k-1}})\, f(\mathbf{A_k} \mid \mathbf{A_{k-1}})\, f[\mathbf{d_k} \mid \mathbf{A_k}]}{\int (...) d\mathbf{A}} \tag{3.18}$$

where $f(\mathbf{A_0}, ..., \mathbf{A_k} \mid \mathbf{d_1}, ..., \mathbf{d_k})$ is the a posteriori state distribution at time k, $f(\mathbf{A_0}, ..., \mathbf{A_{k-1}} \mid \mathbf{d_1}, ..., \mathbf{d_{k-1}})$ is the a posteriori distribution of $\mathbf{A}$ at time k-1, $f(\mathbf{A_k} \mid \mathbf{A_{k-1}})$ is the model evolution from time k-1 to time k given by a first-order Markov process (see eq. 3.1-3.2), and $[\mathbf{d_k} \mid \mathbf{A_k}]$ is the probability distribution of the measurement at time k given the state at that time.

Eq. 3.18 defines the smoother solution over the interval $t \in [t_0, t_k]$ using data vectors $\mathbf{d_1}, ..., \mathbf{d_k}$. In the same probabilistic framework the EnKF equation is derived as

$$f(\mathbf{A_k}|\mathbf{d_1}, ..., \mathbf{d_k}) = \frac{f(\mathbf{A_k}|\mathbf{d_1}, ..., \mathbf{d_{k-1}})\, f[\mathbf{d_k}|\mathbf{A_k}]}{\int (...) d\mathbf{A}} \tag{3.19}$$

Here the information is carried only forward in time and the state at time t_k is dependent on all the previous data $\mathbf{d_1}, ..., \mathbf{d_k}$, meaning that data can be used to obtain updates at different times than the observation times. At the final time k the estimate is identical for the smoother and the filter, while at all previous times the estimate will be suboptimal since future observations have not been used to derive it (Evensen & van Leeuwen, 2000).
Another variant of the EnKF, introduced by Sakov *et al.* (2010), to assimilate observations taken at a time different than the assimilation time is the Asynchronus Ensemble Kalman Filter (AEnKF). The filter is based on the idea of inferring the linearized model dynamics from the ensemble, assuming that the evolution of the corrections and of the ensemble anomalies is linear. In this case in fact, the expansion coefficients of the corrections for the ensemble anomalies remain constant along the forecast system trajectory. Therefore, the transform matrices calculated for assimilation at the time of the observation can be used for assimilation at other timesteps. In this way the AEnKF makes it possible to 'move' the assimilation time of observations without affecting the results.

3.4 The EnKF: limitations

Evensen *et al.* (2007) showed that for a linear model with Gaussian statistics, the analyzed ensemble converges to the correct posterior distribution. Nevertheless, Zafari & Reynolds (2007) investigated the EnKF performance for nonlinear models and multimodal model variable distributions; they showed that in those cases the EnKF fails to capture the structure of the posterior pdf. Section 3.5 provides a background information on the different modifications that can be applied to the standard EnKF in order to achieve a better performance in case of nonlinear problems and non-Gaussian variable distributions.
Another potential limitation of the EnKF is that the solution space investigated is limited to the space spanned by the forecast ensemble, as shown by Evensen (2004). Hence, the ensemble members can be considered as basis functions in the parameter search space. These basis functions should, in principle, span the entire parameter search space, but that would require an

infinite ensemble. In practice, the EnKF forces the state covariance to be of the same rank as the ensemble size, which is in general in the order of magnitude 100, much smaller compared to the number of unknowns in the state vector (variables and state for the reservoir gridpoints) (Anderson, 2009). For this reason, the characteristics of the prior ensemble members (initial parameters and states) and their number (ensemble size) strongly condition the final analysis. Section 3.6 provides an overview of the variations that can be implemented in the EnKF algorithm in order to decrease the sampling errors due to the stochastic nature of the filter. A further limitation of the filter is that it can not handle a number of independent observations larger than the ensemble size (see for references section 3.7); therefore section 3.7 provides a review of all the possible modification to the filter when large amounts of data are available for history matching.

3.5 The EnKF with Non-Gaussian priors and strongly nonlinear systems

The EnkF is particularly efficient when the prior probability distributions are Gaussian and when the relationships between the model parameters, state variables, and observation variables are approximately linear. Violation of even only one of these conditions these two assumptions may introduce severe problems in the model update. This section examines separately different approaches for dealing with nonlinearity in the dynamical system and the complex non-Gaussian distributions for model parameters.

3.5.1 Restarting the simulation

Thulin *et al.* (2007) established consistency between the model forecast obtained from the last data assimilation and the one obtained by rerunning the simulation from time zero. However, this consistency only holds for dynamical systems with no modeling error and where the predicted data are linearly related to the state vector. For the nonlinear problems involved in history matching this consistency fails (Thulin *et al.*, 2007; Evensen, 2009). A rerun from time zero, although computationally demanding in some cases, represents the advantage of eliminating any material balance errors introduced by truncating nonphysical values of saturations or porosities to physically plausible values during the EnKF update. This however at the cost of a potential divergence between the optimal solution obtained with the EnKF and the resulting model after the re-run. Chapter 6 shows an example of a rerun experiment after the assimilation of time-lapse data.

3.5.2 Parameterization to ensure Gaussian distributions and Particle Filter

In order to avoid non-normal variable distributions in the EnKF update, applying upfront a Gaussian transform to such variables is the most common and intuitive procedure to improve the filter performance.
Bertino *et al.* (2003) changed strictly positive and strongly skewed concentrations of phytoplankton into a nearly Gaussian distributed variable by using a log-normal transformation: it resulted in an improved filter performance. zha (n.d.) used a similar approach by applying a normal score transform to water saturation before updating it. This helped to avoid unphysical updated values.
Jafarpour & McLaughlin (2007a) and Jafarpour & McLaughlin (2007b) introduced the use of the discrete cosine transform (DCT). The DCT allows to reduce the number of basis functions by retaining only the ones with higher weights. The weights are established according to the prior information, emphasizing large-scale events like channels or long range high permeability structures. The advantage introduced by this technique is a reduction in computational costs for the EnKF, extremely useful for real time applications when working with large models.
Gu & Oliver (2006) replaced water saturation in the state vector with a geometrical variable locating the position of the water front. The result for a 1D model showed improved saturation updates. Chen *et al.* (2009) further developed this idea, replacing the saturation values for gridblocks at the waterfront (with bimodal distribution) with the water-phase arrival times for the same gridblocks. Because arrival times is quasilinearly related to the petrophysical properties of the reservoir (Wu & Datta-Gupta, 2002), this parameterization ensures a Gaussian distribution of the variables in the state vector. As the variable distribution becomes similar to a Gaussian function then using saturation data, results show improved an model update, with no abnormal saturation values, with respect to the case where no parameterization is applied. Chapter 6 shows an example of a similar approach where observed saturation data coming from seismic inversion are parameterized into waterfront arrival times.
Another approach that has been proposed to get a correct sample of the posterior distribution, in case of distributions which are not simply described by a Gaussian curve, is the Particle filter (Doucet *et al.*, 2001). In this method a set of "particles" (ensemble members) are sampled from the forward model, then each particle receives a weight proportional to the ratio between the joint posterior density function and an 'importance function'. The update

for each particle is then obtained using the standard EnKF formula: hence, the EnKF can be seen as a particle filter restricting the weights to be uniform. The mentioned importance function's role is to slightly distort the posterior density function in order to capture non-Gaussian features in the distribution. However, weights have to remain as close as possible to one, in order to preserve the main analyzed state characteristics. A shortcoming of particle filters is the difficulty of locating particles in regions of high likelihood when the dimension of the model space is large (Aanonsen *et al.*, 2009). Furthermore Gordon (1993) proved that the weights converge to zero after a few time steps. No applications to large-scale systems have been published.
Improvements to this filter have been proposed in literature. Stordal *et al.* (2011) presented a way to avoid the collapse of the weights by forcing them to be uniform with an artificial increase of the uncertainty associated with each particle. This means that each sample, or weight, is smoothed with a Gaussian density leading to the 'Gaussian mixture filter'. A recent development of this type of filter is the adaptive Gaussian mixture filter (Anderson & Moore, 2005; Bengtsson *et al.*, 2003; Kotecha & Diurić, 2003). The difference with the Gaussian mixture filter is the introduction of a tuning parameter $\alpha \in [0, 1]$. The condition that $\alpha = 0$ gives the uniform weights of the EnKF and reduces the weight degeneracy problem, while with $\alpha = 1$ weights are the same as in the Gaussian mixture filter leading to a better preservation of non-Gaussian features of the marginal distributions. The approach is 'adaptive' as an optimal α is sought at each assimilation step.

3.5.3 Iterative ensemble filters

When the relation between model and observation variables becomes strongly nonlinear the EnKF might lead to unphysical updates. Obviously truncation represents the simplest, but not very elegant solution. Fortunately, more sophisticated alternatives, like iterative methods have been introduced. Most iterative forms of the EnKF can be viewed as algorithms that minimize a stochastic objective function or, equivalently, maximize the posterior conditional probability distribution of the ensemble.
Zupanski (2005) proposed an ensemble maximum likelihood filter for general nonlinear observations. The ensemble method is used to approximate the Hessian and the gradient of the objective function in the subspace spanned by the ensemble. The iteration avoids non-physical results which would be caused by a single large update step.
Motivated by this study Reynolds *et al.* (2006) and Li & Reynolds (2009) introduced an iterative method that attempts to generate realizations of the

reservoir model parameters at each time-step by solving an iterative equation. In each iteration it is necessary to perform one forward simulation from time zero to the current assimilation timestep and one solution of the adjoint system backward from the current assimilation timestep to time zero in order to compute the gradient of the objective function at each iteration step. During each iteration, the ensemble is used to approximate the Hessian of the model variables to update. As each ensemble uses a separate gradient computed locally, the method is able to preserve multipoint statistics. Gu & Oliver (2007) proposed an iterative ensemble method a bit different from the previous ones as it uses in the iterations the ensemble to compute the sensitivity matrix. The result is that the method does not require an adjoint code to compute gradients, but it uses one descend direction for all the realization.
Lorentzen & Naevdal (2011) proposed an iterative EnKF based on the iterated EKF (Lefebvre *et al.*, 2004) In this approach the measurement model is linearized around the analyzed state estimate. The predicted measurements are expressed as function of the updated model parameters and state variables to produce updated and improved simulated measurements. Although results from simple models show for this approach a more accurate update than obtained with the EnKF, the method is not usually applicable as the observational model is usually not known.
Other examples of Iterative filters are the "Iterative Ensemble Filter for Plausibility" (Wen & Chen, 2006, 2007; Gu & Oliver, 2006). In these methods, the estimates of model parameters are iteratively updated using the simulator to forecast from the last assimilation time k-1 with the state variables obtained at time k-1 and new model parameters at time k. Although the approach ensures physically plausible state variables, it is difficult to justify as it updates model parameters but not the state variables at the previous assimilation time.

3.6 Adjusting the EnKF to reduce sampling errors

3.6.1 Resampling

Evensen (2004) showed that the EnKF analysis can be expressed as a linear combination of the different ensemble members. Hence, these represent the initial parameter search space and should in principle be infinite. For computational reasons the ensemble has to remain finite and relatively small. However, Evensen (2004) introduced a method aiming at increasing the solution space. It consists in generating a large number of realizations

and selecting the initial ensemble from singular vectors associated with the largest eigenvalues of the approximated covariance. In this way, remarkable improvements in the EnKF update were achieved while keeping the ensemble size constant. One problem with this approach is that the property realizations in the initial ensemble might be relatively smooth and not necessarily consistent with the prior geological model. Evensen (2004) also suggested a rescaling to obtain the correct variance. An application of this approach for reservoir models is presented in Oliver & Chen (2009).

3.6.2 Square-Root Filters

Basic EnKF may introduce sampling errors because of the stochastic perturbations added to the observations. However, these sampling errors can be avoided by performing the update of the ensemble mean separately from the ensemble perturbations update (Evensen, 2004). This is the idea behind Ensemble Square-Root Filters (EnSRF) (see Whitaker & Hamill (2002), Tippett *et al.* (2003), Evensen (2004)). In these filters while the ensemble mean is updated according to the standard approach, the analyzed ensemble anomalies are obtained through factorization of the theoretical analysis covariance matrix, assumed to be known in advance. This approach results in no perturbation added to the measurements and in a reduced tendency for the analysis pdf to become Gaussian after few updates (as Lawson & Hansen (2002) empirically found). Another empirical finding is that analysis may become progressively skewed (Lawson & Hansen, 2002; Leeuwenburgh *et al.*, 2005) even when symmetric transformation matrices are applied (Sakov & Oke, 2008). It has also been noticed that the analyzed ensemble may collapse into one single state as a result of a single outlier; fortunately this problem can be avoided by using a simple randomization (Leeuwenburgh *et al.*, 2005). Wang *et al.* (2004) noted that some solutions for generating the ensemble anomalies do not preserve the ensemble mean during the transformation. Therefore, Sakov & Oke (2008) recommended that only mean-preserving transformations should be used with EnSRF.

3.7 The EnKF and large amounts of data

When the number of observations to assimilate is large, i.e. when assimilating 3D or time-lapse seismic data, two major problems occur with the basic EnKF method: (1) It is not computationally feasible to compute or invert the matrix $\left(\mathcal{H}\mathbf{P}^{\mathbf{f}}\mathcal{H}^{\mathbf{T}} + \mathbf{R}\right)$ in the Kalman gain (see eq. 3.10), and (2) as discussed in section section 3.6, each updated ensemble member is a linear

combination of the corresponding initial members, so there are no sufficient degrees of freedom to properly assimilate data when the number of independent data is larger than the ensemble size.
Although this problem could be eliminated by using a large ensemble, efficiency requires an ensemble relatively small. A very effective approach to improve the EnKF efficiency when dealing with large amounts of data is using localization methods: the two most common localization methods are the local analysis and the covariance localization. Local analysis (Sakov & Bertino, 2011), consists of setting ensemble anomalies outside a certain local window to zero during the update, while covariance localization consists of setting to zero part of the covariance matrix during the update. The other approach is covariance localization which consists of multiplying the ensemble covariances element-wise (Hadamard or Schur product) by a local support matrix $\mathcal{C}$ resulting in a localized covariance estimate.
Covariance localization seems to provide an improved update with respect to local analysis (Sakov & Bertino, 2011); furthermore, covariance localization methods were first introduced in literature (Houtekamer & Mitchell, 1998) and enjoy a broader and progressively growing attention. For those reasons it has been chosen in this thesis as a method to improve the EnKF performance for the assimilation of large time-lapse (seismic) datasets.

3.7.1 Covariance Localization

Covariance localization allows updates to use a different linear combination of realizations for each grid cell. For this reason the global update can be obtained from a much larger space than just the span of the ensemble realizations (increase in the effective ensemble size). The other primary reason behind localization is the reduction of spurious correlations in the ensemble covariances which can be explained as sampling artifacts induced by the limited ensemble size (Mysrseth *et al.*, 2012).
In the earliest applications (Houtekamer & Mitchell, 1998) the localized EnKF update reads:

$$\begin{aligned}\mathbf{A^a} &= \mathbf{A} + \left(\mathcal{C}_{\mathcal{A}'\mathcal{A}'} \circ \mathbf{A}\mathbf{A}'^{\mathbf{T}} / (N-1)\right) * \\ &\quad \mathbf{H^T}\left(\mathbf{H}\left(\mathcal{C}_{\mathcal{A}'\mathcal{A}'} \circ \mathbf{A}'\mathbf{A}'^{\mathbf{T}} / (N-1)\right)\mathbf{H^T} + \mathbf{R}\right)^{-1}(\mathbf{D} - \mathbf{H}\mathbf{A})\end{aligned} \tag{3.20}$$

Where for simplicity we assume here a linear measurement operator $\mathbf{H}$ as in the referred papers.
In later applications (Houtekamer & Mitchell, 2001; Fertig *et al.*, 2007), it

was assumed that:

$$\left(\mathcal{C}_{\mathcal{A}'\mathcal{A}'} \circ \mathbf{A}\mathbf{A}'^{\mathbf{T}}/\left(N-1\right)\right)\mathbf{H}^{\mathbf{T}} \approx \mathcal{C}_{\mathcal{P}\mathcal{H}} \circ \mathbf{P}^{f}\mathcal{H}^{T} \tag{3.21}$$

and that

$$\mathbf{H}\left(\mathcal{C}_{\mathcal{A}'\mathcal{A}'} \circ \mathbf{A}\mathbf{A}'^{\mathbf{T}}/\left(N-1\right)\right)\mathbf{H}^{\mathbf{T}} \approx \mathcal{C}_{\mathcal{H}\mathcal{P}\mathcal{H}}\mathbf{H}\mathbf{P}^{\mathbf{f}}\mathbf{H}^{\mathbf{T}} \tag{3.22}$$

It can be noted that the dimensions of the compact support matrices $\mathcal{C}$ are inconsistent in these expressions (Chen & Oliver, 2010). However, these assumptions may hold if most types of measurements have compact support much smaller than the localization range (Leeuwenburgh *et al.*, 2011).
When these assumptions hold, it can be noted that localization applied on the model-error covariance matrix becomes equivalent to localization applied on the matrix of ensemble covariances between state/parameters and measurements and on the ensemble covariance matrix of predicted outputs. This allows the use of localization with non-linear model propagation and it does not require the calculation of the model error covariance matrix, usually very large (Leeuwenburgh *et al.*, 2011). For this reason in the mentioned papers and in other later studies -like in Hamill *et al.* (2001) and Keppenne & Rienecker (2002), among others- localization has been applied to ensemble covariances.
Another modification, introduced in later applications (Houtekamer & Mitchell, 2001; Keppenne & Rienecker, 2003; Bertino *et al.*, 2003; Houtekamer & Mitchell, 2005), is the replacement (in the local support matrix $\mathcal{C}$) of the sharp cutoff (binary matrix) with a tapering de-correlation function: this is a scalar, compactly supported, positive, monotonically decreasing function which takes values between zero and one (Gaspari & Cohn, 1999). In this way sharp discontinuities in the updates have been eliminated.
Hamill *et al.* (2001) investigated the effect of noise in the analysis estimate. They also computed the eigenvalues of the estimated covariance matrices with different localization regions showing that these become full rank if localization is applied. Lorenc (2003) showed that when the Gaspari-Cohn correlation function is used for localization, the optimal choice regarding the localization radius increases as the ensemble size increases. For this reason Furrer & Bengtsson (2007) contributed to solving the problem of estimating an optimal distance-dependent localization function. Their approach involves the minimization of the difference between the true covariance matrix and the localized ensemble estimated covariance. Results showed that the optimal localization function determined by this method, depends on two crucial factors: (1) The true covariance structure, and (2) the ensemble size. For

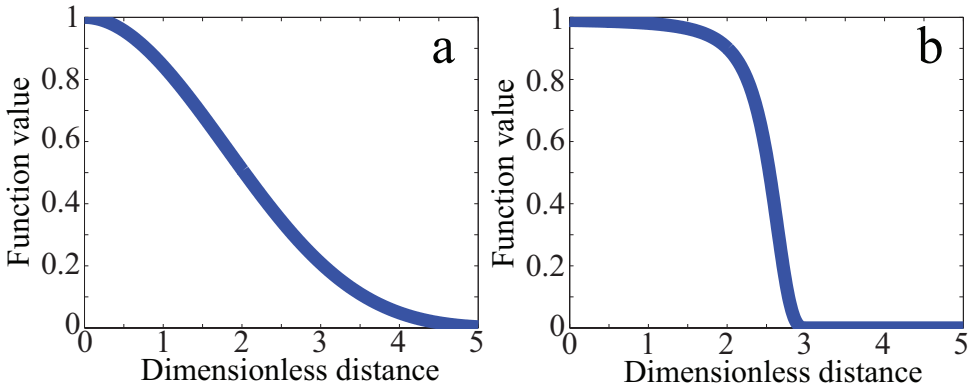

Figure 3.1: *Monodimensional behavior of Gaspari-Cohn (plot a) and of Furrer-Bentson (plot b) function. For the second function the ensemble size N is set to 100 and the true covariance has exponential variogram. Both the expressions depend on the variable* c*. In both these examples* c *is set to 3. Gaspari-Cohn presents a gentler slope, but Furrer-Bengtson presents a more extended high value plateau.*

a mathematical derivation the reader can also check Aanonsen *et al.* (2009) and Schulze-Riegert *et al.* (2009).
Figure 3.1 compares the Gaspari-Cohn localization function with the function later introduced by Furrer-Bengtson (estimated using an exponential variogram and an ensemble of 100 members). Both functions depend on a single-length factor indicated with "c". In Gaspari-Cohn the value of c corresponds to the distance at which the function decreases to the value of 0.2; in Furrer-Bengtson, the value of c corresponds to the distance at which the function drops to zero. In both these examples c is set to 3. Gaspari-Cohn curve presents a gentler slope, but Furrer-Bengtson presents a more extended high value plateau, allowing for stronger updates. For this reason, and for its dependence with the ensemble size and real correlation pattern, this Furrer-Bengtsson function is often preferred in recent distance-dependent localization studies (Chen & Oliver, 2010) as in this thesis.

3.7.2 Application in Reservoir Engineering

In reservoir engineering applications, localization is often applied directly to the Kalman gain instead of on the covariance matrixes (Chen & Oliver, 2010; Devegowda *et al.*, 2007; Arroyo-Negrete *et al.*, 2006; Chen & Oliver, 2009);

in this case the EnKF update reads as:

$$\mathbf{A}^a = \mathbf{A} + \mathcal{C} \circ \left(\mathbf{P}^f \mathcal{H}^T \left(\mathcal{H} \mathbf{P}^f \mathcal{H}^T + \mathbf{R} \right)^{-1} \right) (\mathbf{D} - \mathcal{H}\mathbf{A}) \,. \tag{3.23}$$

In reservoir engineering, the earliest applications of covariance localization are from Skjervheim *et al.* (2007), and Dong *et al.* (2006). In both studies, localization has been used for the assimilation of seismic data. Dong & Oliver (2003) showed, using a simple 2D model, that the combination of seismic data (as P-wave impedances) and production data resulted in a better estimation of those static properties than in the case where only production data were used. In particular, the porosity estimate was more accurate than the permeability estimate when using seismic data. This is due to the fact that P-wave impedances are more related to porosity than permeability. Skjervheim *et al.* (2007) used a distance dependent localization that allowed updating over a larger region. The authors did not discuss the choice of the distance range, but they showed that decreasing the template size makes the ensemble spread increase. Arroyo-Negrete *et al.* (2006) and Devegowda *et al.* (2007) chose a different procedure to decide the localization regions. In their papers, the areas of influence for production rates were not decided according to distance criteria but based on the traveltime sensitivity to the reservoir gridpoint permeability, calculated along the streamlines connecting each injector to the related producers. This streamline-based covariance localization has the benefit of preserving prior geological information, retaining the non-Gaussian distribution from the initial model. Trani *et al.* (2009b) and Trani *et al.* (2009a) used streamlines to identify localization regions for time-lapse saturation and pressure data. Agbalaka & Oliver (2008) applied the EnKF to adjust facies boundaries in a 3D model. Facies constraints were iteratively enforced using the Gaspari-Cohn distance-dependent localization of the Kalman gain to update the Gaussian random fields for facies.

3.7.3 Covariance Localization: limitations and Improvements

Although covariance localization has been proven successful in many studies, as described in the previous section, it presents some drawbacks as well. This section describes the limitation of the approach and how it can be made more efficient.

Hacker *et al.* (2007) used a Gaspari-Cohn localization function with optimized range parameter for a weather forecast application. They found that the optimal localization range varied with the time of the day. Hence, they concluded that localization based on distance alone in a system with multiple

data and state types is of questionable value.
Kepert (2009) showed that although localization filters out covariance at large scale, it does not change the total variance; the consequence is a net gain of covariance at small scale. Hence, localization can not be regarded simply as a high-pass filter. This distortion in the variance introduced by localization is likely to generate imbalance in the analysis, as reported by Houtekamer & MItchell (2006). Another localization drawback, is that it can only be applied on spatially correlated variables; in fact, if it is applied on spatially uncorrelated variables (like oil-water contact or fault transmissibility multipliers) the EnKF localization might have a detrimental outcome (Zhang & Oliver, 2011a).
The adaptive localization approach has been introduced to improve the classical EnKF localization method (Hunt *et al.*, 2007). In this method in fact, each grid-point is treated independently and updated with different sets of observations, like in the classical approach; however, the measurement error matrix R is weighted by the localization factor, so that far-away, uncorrelated measurements have large errors (R-localization).
From the previous paragraphs it is obvious that the major challenge associated with localization, is the selection of an appropriate localization region, in order to remove the spurious correlations without eliminating the true ones. Therefore, localization in order to be effective would require an a priori knowledge of the true covariance of model variables with measurements (Zhang & Oliver, 2011a). Chen & Oliver (2010) and Emerick & Reynolds (2010) defined appropriate localization functions to apply to the covariance matrix between model variables and production data. They proved that the region of influence depends on the prior covariance for the model variables, on the past history of data assimilation, and on the reservoir structural geology. The results show that choosing for each measurement a localization function including the real correlations only, the localized EnKF update is much more accurate than the traditional approach. In fact, with the use of localization, the filter divergence is avoided, the permeability is correctly estimated, and the quality both of the history match and of the production forecast improves.
The next chapter presents a study similar to the one described in Chen & Oliver (2010). The difference is that in our approach the covariance of model parameters and states with 4D seismic observations is analyzed, instead of the covariance of variables with production data. Time-lapse seismic measurements considered are typically those resulting from the inversion scheme proposed in chapter 2(ΔS and ΔP). The aim of this study is to find localization functions which include the region of non-zero cross-covariance only.

Results show that the covariances mainly depends on the geological structure (permeability field), on the well pattern and flow dynamics; furthermore, as saturation and pressure are state variables, their cross-correlations with seismic measurements change in time. In the next chapter, these localization functions will be used to condition the EnKF update in case a large number of seismic observations is available; the effect of knowing a priori the true cross-covariances will be evaluated.

3.7.4 Alternatives to Covariance Localization

The first alternative approach to covariance localization to deal with large amounts of data was introduced by Evensen (2004); Evensen *et al.* (2007); Skjervheim & Ruud (2006); Skjervheim *et al.* (2006). In these papers the authors used a subspace EnKF inversion scheme in which data mismatches and simulated measurement errors are projected onto the subspace spanned by the principal left singular vectors of $\mathcal{H}(\mathbf{A})$ However, with this method, there is no guarantee that the updated model parameters will honor all the measurements, therefore the update accuracy is much smaller than the one obtained by using a larger ensemble.
Other alternatives to covariance localization are more recent.
Anderson (2007) proposed a filter for arbitrary localization functions that do not necessarily decrease monotonically with distance from the observation point. The tuning ensemble used to estimate localization functions must be several times larger than the normal ensemble (for this reason called 'Hierarchical filter'). The procedure requires generation of 3-5 ensemble of the normal size. A regression coefficient is estimated for each variable-observation pair in each ensemble. The mean and the variance of the regression coefficient are used to compute a regression confidence factor (RCF) for each variable-observation pair. The set of RCFs for each observation form a regression confidence envelope, which can be thought of as a sort of localization.
Vallés & Naevdal (2009) applied the hierarchical filter by Anderson (2007) on the Brugge field (Peters *et al.*, 2009). They gave recommendations on the number of ensembles and the size of each individual ensemble, the product of which is the number of the simulation runs required by this method. As this number is quite prohibitive, practical implementations of the method are limited.
Zhang & Oliver (2011b) and Zhang & Oliver (2011a) used a similar idea as the hierarchical filter to stripe out spurious correlations. They also created multiple ensemble groups for as many estimates of the Kalman gain. The difference with Anderson (2007) is that they used bootstrap sampling

(repeated sampling method from the parent data to compute the statistics of interest) in order to generate new ensemble realizations. For every ensemble the Kalman gain is calculated. For every variable-observation pair, or equivalently every entry in the Kalman gain, a distribution of the values is calculated. Outliers, results of spurious correlations, are assigned a damping factor, proportional to the deviation from the mean distribution value. The advantage of such screening methods is the regularization of the Kalman gain without applying the concept of distance. The consequence is that they can be applied to non-spatially dependent variables, like relative permeabilities, fluid-contacts etc..
A method used frequently in weather and oceanography applications to maintain the ensemble variability in case of a large amount of data is Covariance Inflation (Anderson, 2009), although its use in petroleum engineering is rare. Chen & Oliver (2009) showed preliminary results on covariance inflations and the combined use with covariance localization on the Brugge field. They proposed that the region for the covariance inflation at a particular assimilation time should be chosen as the union of all the localization regions for that time, with the magnitude of the inflation factor determined by the sum of the localization functions. As a consequence, the actual inflation applied varies in time and in space.

3.8 Conclusions

This chapter provides an introduction to the EnKF algorithm, which will be used in this thesis to update the reservoir model from observed data. This chapter also provides an overview of the modifications proposed in literature applied to the standard EnKF procedure. Those adjustments are addressed to specific issues causing malfunctioning of the filter like:

- Sampling errors
- non-linearity in the model
- non-Gaussianity in the prior model variable distribution
- assimilation of large amounts of data

The following chapters of this thesis aim at improving the EnKF update performance in case of the assimilation of 4D seismic data. In general, when seismic data are assimilated, the issues of non-Gaussianity and large amounts of data, indicated by the last two bullet points, are of importance.

Chapter 4

Covariance Localization analysis and 2D Results

The previous chapter introduced the EnKF algorithm and the covariance localization approach to improve the performance of the filter when large amount of data have to be assimilated. The difficulty with covariance localization is essentially that it requires localization functions large enough to include the true regions of non-zero cross-covariance but small enough to enlarge the effective solution space. Hence, localization, in order to be effective, would actually require some knowledge of the real covariances which is not the case in real case studies. The first part of this chapter shows an analysis of the covariances between model variables and time-lapse seismic measurements like changes in fluid saturation and in pore pressure for a synthetic case. The objective is to build guidelines for defining localization functions for the effective assimilation of time-lapse seismic observations. In the second part of the chapter, these guidelines will be used to regularize the covariances in the Kalman gain in case time-lapse seismic surveys are frequently applied.

4.1 Introduction

The first part of the chapter takes its main idea from the work presented in Chen & Oliver (2010). In this study the authors analyzed the ensemble-based covariance for model parameters like permeability and model states like water saturation and pressure with well production measurements like bottom-hole pressures (BHP), oil and water-rates (OR and WR) using a 2D model with a repeated five-spot well pattern. Results showed that the regions of non-zero cross-covariances extend further than a single five-spot area. Emerick &

Reynolds (2010) deepened the work of Chen & Oliver (2010) by proposing, for the assimilation of production data, large localization regions equal to the sum of the drainage area plus the permeability correlation length. The first part of this chapter can be considered as an extension of these two previous studies. In fact, it aims at building guidelines for the definition of localization functions to apply on distance- based localization of model variables covariances with time-lapse changes in saturation and in pressure. The work presented in this thesis is done on a similar model as in the mentioned studies: a 2D model with a repeated five-spot pattern.
The second part of the chapter shows the results of an analysis carried out on a 2D synthetic reservoir model (similar to the one used for the covariance analysis) demonstrating the effects of a perfect vs. an imperfect localization on EnKF updates. The standard approach without any localization is compared to two localized updates: In the first case the localization functions as recommended by the covariance analysis in the first part of the chapter are used; in the second case the localization radius is chosen too small, a situation that could easily occur in a real case where the true covariance is unknown. The effect of a localization radius chosen too large has not been investigated separately, since this corresponds to some extent to the base case, where no localization is performed at all. The aim of this exercise is to illustrate the effect of a priori knowledge of the covariance appearing in the Kalman gain on the reservoir state estimation. In the next chapter, the recommended localization functions for the cross-covariance regularization in the Kalman gain will be applied on a 3D synthetic model, larger and more realistic than the one used in this chapter.

4.2 Cross-Covariance analysis

4.2.1 Introduction

The study of the true correlations between model variables and observations may help in building compact support functions for an appropriate localization of the covariance matrix appearing in the Kalman gain. In this section, the covariances between model variables and simulated seismic measurements (ΔS and ΔP) are analyzed. The cross-covariances are computed from a large ensemble of 1000 members, all created with the same statistics, in order to approximate the truth covariances. The correlations are analyzed for two different ensemble groups created with different variograms and at different production stages. These are: an early time of 400 days, which is before the water breakthrough occurs for all the producers, an intermediate time of 850

days, which corresponds to a time shortly after all the reservoir producers experience some water breakthrough, and a late time of 1300 days, when the water production is in the same order as the oil production. The objective is to evaluate the cross-correlations as the water invades the reservoir.
The basis is a 61 x 61 gridblock synthetic reservoir model, where each gridpoint measures 33 x 33 x 10 m. The reservoir has a five-spot well pattern -with one injector and four producers at the corners- repeated 9 times, leading to a total of 9 injectors and 16 producers.
Two groups of ensembles were created with the aim of evaluating the impact of the geological structures on the localization functions. The porosity for both the ensembles is kept constant with a value of 0.3; the (logarithm of the) permeability for the first ensemble group (A) consists of 1000 unconditioned, sequential Gaussian simulations using an isotropic, exponential variogram with a range of 10 gridblocks and nugget effect equal to 1. The permeability for the members of the second group (B) are sequential Gaussian, unconditioned simulations with anisotropy introduced by a variogram with an azimuth of 45°W. The variogram has the same correlation length and nugget effect as used for ensemble A. For both of the ensembles the logarithm of permeability has a mean of log(125)md and a standard deviation equal to log(0.05) md. Figures 4.1 and 4.2 show two realizations from ensemble A and B, respectively. The positions of the wells are also indicated.

4.2.2 Analysis before water breakthrough

The next figures show the correlations (covariances rescaled by the product of the standard deviations of model variable and observations) between the two types of seismic measurements and the three model state/variables (permeability, water saturation and pressure). The correlations are calculated before water breakthrough has occurred in any of the producers. The seismic measurements are changes in water saturation and in pressure (ΔS and ΔP) between time 0 and time 400 days. During the simulations, water injection occurs simultaneously to oil production, the producers are controlled by fixed bottom-hole pressures (BHP) and injectors are constrained to fixed liquid rates.
Figure 4.3 shows the correlation between seismic measurements at the gridpoint indicated by a black diamond and the log-perm. Plots a&b indicate the correlation between ΔS and log-perm for ensemble A and B, respectively. The cross-correlation is positive between the injector and the observation gridpoint, up to its closest producer; the correlation is negative on the opposite side of the injector and around the other producers of the same

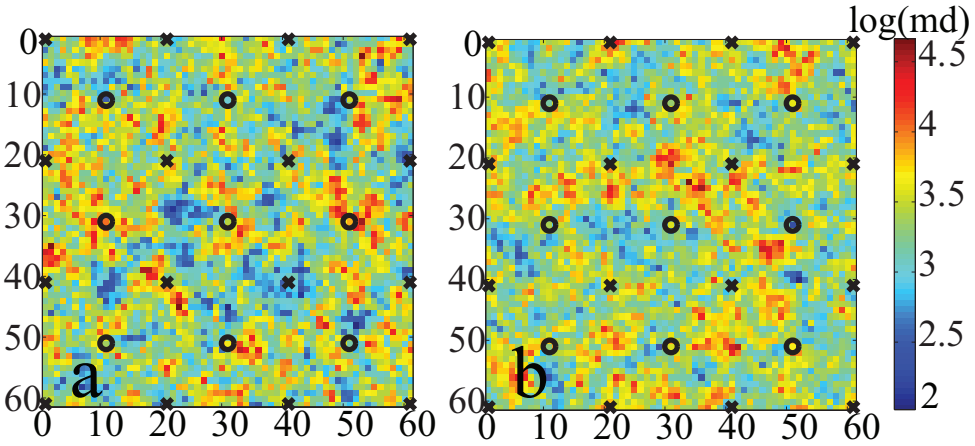

Figure 4.1: *Two realizations from ensemble A. All the realizations are created using the same isotropic variogram. The black rounds indicate the position of the injectors and the black crosses the position of the producers. The number denote the gridpoint coordinate in the X− and Y− directions.*

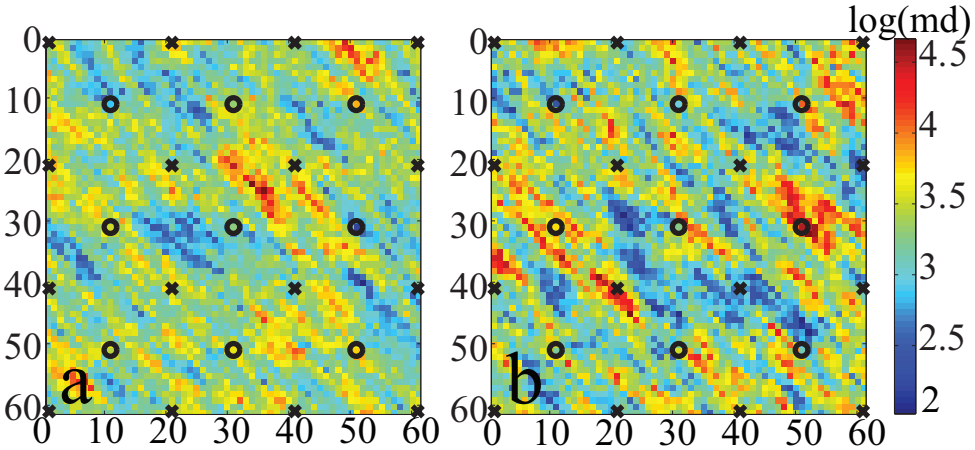

Figure 4.2: *Two realizations from ensemble B. All the realizations are created using the same variogram having azimuth of 45° W. The black rounds indicate the position of the injectors and the black crosses the position of the producers. The number denote the gridpoint coordinate in the X− and Y− directions.*

five-spot pattern. In plot b the structure of the correlation is similar, except that the permeability anisotropy tends to distort the correlation pattern in the same direction of the permeability azimuth. The negative correlations on the opposite side of the injector appear also to be more stretched. This is explained by the fact that the correlation length used in the variogram to built ensemble B is larger than the correlation length used for ensemble A. For these examples, since injecting wells operate at fixed injection rate, increasing the permeability in the region of the drainage area around the seismic measurement increases the flow rates towards that point. Furthermore, because of the mass conservation law, if the water flow increases towards the measurement location, it must decrease on the opposite side of the injector (Emerick & Reynolds, 2010). Although the sensitivity is highest near the measurement location (drainage area), the localization function necessary for an appropriate update, should not ignore the other producers: it should be as large as the five-spot pattern.
Plot c illustrates the correlation between log-perm and ΔP observed at the same point as in the previous plots (black diamond). The correlation with the permeability is negative around all the producers draining water from the closest injector, with a negative peak around the closest producer. This can be explained as follows: as producers are constrained to fixed BHP, a decrease in permeability around these wells would render the water drainage more difficult. Since the injectors operate at fixed WR, this decrease in water drainage would contribute to a pressure build-up in all the five-spot well patterns, including the measurement location. Plot d shows the same correlation but now calculated with ensemble B. Also in this case, the azimuth and the correlation length of the permeability variogram cause, respectively, a reorientation and a stretch of the correlations.
Figure 4.4 illustrates the correlation between ΔS and ΔP (calculated at the same point as in the previous figures) with the water saturation field. The correlations are shown both for ensembles A and B, in the same order as in the previous figures. Plot a shows the correlation between ΔS at the black diamond and the water saturation, and it is calculated using ensemble A. In all plots of figure 4.4 the circular structures reflect the position of the oil-water front after 400 days. The correlation is clearly positive from the injector up to the measurement gridpoint, and negative on the opposite side of the producer. This correlation can be explained by the fact that since the injector is constrained to a fixed water rate, an increase in saturation towards the measurement point and its closest producer means, because of the mass balance, a decrease in water flow towards the other producers of the same five spot pattern. A similar correlation structure is observed in ensemble B

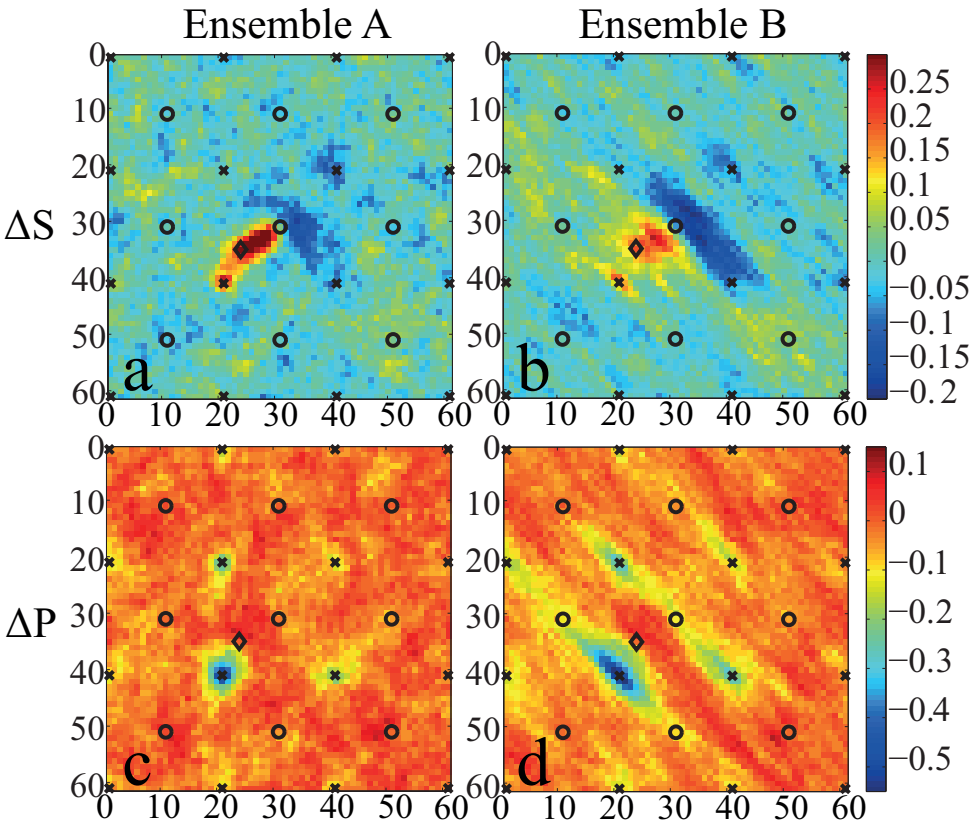

Figure 4.3: *Cross-correlation between the logarithm of permeability and seismic measurements at the location indicated by the black diamond. Plot a presents the cross-correlation between ΔS and log-perm, calculated with ensemble A; plot b shows the same cross-correlation calculated with ensemble B. Plot c presents the cross-correlation between ΔP and log-perm, calculated with ensemble A; plot d shows the same cross-correlation calculated with ensemble B. The numbers denote the gridpoint coordinates in the $X-$ and $Y-$ directions.*

(plot b). This correlation structure reflects the correlation of saturation with water injection rate and and oil production rate presented in Chen & Oliver (2010): positive between the injector and the producing well, negative in the rest of the five-spot pattern.
In the second row, plot c shows the correlation between ΔP and the saturation field. The structure of the correlation reflects the general position of the water fronts advancing from the injectors and its value is very negative in the undrained area next to the producers. Plot d shows a similar correlation structure, note that the waterflooded areas present a more elliptical shape, with respect to plot c, due to the anisotropic permeability.

Figure 4.5 displays the correlation of seismic measurements with the pressure field for ensemble A and B, in the same order as in the previous pictures. Plot a shows the correlation, calculated with ensemble A, between ΔS at the black diamond and the pressure field. The area of non-zero correlation is very large and choosing a localization function for this covariance seems to be a difficult task. The same conclusion can be drawn as for the covariance calculated with ensemble B (plot b). At the bottom row, plots c&d illustrate the correlation of ΔP at the black diamond with the pressure field. The (auto-)correlation monotonically decreases with distance but nowhere approaches zero, making the choice for a localization function rather difficult. The permeability anisotropy does not seem to affect this correlation pattern strongly (plot d).

4.2.3 Analysis during and after water breakthrough

As shown by Chen & Oliver (2010), the cross-correlations of model variables with production measurements, or at least the length of the true correlations (which defines the localization radius) do not change between a time shortly after the water breakthrough for all the reservoir producers (intermediate time) and a later stage (late time). The same is observed for cross-covariances between model variables and seismic measurements. For this reason, only the covariances calculated at the intermediate time will be shown.
Figure 4.6 shows the cross correlation of seismic measurements with log-perm, in the same order as in figure 4.3. The comparison between these figures suggests that, in general, the structure of these correlations does not change much after wells experience water breakthrough (note that permeability is a parameter, therefore time-independent). However, looking carefully at the correlation of log-perm with ΔS (plots a&b) it can be noticed that the negative correlations around the producers located on the opposite side of the injector with respect to the measurement point seems to be a bit lar-

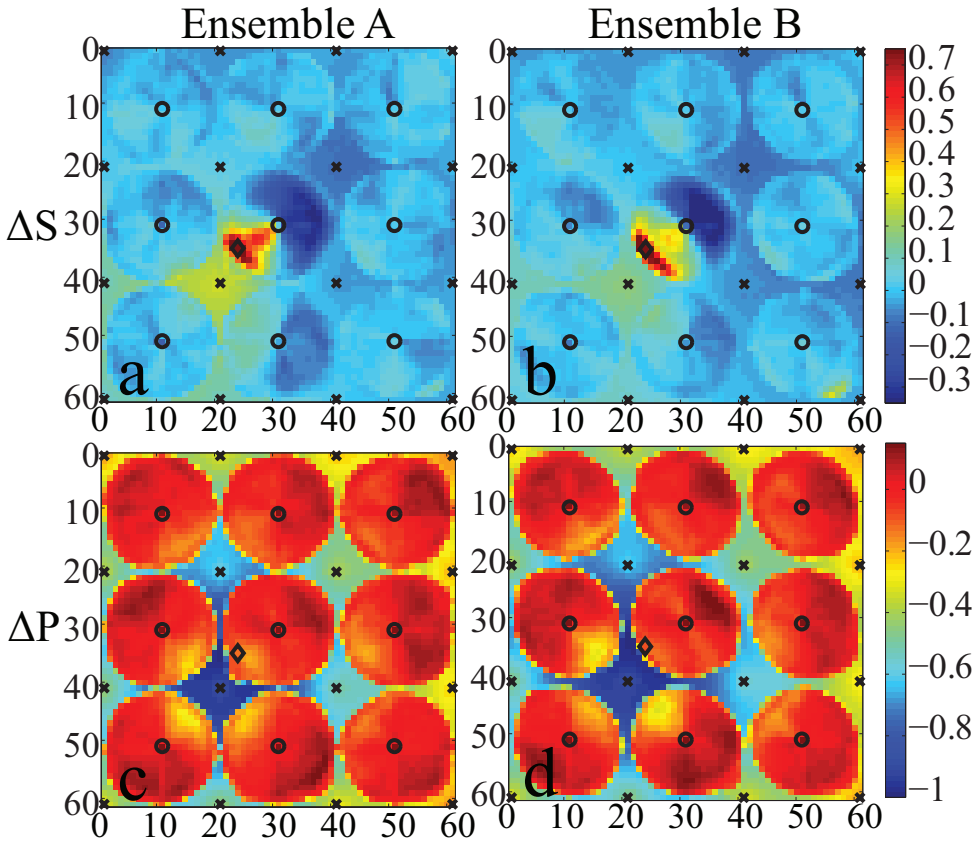

Figure 4.4: *Cross-correlation between the water saturation and seismic measurements at the location indicated by the black diamond. Plot a presents the cross-correlation between ΔS and water saturation calculated with ensemble A; plot b shows the same cross-correlation calculated with ensemble B. Plot c presents the cross-correlation between ΔP and satuation, calculated with ensemble A; plot d shows the same cross-correlation calculated with ensemble B. The numbers denote the gridpoint coordinates in the $X-$ and $Y-$ directions.*

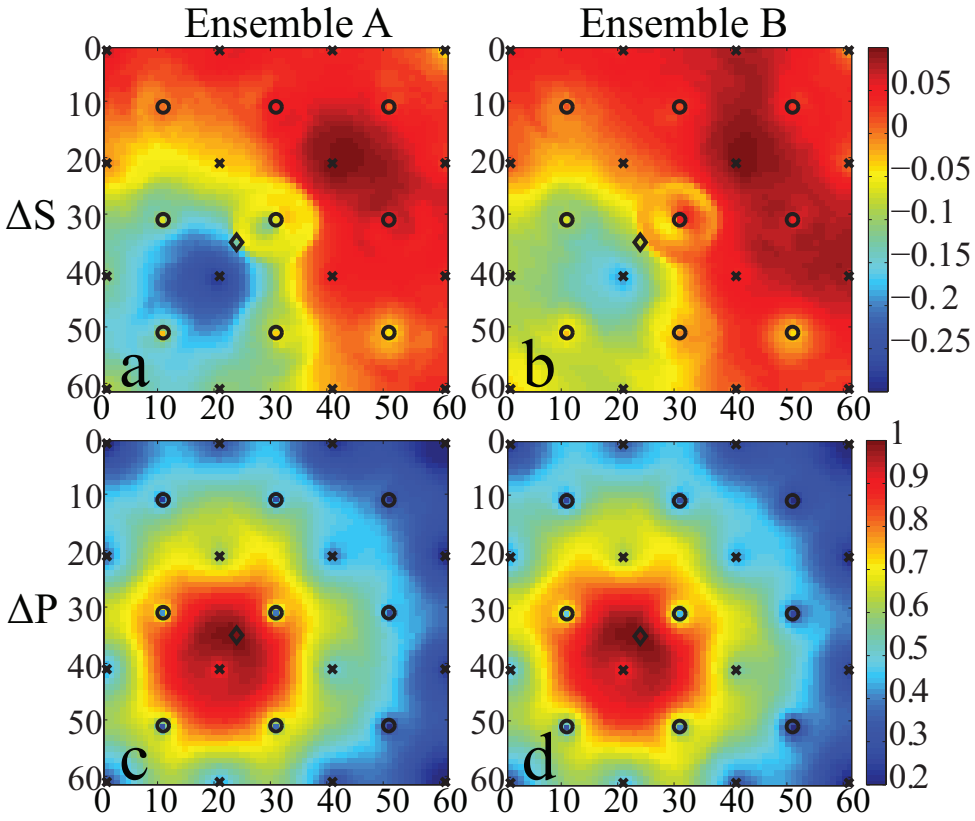

Figure 4.5: *Cross-correlation of the pressure field with seismic measurements at the location indicated by the black diamond. Plot a presents the cross-correlation of ΔS with pressure, calculated with ensemble A; plot b shows the same cross-correlation calculated with ensemble B. Plot c presents the cross-correlation of ΔP with pressure, calculated with ensemble A; plot d shows the same cross-correlation calculated with ensemble B. The numbers denote the gridpoint coordinates in the $X-$ and $Y-$ directions.*

ger than at an earlier time. This correlation structure is consistent with the correlation of log-perm with OR found by Chen & Oliver (2010) i.e. positive around the measurement well location and negative around other wells.
The correlation with ΔP (plots c&d) also seems slightly changed with respect to the one at an earlier stage (4.3). At a later stage, the negative correlations, albeit very small, extend to producers far away from the measurements (see producer with X=20, Y=11).

Figure 4.7 displays the cross correlation of seismic measurements with the water saturation field, in the same order as in figure 4.4. Plot a shows the correlation of ΔS with the water saturation. As in plot a of figure 4.4, the correlation is positive between the injector and the measurement gridpoint, negative on the opposite side of the injector, and zero elsewhere. The saturation fronts have reached the producers and appear as a straight line passing through them. These features can be explained by the image theory, first introduced by Ferris *et al.* (1962).
The image theory is based on the assumption that well drainage area have infinite areal extent. The effect of a geological impermeable barrier on the drawdown in the producing well is the same as if the aquifer had an infinite extent and a discharging image well was located across the boundary on a line normal to it and at the same distance from the boundary as the real producing well. The production rate of the imaginary well would be the same as the real one. On the other hand, the effect on drawdown in a production well due to another well operating at the same constraint is the same as the effect of a barrier boundary normal to the line connecting the wells.
The anisotropy in the permeability and therefore in the saturation fronts, stretches the correlations in the same direction as the permeability azimuth (plot b).
This correlation structure is consistent with the correlation of the saturation field with OR at producing wells in Chen & Oliver (2010), positive between the injector and the producing well at which the measurement is taken, negative on the opposite side of the injector; the non-zero cross-covariance region extends beyond the five-spot well pattern of the producing well, and each five-spot well pattern is separated from the adjacent ones by straight sharp lines.
Plot c presents the correlation of ΔP at the black diamond with the water saturation field. As in the previous two plots, the saturation fronts appear as sharp boundaries delimiting different five spot patterns. The correlation is negative in the area around the closest producer and it is also slightly negative in the areas between distant injectors and producers draining water flowing in the direction of the measurement location. The permeability an-

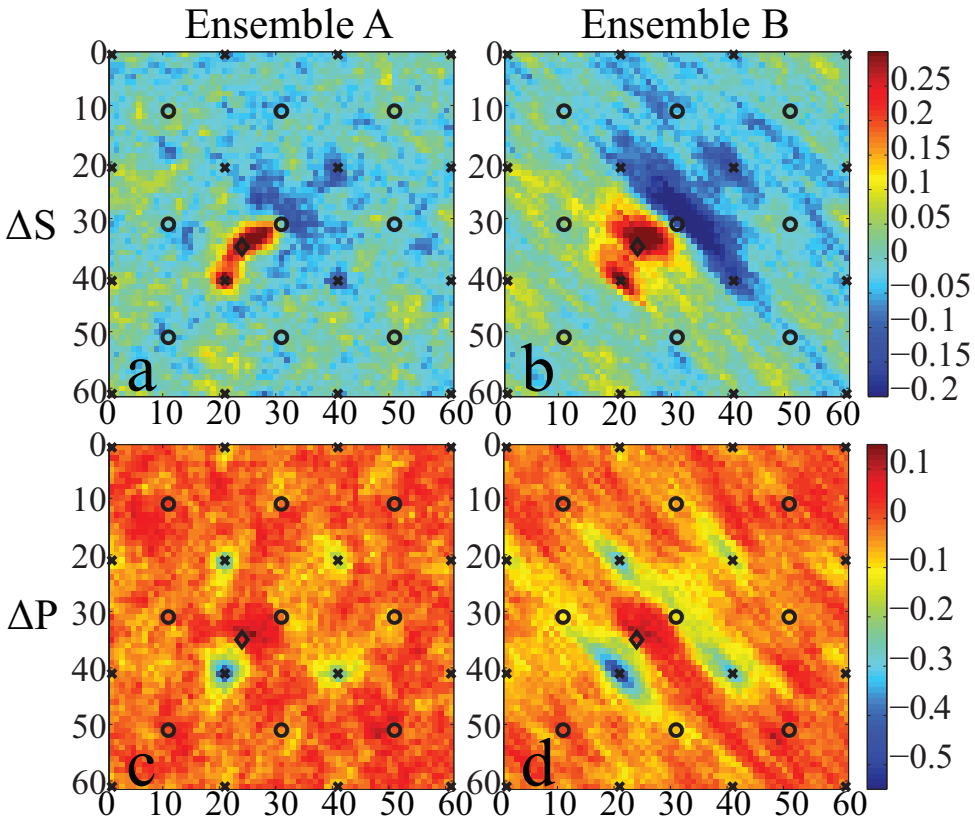

Figure 4.6: *Cross-correlation of the logarithm of permeability with seismic measurements at the location indicated by the black diamond. Plot a presents the cross-correlation of ΔS with log-perm, calculated with ensemble A; plot b shows the same cross-correlation calculated with ensemble B. Plot c presents the cross-correlation of ΔP with log-perm, calculated with ensemble A; plot d shows the same cross-correlation calculated with ensemble B. The numbers denote the gridpoint coordinates in the $X-$ and $Y-$ directions.*

isotropy does not change the correlation pattern (plot d).
The region of non-zero values extends much further than the five spot repeated pattern, through the entire model and sharp lines passing through the producers delimit different covariance regions corresponding to the each five-spots well groups.

Figure 4.8 presents the cross-correlation of seismic measurements with the pressure field, in the same order as in figure 4.5. The correlation of ΔS with the pressure, calculated with both of the ensembles (plots a&b), shows again non-zero values in an extended part of the model. The cross-correlation of ΔP with the pressure, like in plots c&d of figure 4.5 shows decreasing values with distance but nowhere in the model approaching zero. This correlation structure reflects the cross-covariances of the pressure field with production measurements as observed by Chen & Oliver (2010): There is no area in the model where the covariances of pressure with production measurements decreases to zero, neither at an early nor at a later stage.

4.2.4 Building the localization template

The real correlation of 4D seismic measurements with parameters and state variables has been observed through the previous plots. The knowledge of these real correlations during localization applied on the Kalman gain, allows the removal of spurious correlations without stripping the real ones. This way, the simulated ensemble-based covariance information can be fully exploited without being affected by noisy correlations or by filter divergence. From the presented plots some guidelines for building appropriate localization functions can be extracted.

localizing permeability

The analysis of the correlation of (log-)permeability with changes in saturation (figs. 4.3a & b & fig.4.6a & b) suggests that it would be appropriate to localize this covariance using a Furrer and Bengtsson type function centered around the measurement location and with a plateau (indicated by the red area, in which the function value is higher than 0.8) covering the whole five-spot well pattern to which the measurement belongs. This choice would be consistent with the localization function proposed by Chen & Oliver (2010) for the cross-covariance of permeability with well OR or WR: this function was centered around the producer and extended over an area slightly larger than the five-spot repeated pattern.
In order to localize the correlation of log-perm with changes in pressure(figs.4.3c &d & fig.4.6c&d) it would seem a safe choice to use a localization function

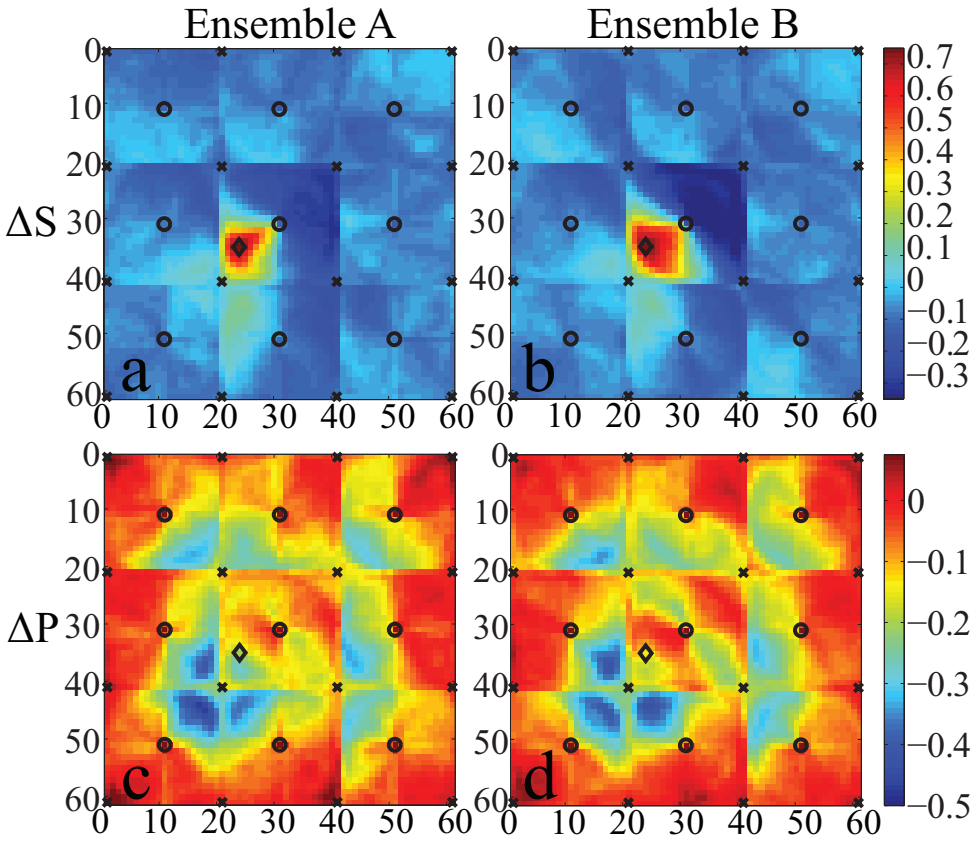

Figure 4.7: *Cross-correlation of the water saturation with seismic measurements at the location indicated by the black diamond. Plot a presents the cross-correlation of ΔS with water saturation calculated with ensemble A; plot b shows the same cross-correlation calculated with ensemble B. Plot c presents the cross-correlation of ΔP with satuation, calculated with ensemble A; plot d shows the same cross-correlation calculated with ensemble B. The numbers denote the gridpoint coordinates in the $X-$ and $Y-$ directions.*

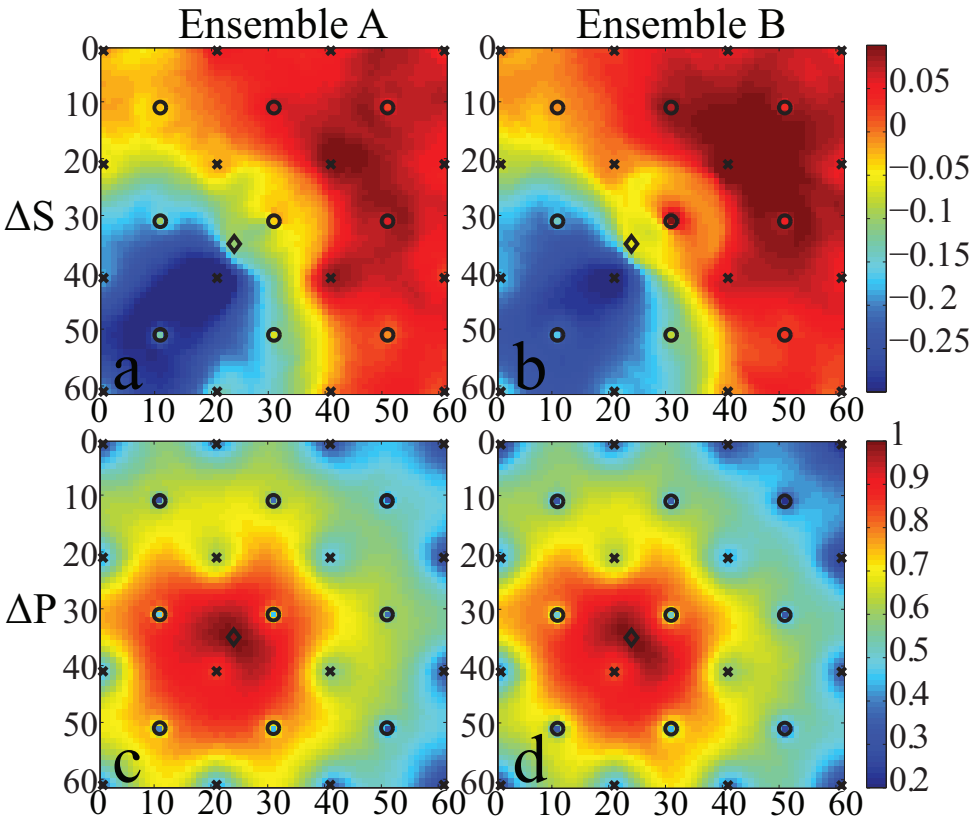

Figure 4.8: *Cross-correlation of the pressure field with seismic measurements at the location indicated by the black diamond. Plot a presents the cross-correlation of ΔS with pressure, calculated with ensemble A; plot b shows the same cross-correlation calculated with ensemble B. Plot c presents the cross-correlation of ΔP with pressure, calculated with ensemble A; plot d shows the same cross-correlation calculated with ensemble B. The numbers denote the gridpoint coordinates in the $X-$ and $Y-$ directions.*

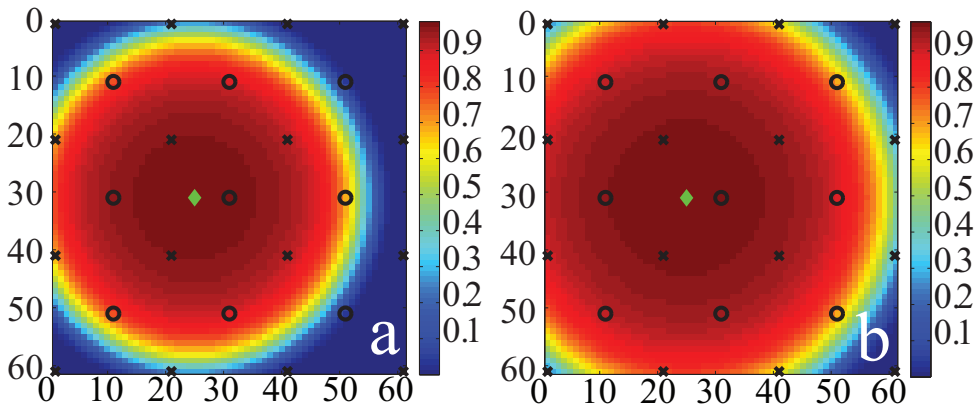

Figure 4.9: *Localization functions proposed for the cross-covariance of log-perm with ΔS (plot a) and with ΔP (plot b). The localizing functions are of Furrer type, centered around the measured point. In plot a the plateau covers the five-spot well pattern of the observation while in plot b the plateau extends up to the next lines of producers. The numbers denote the gridpoint coordinates in the $X-$ and $Y-$ directions.*

centered around the measurement location, with a plateau extending further than the five-spot well pattern, up to the next line of producers. This function would ensure that the negative small correlations as observed at distant wells after the water breakthrough (fig.4.6c&d) will be fully taken into account in the update.
Figure 4.9 illustrates the Furrer and Bengtsson type function proposed to localize the covariance of log-perm with ΔS (plot a) and with ΔP (plot b).

localizing saturation

The analysis of the correlation of saturation with changes in saturation (figs. 4.4a&b and 4.7a&b) suggests that an appropriate localization function must be centered around the measurement with a plateau extending beyond the five-spot well pattern to which the measurement belongs, up to the next line of producers. This function would be as large as required for the localization of the covariance of log-perm with changes in saturation.
More cumbersome appears to be the decision regarding the localization radius for the covariance of saturation with measured changes in pressure (figs. 4.4c&d and 4.7c&d), as it approaches zero only at very far distances. One option would of course be to apply no localization on this covariance. How-

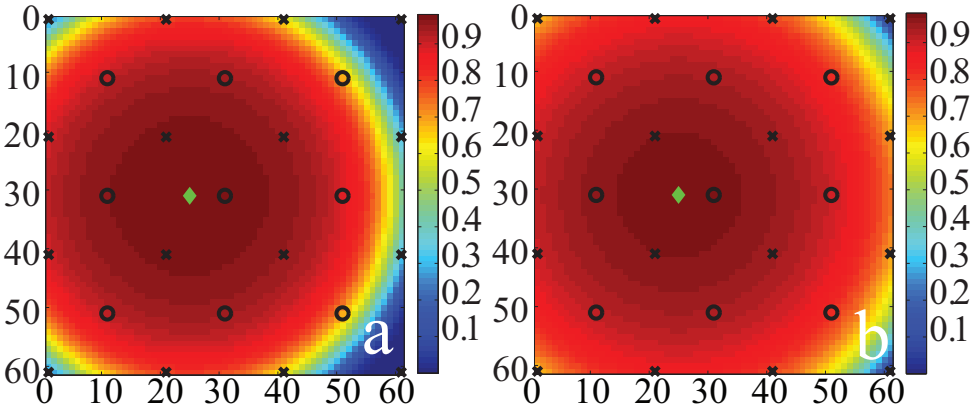

Figure 4.10: *Localization functions proposed for the cross-covariance of saturation with ΔS (plot a) and with ΔP (plot b). The localizing functions are of Furrer and Bengtsson type, centered around the measured point. In plot a the plateau reaches the first line of producers outside the five-spot well pattern in which the seismic measurement is taken, in plot b the plateau radius covers the whole five-spot well pattern of the observation while in plot b the plateau is equal to twice the diagonal of a single five-spot pattern. The numbers denote the gridpoint coordinates in the $X-$ and $Y-$ directions.*

ever, in order to increase the ensemble spread, we propose to use localization with a function centered around the measurement and with a plateau radius equal to twice the diagonal of a single five-spot pattern. Such a large localization function would ensure that far distant real correlations will still be taken into account.

"localizing" pressure

The plots showing the covariances of pressure with seismic measurements indicate that in no area of the model their values approach zero. Hence, it would seem appropriate not to localize pressure when using seismic observations. This choice is consistent with the findings by Chen & Oliver (2010) in which pressure was not localized in the case production measurements are available.
Figure 4.11 plots the localization functions suggested to use for pressure when changes in saturation (a) and changes in pressure (b) are used: in both cases the template size coincide with the entire model and the function is constantly equal to one. This is equivalent to not localizing the pressure state.

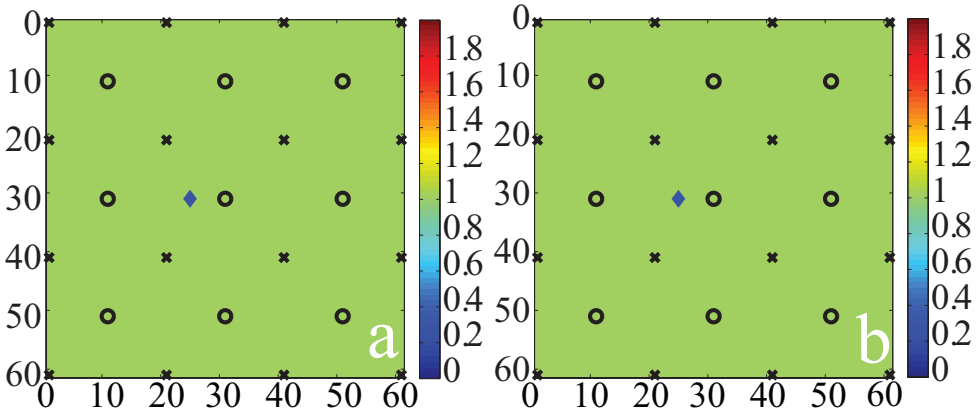

Figure 4.11: *Localization functions proposed for the cross-covariance of pressure with ΔS (plot a) and with ΔP (plot b). The localizing functions extend through the entire model and they are in both cases constantly equal to one. This is equivalent to not localize the state of pressure. The numbers denote the gridpoint coordinates in the $X-$ and $Y-$ directions.*

4.3 Applying the localization functions: Description of the model

4.3.1 Description of the model

In order to test the validity of the covariance study, a synthetic 2D model has been constructed.
The reservoir model has the same size as the models previously used, i.e. 61x61 gridblocks each with size of 33.3x33.3x10 m. The well configuration is also quite similar, except that the central five spot pattern of one injector and four producers has been replaced by a single producer penetrating the exact center of the model. This results in less production data allowing time-lapse seismic data to play a larger role in the updating process. The permeability distribution for the truth model is obtained using a sequential Gaussian simulation with an exponential variogram with major and minor correlation lengths of 3000 and 1000 m, respectively, with an azimuth of 45°W, and with a nugget effect equal to zero. The reservoir permeability ranges from 2 mD (no flow areas) up to 5000 mD with a mean value of 2500

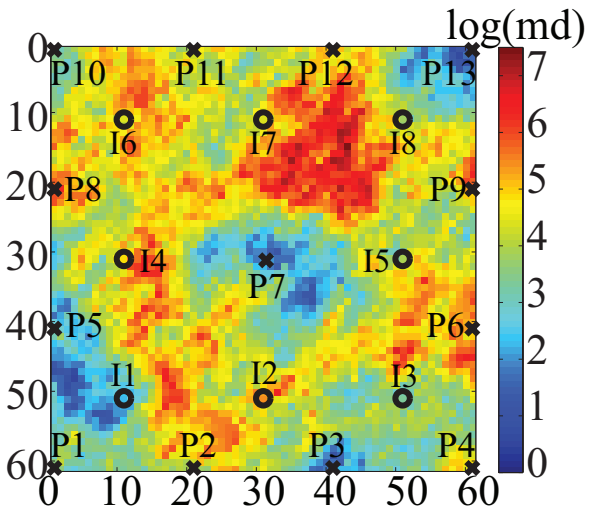

Figure 4.12: *(Logarithm of) permeability for the truth model. The black circles indicate the positions of the injectors and the black crosses of the producers. The axis labels denote the gridpoint index in the $X-$ and $Y-$ directions.*

mD. Secondary anisotropy has been introduced with a spherical variogram having azimuth of 45°E, major and minor correlation lengths of 1000 and 500m, respectively, and a nugget effect equal to zero. Figure 4.12 shows the true permeability field with the wells configuration on top; the general trend corresponds geologically to a coastal depositional environment: the elongated high permeability structures resemble tidal channels or tidal sand barriers, the low permeability areas are considered inter-channel or lagoon deposits. The reservoir porosity, similar to the models presented in the previous part of the chapter, has been set constant with a value of 0.3.

A total of 100 ensemble members was created, with permeabilities based on sequential Gaussian simulations with other variograms than used for the truth model. The aim is to keep the parameters search space sufficiently large in order to obtain a good fit to the observations. Table 4.1 reports the characteristics of the variograms for the ensemble members. Figure 4.13 illustrates the permeability distributions for five randomly picked ensemble members.

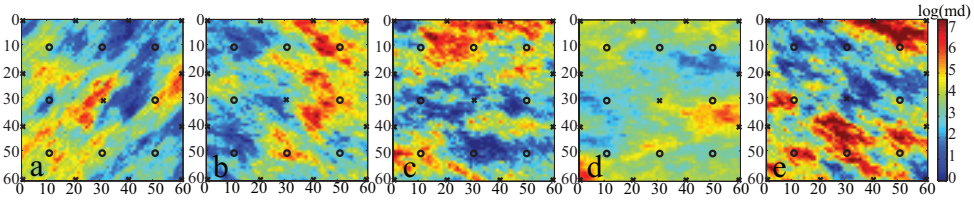

Figure 4.13: *(Logarithm of) permeability for five different ensemble members. Plot a refers to member 37, plot b to member 44, plot c to member 67, plot d to member 84, and plot e to member 96. The black rounds indicate the positions of the injectors and the black crosses of the producers. The axis labels denote the gridpoint index in the X− and Y− directions.*

Ensemble members	Primary Anisotropy					Secondary anisotropy				
	type of variogram	Azimuth	nugget effect	major corr. length	minor corr. length	type of variogram	Azimuth	nugget effect	major corr. length	minor corr. length
1-10	spherical	0◦	0	500	400	NA	NA	NA	NA	NA
11-20	exponential	45◦E	1	2000	500	exponential	0◦	1	1000	300
21-30	spherical	0◦	1	3000	500	exponential	45◦W	0.5	1000	500
31-40	spherical	45◦E	1	2000	1000	NA	NA	NA	NA	NA
41-50	spherical	45◦W	0	3000	1500	spherical	45◦E	2	300	150
51-60	spherical	isotropic	0	2000	1000	NA	NA	NA	NA	NA
61-70	exponential	90◦W	1	2000	1000	exponential	45◦W	0.8	800	400
71-80	exponential	0◦	1	6000	3000	NA	NA	NA	NA	NA
81-90	spherical	90◦W	0	2000	1000	NA	NA	NA	NA	NA
91-100	spherical	45◦W	1	2000	1500	spherical	0◦	1	1000	500

Table 4.1: *Variogram characteristics of the ensemble members.*

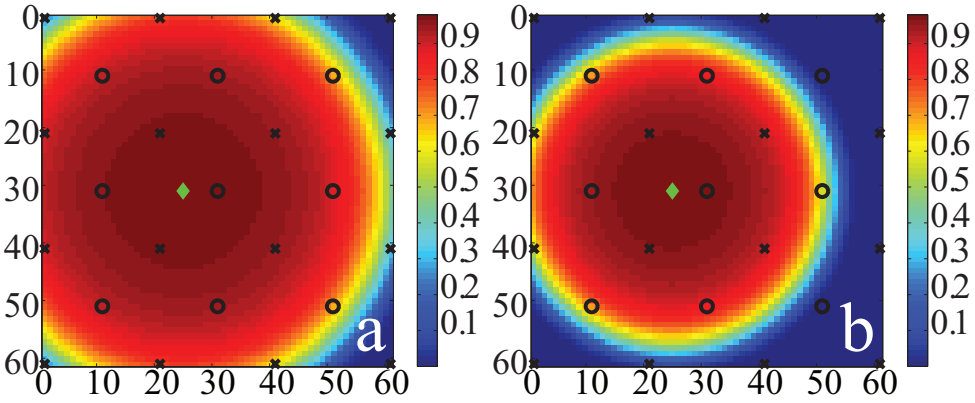

Figure 4.14: *Furrer tapering functions used to localize the cross-covariance of the (log-)permeability with changes in pressure. Plot a refers to the function used in case 4; note that this function is same as in fig. 4.9b which was suggested after analyzing the true covariance. Plot b refers to the function used in case 5, where the template radius, with respect to case 4, has been reduced by approximately 20%.*

4.3.2 History match and production forecast

With the ensemble introduced in section 4.3.1, five different simulations have been carried out. Case 1 corresponds to the run without any data assimilation performed (prior); case 2 refers to the run where only production data are assimilated, case 3 is the run where production data and seismic data are assimilated jointly; case 4 refers to the run where again both seismic and production data are assimilated but after applying covariance regularization. For the case of assimilating production data only the localization functions correspond to the ones suggested by Chen & Oliver (2010) while for seismic data, the localization functions are those recommended by the covariance analysis in the first part of this chapter. Case 5 is similar to case 4, except that the radius of every template used to localize cross-covariances of state and parameters with seismic measurements has been reduced by approximately 20%; in this way, the region of real correlation is not entirely included in the template size. Figure 4.14 plots the tapering functions used to localize the cross-covariance of permeability with changes in pressure in cases 4 and 5. Table 4.2 summarizes the characteristics of the cases.
The production data consist of Bottom Hole Pressures (BHP), water rates (WR), and oil rates (OR), with uncertainties estimated at 0.35 MPa (50 psi) for BHP, and 10% for water- and oil-rates.

Case 1	Case 2	Case 3	Case 4	Case 5
NO DATA Assimilation	Production Only	Prod. and Seismic	Pr. & Seis. Localized	Pr. & Seis. Local. Template Small

Table 4.2: *Characteristics of the different cases.*

Seismic observations consist of inverted time-lapse changes in saturation and pore pressure; given the large grid dimensions compared to the bin size, seismic measurements from different CMP's are averaged over the entire gridblocks, available for 1281 gridpoints. The standard deviation of the measurement error is 0.1 for changes in saturation and 1 MPa for changes in pressure. The baseline survey is shot at time 0 and the monitor surveys are repeated every 150 days. At time 0 the ensemble members have the same saturation and pressure fields as the truth case. In this situation, the information from time-lapse measurements can be used to update the model at the times of the monitor surveys, with no need to update state variables at earlier times. This legitimates a sequential assimilation of 4D seismic measurements with the EnKF, without the use of the EnKF smoother to update state variables back at time zero.
The simulations have been run for 1400 days, where the first 600 days are used to obtain a history match. As often observed in literature (Chen & Oliver, 2010; Emerick & Reynolds, 2010; de Wit & van Diepen, 2007) after matching history data the updated ensemble can be reinitialized. The advantage of this approach was explained in section 3.5.1. Hence, at the end of history matching, the simulations have been re-run until time 1400 days.
Figure 4.15 presents the water rates for producer 9 (see fig. 4.12). The first row refers to the history matching period, the second row to the period after restarting the model; the columns refer to the different cases. In blue the ensemble members are plotted, in yellow the ensemble mean, in black the analyzed ensemble, in green the mean of the update and in red the observations. Note how in the history match of cases 2,3,4,5 all the lines coincide. The truth model registers a late water breakthrough at about 1300 days. The prior shows a noticeable ensemble spread and an early water breakthrough time (plots a&f). The assimilation of data results in all cases in a better match than in case 1, as no water breakthrough is seen in this period (plots b,c,d,e). With the assimilation of production data, the prediction of the water breakthrough is shifted to a later time but still far from the truth such that the ensemble spread does not cover the truth (plot g). With the assimilation of production and seismic data, the ensemble mean is shifted much

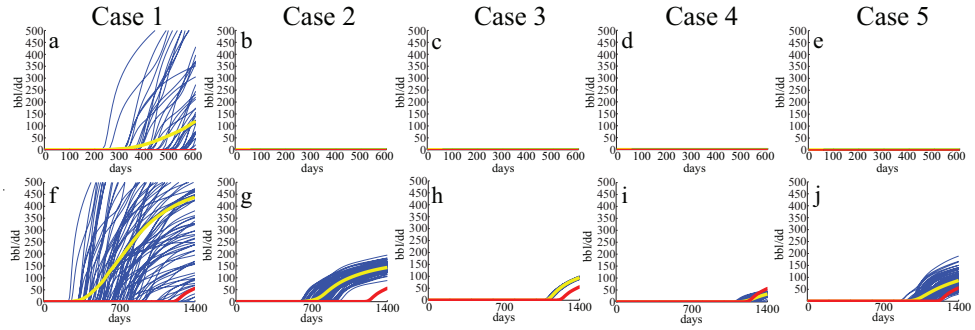

Figure 4.15: *Water rates for producer 9 for the different cases. The first row refers to the history matching period (600 days), the second row to the full period (1400 days) after restarting the model; the columns refers to the different cases. In blue are plotted the ensemble members, in yellow the ensemble mean, and in red the observations.*

closer to the real water breakthrough time; however, because of an excessive spread reduction, the ensemble spread does still not include the observed data (plot h). In case a localization that takes into account the size of the real correlations is applied, the ensemble mean forecast almost overlaps with the truth and the spread nicely covers it (plot i). Using a smaller template for the assimilation of seismic data, although increasing the ensemble spread, seems to move the ensemble mean away from the measurements (plot j).
Figure 4.16 shows the history match and the forecast for the oil rates at producer 12 (see fig. 4.12) for the different cases, in the same order and with same legend as in the previous figure. As for the water rate, the oil rate shows a large ensemble spread (plots a&f). The assimilation of production data is able to largely improve the history match (plot b), however, the oil production forecast is not really satisfying (plot g). When adding a large number of seismic observations to the production data, the history match becomes worse. This can be explained by the fact that the extreme reduction in the model covariance causes the update to be influenced by the model forecast only and not by the measurements: plot c presents a clear example of filter divergence. The malfunctioning of the filter results in a bad oil production forecast, as shown in plot h. The use of a correct localization criterion moves the update closer to the measurements (plot d) and leads to an almost perfect production forecast (plot i). If covariance regularization is performed with a smaller localization radius (plot e), this leads to an inferior model update with respect to the previous case, although the ensemble spread increases. Probably this is the effect of loosing some of the true correlations in the loc-

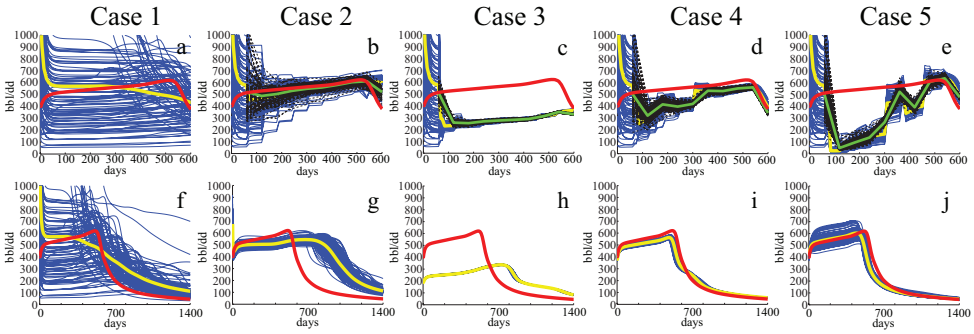

Figure 4.16: *Water rates for producer 9 for the different cases. The first row refers to the history matching period (600 days), the second row to the full period (1400 days) after restarting the model; the columns refers to the different cases. In blue are plotted the ensemble members, in yellow the ensemble mean, in black the analyzed ensemble, in green the mean of the update and in red the observations.*

alization process. Although the history match from case 5 is not as optimal as in case 4, the forecast is still satisfactory (plot j).
The observed figures show the improvement obtained through a correct use of localization only for two production measurements. A measure to estimate the performance for all the wells is the RMSE of production rates summed over all the producers. For a single well rate the RMSE is defined as the square root of the squared sum of the differences between the true and the mean of the ensemble rates at different time steps; summing over all the producers the total RMSE in water rates reads as:

$$RMSE_{WR} = \sum_{j=1}^{N_{Prod}} \left(\sqrt{\frac{1}{N_{TimeSteps}} \sum_{i=1}^{N_{TimeSteps}} \left(WR_i^{True} - WR_i^{Ens} \right)^2} \right), \quad (4.1)$$

where N_{Prod} denotes the total number of producers, and $N_{TimeSteps}$ the total number of timesteps at which the rates are sampled during the rerun period (0-1400 days). Analogously, the RMSE can be calculated for oil rates. Table 4.3 reports the RMSE for the water- and oil-rates in barrel per day (bbl/dd) for the different cases. It is worth noticing that the best performance is provided by the case where a correct localization is applied; the use of localization functions neglecting part of the real correlations increases the RMSE leading to a performance comparable to that of the cases where seismic information lacks or where seismic data cause filter divergence.
Figure 4.17 presents the true (log-)permeability field (plot a) versus the ensemble mean (log-)permeability estimated for the different cases at the end

	Case 1	Case 2	Case 3	Case 4	Case 5
RMSE (WR)	2707.8	593.7	544.7	303.9	677.9
RMSE (OR)	3239.2	875.9	808.7	434.7	736.3

Table 4.3: *RMSE for water- and oil-rates for the different cases in bbl/dd.*

Case 1	Case 2	Case 3	Case 4	Case 5
1.23	0.95	1.05	0.1	0.93

Table 4.4: *RMSE for the (log-)permeability estimate reported from the different cases at the end of the history match. These errors are calculated in log(mD).*

of the history matching period (i.e. 600 days). While the prior does not show any relevant structure (plot b), already with the assimilation of production data only the main permeability trend is recovered (plot c) quite well. The limited number of measurement however is reflected in a weaker update than obtained in the following cases including seismic measurements. With the assimilation of both seismic and production data (plot d) the main permeability trend is recovered but with some extreme outliers, which may be an indication of filter divergence. With the use of a correct localization function (plot e), the permeability is much better estimated than in the previous case; reducing the localization template leads to a mean permeability field with the true trend recovered but again with extreme outliers in certain areas (plot f).
Table 4.4 summarizes the analysis of figure 4.17 by reporting the RMSE between the truth and the ensemble mean (log-)permeability for all the different cases. The best estimate is clearly provided by case 4; It is worth noticing, that, including seismic data without localization results generally in an overall worse estimate than the one obtained by using production data only because of filter divergence.
Figure 4.18 shows the standard deviations of the log-perm calculated over all the reservoir gridblocks. The prior (plot a) presents, obviously, the highest standard deviation; case 2 has a reduced standard deviation, especially for gridpoints in correspondence with the wells. In case 3 (plot c) the standard deviation is overall unrealistically reduced, an indication of filter divergence. In case 4 (plot d) the ensemble covariance is slightly higher than in the previous case, necessary to ensure a better functioning of the filter; in case 5 (plot e), the standard deviation is overall higher than in the previous case.
Table 4.5 reports the standard deviation in the (log-)permeability for all the model gridpoints for all different cases. From the analysis of this table and of the previous figures, it can be argued that when using localization (case

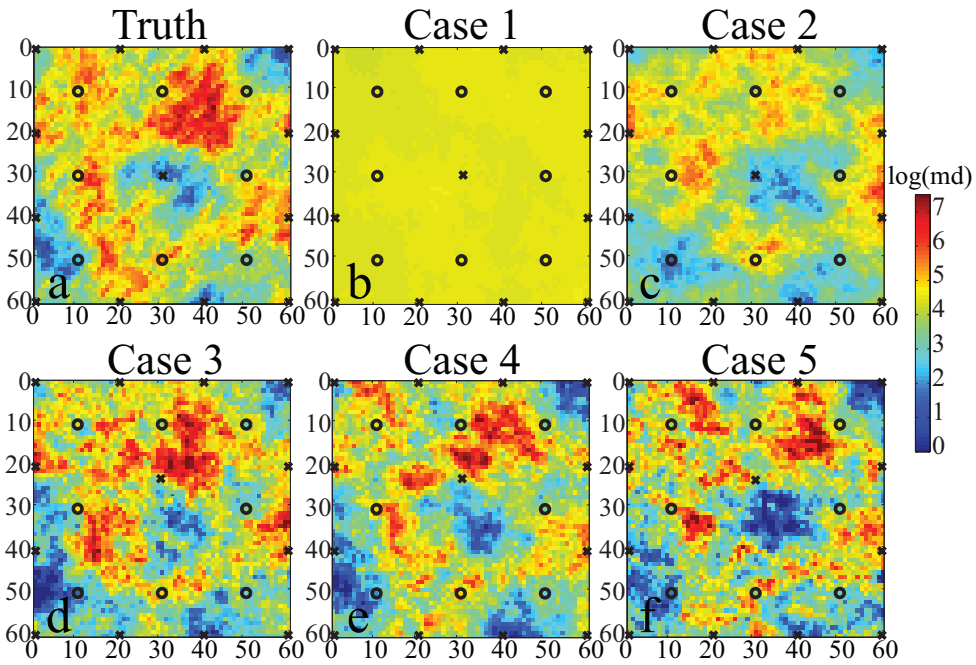

Figure 4.17: *Permeability estimates from the different cases at the end of the history match. The axis labels denote the gridpoint index in the $X-$ and $Y-$ directions.*

4 vs. case 5), a larger ensemble spread does not necessarily correspond to a better update.

4.4 Conclusions

This chapter presents an analysis of the covariance of model state and parameter variables with time-lapse seismic measurements provided by the inversion scheme in the chapter 2. The goal is to understand the extension of the non-zero real covariance regions. Knowing the real covariances, localiz-

Case 1	Case 2	Case 3	Case 4	Case 5
0.98	0.58	0.07	0.18	0.27

Table 4.5: *Average standard deviation of the ensemble permeability from the different cases at the end of the history match. The standard deviations are expressed in log(mD).*

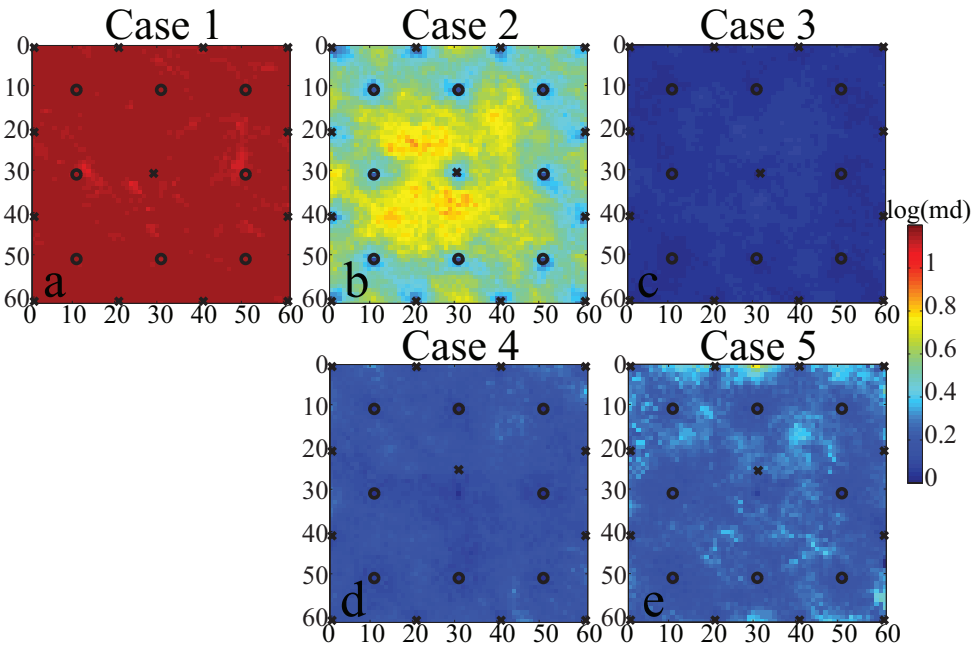

Figure 4.18: *Standard deviation for the reservoir gridblock permeability at the end of the history match for the different cases. The axis labels denote the gridpoint index in the $X-$ and $Y-$ directions.*

ation functions can be constructed to regularize the ensemble Kalman gain. The results demonstrated that the covariances between time-lapse seismic measurements and parameters/states depend on the geological permeability structure of the ensemble realizations, the flow dynamics (associated with the well pattern), and the production stage (or time).
The second part of the chapter is dedicated to a new approach for the assimilation of 4D seismic measurements with the EnKF. The traditional approach, using production data with or without seismic information, is compared with two updates obtained after localization; in the first case the localization functions are designed to include the a priori knowledge of the true correlations between model variables and observations, while in the second example the template used to regularize the covariance with seismic measurements is chosen smaller; this is done to mimic a realistic case in which the true covariance is not necessarily known and can lead easily to a wrong choice of the template.
Results from a 2D synthetic model show that with the assimilation of produc-

tion data only the permeability trend is not fully recovered. Adding seismic data causes an excessive ensemble covariance contraction with a detrimental outcome (filter divergence); in fact, in this case in the history match of production data the update moves away from the truth, the production forecast is poor and and the permeability estimate presents extreme values. The use of covariance localization to include only the real correlations improves the update considerably: the filter divergence is avoided allowing the analyzed ensemble to move closer to the observed rates, the permeability field is correctly estimated, and as a consequence, the reservoir forecasts fully reflect the true behavior. The use of a tapering localizing function smoothly decreasing with distance avoids the introduction of sharp boundaries in the analysis; this helps in obtaining consistent ensemble updates.
It might occur that when the real correlations are not known, the template used for the Kalman gain covariance regularization is too small to include them all. If this is the case, the increase in ensemble spread, which is necessary to avoid filter divergence, is even more pronounced than in the case of a larger, more appropriate template; however, a more evident increase in the effective ensemble size is not necessarily accompanied by an improvement in the update. In fact, cutting out some real correlations through localization results in an inferior quality production history match and in a lower accuracy of the permeability estimate.
In the next chapter, a similar study will be performed on a more realistic 3D field where the traditional EnKF update, with production data only or including seismic data, is compared to the localized update; in this latter case, the localization functions for the cross-covariance regularization in the Kalman gain are based on the conclusions from the covariance analysis presented in this chapter.

Chapter 5

3D Results

This chapter presents a comparison between a traditional history match based on an EnKF approach versus a localized version applied to a large 3D reservoir model. The aim is to verify the effect of covariance regularization on the assimilation of seismic data in a synthetic, though realistic case. Seismic data are assimilated either as vertically averaged observations (as proposed in the inversion from chapter 2) or, assuming higher seismic vertical resolution, as observations assigned to single reservoir gridblocks. The localization regions for the covariances regularization in the Kalman gain have been selected following the rules-of-thumb determined in the previous chapters based on smaller 2D models with a regular well pattern. Results show that, with the use of localization, an improvement in the match and in the prediction of production data is achieved, as well as a moderate improvement in the overall permeability estimate.

5.1 Introduction

This chapter, showing the effect of localization in an EnKF approach for history matching applied to a full 3D synthetic reservoir, starts with a description of the 3D model (section 5.2). Subsequently, results of different EnKF updates with and without localization are compared (section 5.3). Section 5.4 provides a broader discussion on this case study and finally, section 5.5 lists conclusions and recommendations for future work.

5.2 Model description

The truth model used in this study is the same as presented in chapter 2 consisting of an anticlinal structure with a fault cutting through the reservoir.

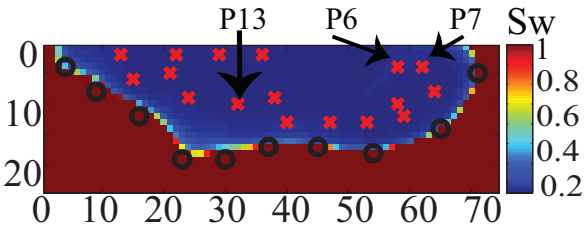

Figure 5.1: *Initial saturation for layer 5. The injectors, indicated with black circles, are located at the OWC, while the producers, indicated with red crosses, penetrate the higher part of the model. The numbers denote the gridpoint indexes in the X− and Y− directions. The producers indicated by arrows were chosen to display production profiles in later figures.*

The reservoir thickness is about 30 m and the reservoir rock is "trapped" in between impermeable shale layers. The positions for all the injectors and the remaining producers were kept identical. Water is injected near the OWC. Since there is no aquifer drive and the over- and the underburden have extremely low permeability, in- and outflow only occur at the wells. Figure 5.1 shows the original OWC for layer 5, and the well positions.
100 ensemble members were created, populated with porosities obtained through sequential Gaussian simulation without conditioning to well data. For all the realizations, the variogram used is the same as for the truth: long and short horizontal correlation lengths of 5000 and 500 m, respectively, and a vertical correlation length of 25 m. For 60 realizations the azimuth is the same as for the truth (80°W); 20 realizations have a variogram with an azimuth of 70°W, and for the remaining 20 realizations the azimuth is 90°W. The same poro-perm relationship (and the related uncertainty) as for the truth was used to derive the ensemble permeabilities, displayed in figure 5.2.

Figure 5.3a&b plot the porosity for layer 1 and 5 of ensemble member 50; below each plot the respective permeabilities are plotted (c&d). Note the resemblance between the porosities in the different layers resulting from the imposed vertical correlation.

5.3 History matching results

With the presented ensemble, six different simulations were run. Case 1 indicates the run without data assimilation (prior). Case 2 refers to the run in which only production data are assimilated. Cases 3 and 4 are the runs in

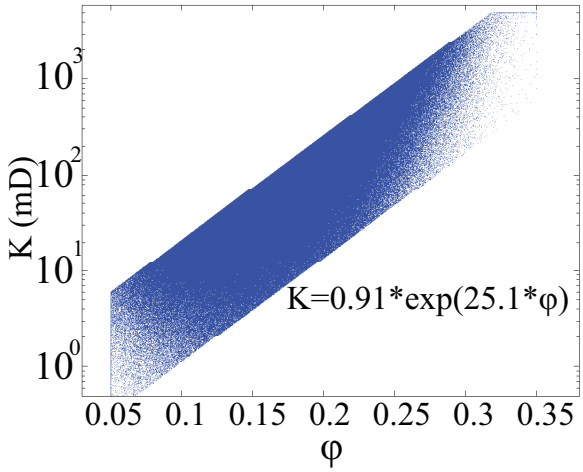

Figure 5.2: *Porosity-permeability relationship, in semi-logarithmic scale, used for the truth and for the ensemble members. The permeability is indicated in milliDarcys. The uncertainty in the relationship produces a cloud of point.*

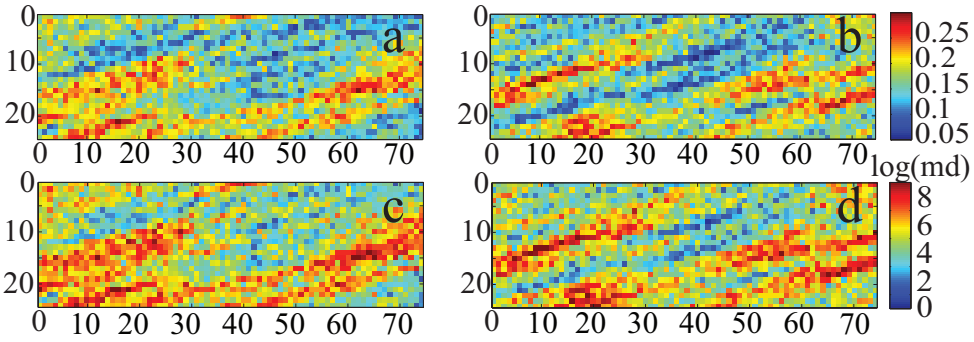

Figure 5.3: *Porosity for layer 1 (plot a) and layer 5 (plot b) of ensemble member 50. In the second line, permeability for layer 1 (plot c) and layer 5 (plot d) for the same ensemble member. The numbers indicate the gridblocks X- and Y-indexes.*

Case 1	Case 2	Case 3	Case 4	Case 5	Case 6
No Data Assimilation	Production Only	Prod. and Seismic (vertically averaged)	Prod. and Seismic (per gridblock)	Prod. and Seis. (vertically averaged) LOCAL	Prod. and Seis. (per gridblock) LOCAL

Table 5.1: *Characteristics of the different cases.*

which production data are assimilated together with seismic data: in the first case (3) seismic measurements are inverted to vertically averaged changes in saturation and pressure, and in the second case (4), those changes are inverted per gridblock. Case 5 and 6 refer to the runs in which production and seismic data are assimilated with covariance localization: in case 5 the seismic measurements are the same as in case 3, while in case 6 the seismic measurements are the same as in case 4. Table 5.1 summarizes the characteristics for the different cases.
This chapter investigates the possibility to extend the conclusions provided by the study of Chen & Oliver (2010) and by chapter 3 from a 2D model with a regular well pattern to the 3D model here introduced. Chen & Oliver (2010) suggest some rules-of-thumb to build localization functions for the covariances of states and parameters with production data:

- The localization functions to localize the cross-covariances of states and parameters with any kind of production measurements should be centered around the well location and include at least the closest producers and injectors;
- The template size to use for the localization of the covariance of log-perm with BHP should be smaller than the template size for the localization of the covariance of log-perm with OR or WR;
- The template sizes to use for the localization of saturation with BHP at one injector and with WR or OR have to be very large to include far distant producers;
- The cross-covariance of pressure with production data should not be localized.

Figure 5.4 plots the Furrer tapering functions, based on the listed rules-of-thumb, which will be used in this study for the localization of covariances of parameters and states with production measurements.
Analogously, the covariance study in chapter 3 of this Thesis, can provide some rules-of-thumb to build localization functions for the covariances of states and parameters with seismic data. The rules can be summarized as:

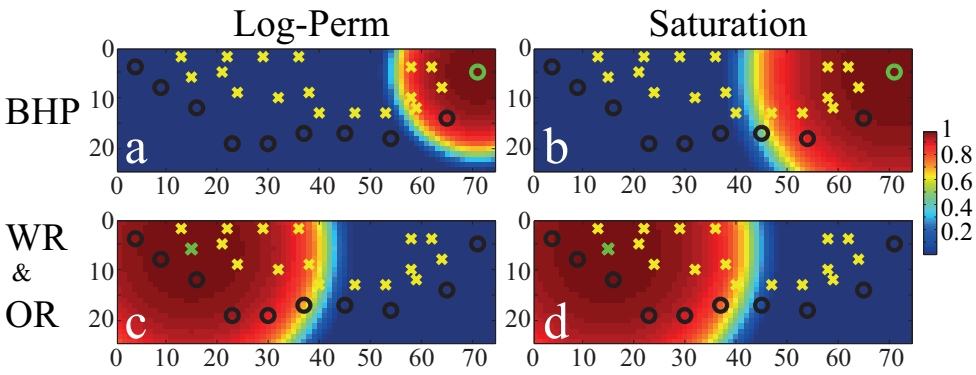

Figure 5.4: *Localization function used in the update of permeability and saturation with production measurements. The crosses indicate the position of the producers and the circles the injectors locations. The wells at which the measurements are taken are colored in green. The numbers indicate the gridblocks X- and Y-indexes.*

- The localization functions to localize the cross-covariances of states and parameters with any seismic measurements should be centered around the measured location and include at least the closest producers and injectors;
- The template size to use for the localization of log-permeability with changes in saturation should be smaller than the template size used to localize the cross-covariance of log-perm with changes in pressure;
- The extension of the non-zero region for the cross-covariance of saturation with ΔS is larger than the non-zero region of the covariance of log-perm with ΔS;
- The extension of the non-zero region for the cross-covariance of saturation with ΔS is smaller than the non-zero region for the cross-covariance of saturation with ΔP;
- The template size used for the localization of covariances of parameters or states with Oil-Rates is as big as the template size used to localize covariances of parameters and states with Water-Rates.
- The cross-covariance of pressure with seismic data should not be localized.

Figure 5.5 plots the resulting Furrer tapering functions used for the localization of covariances of parameters and states with seismic measurements.

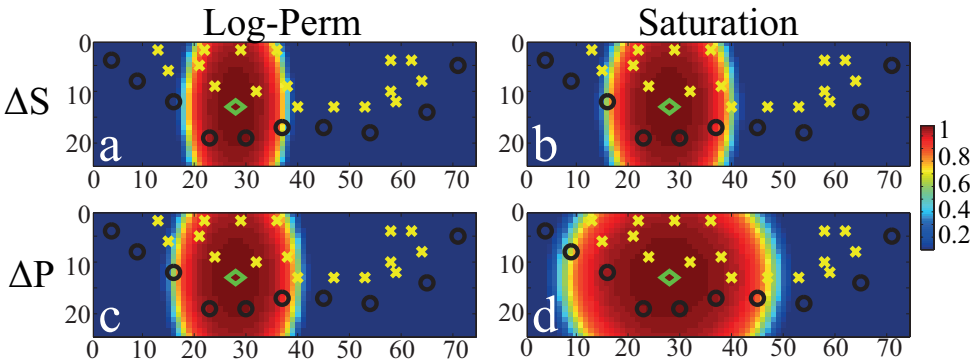

Figure 5.5: *Localization function used in the update of permeability and saturation with seismic measurements. The CMP at which the measurements are taken is indicated by a green diamond. The yellow crosses indicate the position of the producers and the black circles the injectors locations. The numbers indicate the gridblocks X- and Y-indexes.*

All the simulations were run for 30 years, with the first 11 years (4000 days) corresponding to a history match and the remaining period of 19 years to a forecast. Production data consist of Bottom Hole Pressures (BHP), water rates (WR), and oil rates (OR), with uncertainties of 0.35 MPa (50 psi) for BHP, and 10% for rates. These data are collected every 16 months (500 days).
Seismic surveys are acquired every 1000 days starting from time 0 (at this time, similar to the 2D case described in chapter 4, the truth and the ensemble members have the same pressure and saturation). Seismic observations consist of inverted time-lapse changes in saturation and pore pressure; given the large grid dimensions compared to the bin size, seismic measurements from different CMP's are averaged over the entire gridblocks. Seismic measurements are available at 592 CMP's distributed over 8 Inlines and 74 CrossLines. This means that in cases 3 and 5, at each monitor survey, the changes in saturation and in pressure to assimilate are 592, while in cases 4 and 6 those are 4144 (592*7). The standard deviation of the measurement error is 0.1 for changes in saturation and 1 MPa for changes in pressure, identical for all cases.
The next figures present the history match and the forecast from the different cases for water and oil rates for three different wells. These are producers 7, 13, and 6, ordered according to the distance from the initial OWC and therefore, to the true water breakthrough time (see figure 5.1). Producer 7 registers a waterphase arrival late in the history matching period; producer

13 records a water breakthrough time at the very end of the history match, while producer 6 only sees water arriving long after the history matching period ends. In each graph, the ensemble members forecast is plotted in blue, the ensemble mean in yellow, the ensemble update in black and the update mean in green; the observations are plotted in red. Every figure contains six graphs, each one referred to with a letter; the plots' alphabetical order corresponds to the numerical order of the different cases.
Figure 5.6 shows the water rates from producer 7. Case 1 (plot a) presents a large ensemble spread; the assimilation of production data (b) results in a poor match in the late history matching period. A possible explanation is that the use of production measurements only is enough to start filter divergence; therefore, localization might be required also for this case (see next chapter). The consequence of a poor match is an underestimation of the true water rate and a later estimation of the water breakthrough time. By introducing seismic data, either vertically averaged (plot c) or assigned at single gridblocks (plot d) the match and the forecast improve: As seen in Fahimuddin *et al.* (2011), even in case the ensemble covariance contraction associated to seismic data induces or exacerbates filter divergence, the use of seismic data might still constrain better the matching solution than using only production data. However, the larger the number of observations the stronger the divergence from the observations, resulting in a poorer match and forecast (compare plot c with d). By applying localization in the assimilation of seismic data, either vertically averaged (e) or defined per gridblock (f), the match and the prediction largely improve.
Figure 5.7 illustrates the water rate for producer 13. Again, the prior presents a large spread and a mean far away from the truth behavior; case 2 presents a very poor estimate of the water breakthrough time (a), which is only slightly improved if vertically averaged seismic data are assimilated (c); however, the larger number of seismic observations increases the bias from the truth behavior (d). The use of localization on vertically average seismic data partially improves the water breakthrough time estimate (compare e with c). In case 6, where localization is applied on the higher resolution inverted seismic data, the water breakthrough time estimate clearly improves; still, the production estimate is not fully consistent with the truth.
Figure 5.8 presents the water rate for producer 6, which registers a late water breakthrough time (≈8000 days). For this well, the assimilation of production data only (b), or with seismic data (c&d) results in an estimate of the water-phase arrival time much later than the truth. The introduction of localization on seismic vertically averaged data provides a perfect estimate of this time; the localization on higher resolution inverted seismic observations

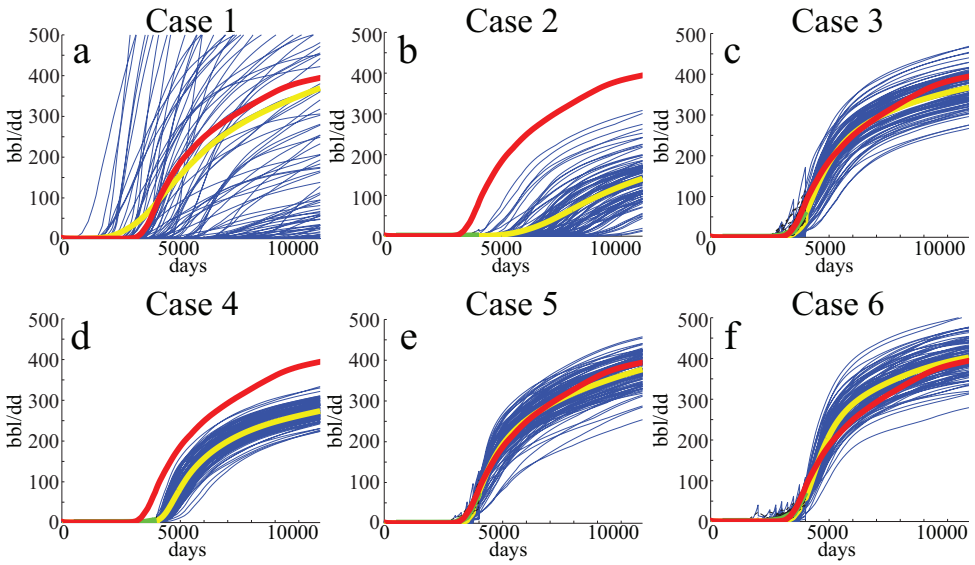

Figure 5.6: *Water rates from producer 7 obtained with the different cases. The ensemble members forecast is plotted in blue, the ensemble mean in yellow, the ensemble update in black and in green the update mean; the observations are plotted in red.*

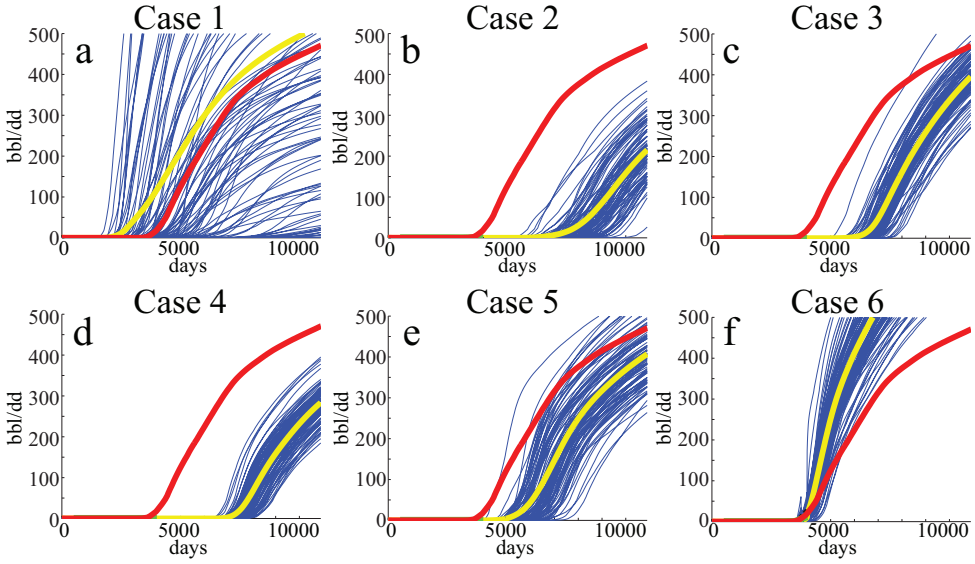

Figure 5.7: *Water rates from producer 13 obtained with the different cases. The ensemble members forecast is plotted in blue, the ensemble mean in yellow, the ensemble update in black and in green the update mean; the observations are plotted in red.*

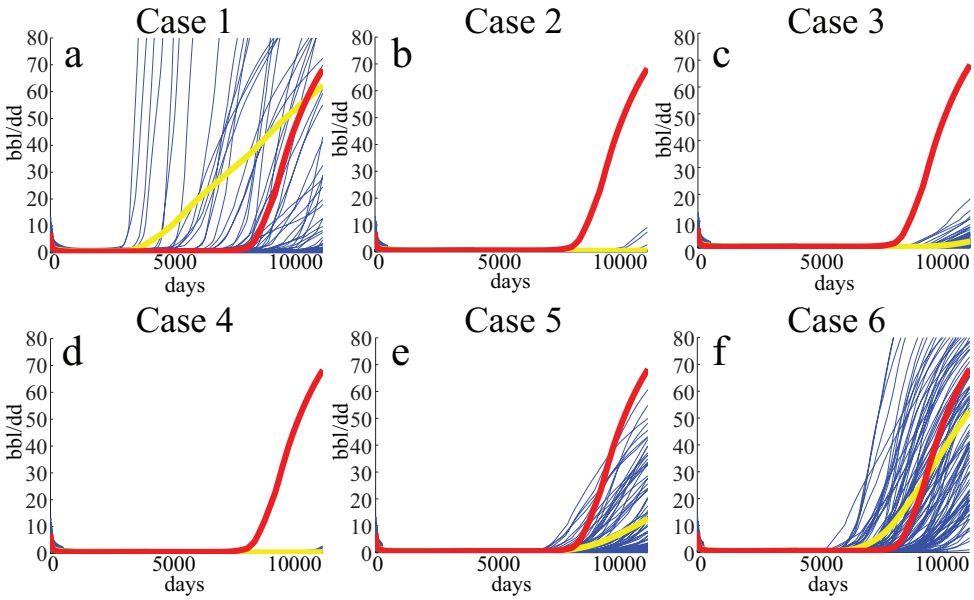

Figure 5.8: *Water rates from producer 6 obtained with the different cases. The ensemble members forecast is plotted in blue, the ensemble mean in yellow; the update coincide with the truth and it is not visible. The observations are plotted in red.*

(f), with respect to the traditional update (d), improves considerably the water breakthrough time estimate and the mean ensemble production forecast. However, despite the improvements introduced by localization, in no cases the ensemble production forecast reproduces the truth behavior.

Table 5.2 reports the average error (in days), from the different cases, in the water breakthrough time estimate for the producing wells; the producers are divided into two groups: one group with early water breakthrough time (¡4000 days) and another group with later water breakthrough time (¿=4000 days). The use of production data only and of production and seismic data without localization, with respect to the prior case, increases the average error in both the groups; the introduction of covariance localization largely improves the water breakthrough time estimate, especially for well with a later water breakthrough.

The next three figures show the oil rates for the same wells. Figure 5.9 refers to producer 7. Like the truth, all the ensemble members show a decreasing production with time, resulting in a prior estimate that is not far from the real behavior (plot a); this consideration holds for all the producers. Case 2 (b) shows a bad history match and a production forecast worse than the prior, confirming that already with production data filter divergence might

	Case 1	Case 2	Case 3	Case 4	Case 5	Case 6
Early Group	506.4	718.5	767.9	875.6	645.6	676.1
Late Group	2492.1	2206.6	2213.1	2218.2	1564.8	1308.2

Table 5.2: *Average error (from the different cases) of the water breakthrough time estimates from the producers. The average errors are reported in days and the producers are divided into two groups: one group with early water breakthrough time (¡4000 days) and another group with later water breakthrough time (¿4000 days).*

occur. As seen in figure 5.6, with the introduction of vertically averaged seismic data (plot c), even if the ensemble spread decreases, both the quality of the match and of the forecast improve. However, if the number of available seismic observations becomes too large, the filter divergence becomes more evident and the quality of the match and of the production forecast decrease (plot d). Using localization on both types of seismic data results in ensemble mean forecasts overlapping with the truth (e&f).
Figure 5.10 plots the oil rates for producer 13. The prior shows a large ensemble spread but a relatively good mean (a). In the history matching period,

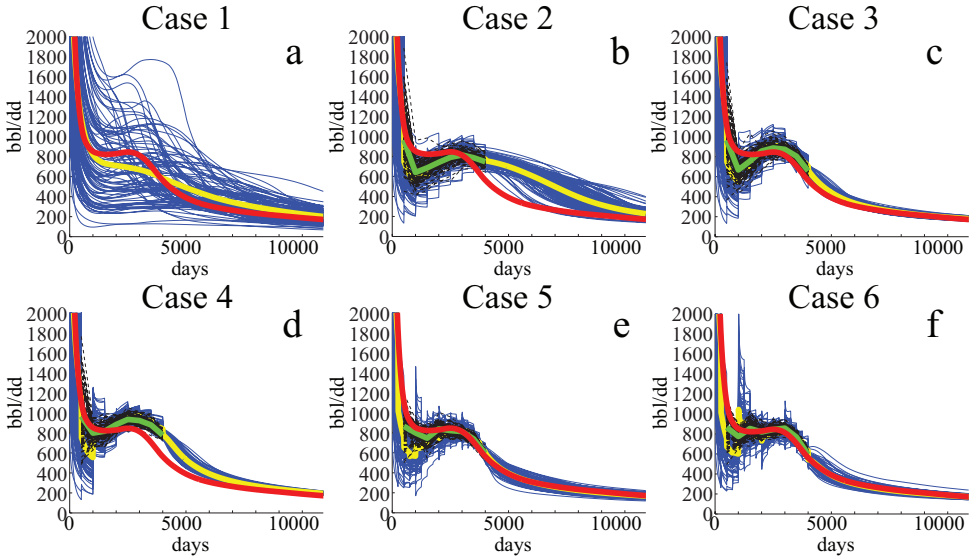

Figure 5.9: *Oil rates from producer 7 obtained with the different cases. The ensemble members forecast is plotted in blue, the ensemble mean in yellow, the ensemble update in black and in green the update mean; the observations are plotted in red.*

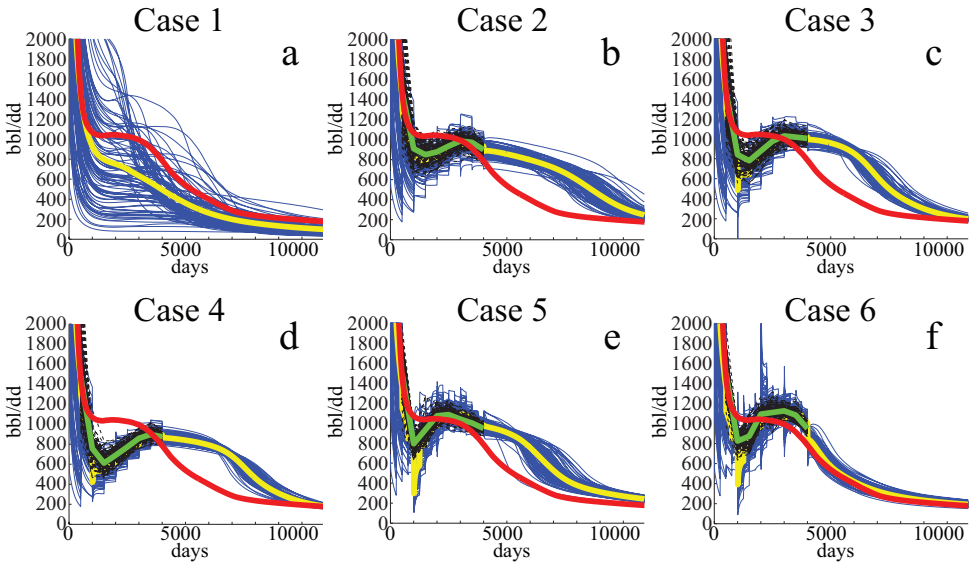

Figure 5.10: *Oil rates from producer 13 obtained with the different cases. The ensemble members forecast is plotted in blue, the ensemble mean in yellow, the ensemble update in black and in green the update mean; the observations are plotted in red.*

the assimilation of production data (plot b) results in a divergence from the truth; this divergence becomes even larger if the number of measurements to assimilate increases: going from case 1 to case 3 the divergence becomes progressively more pronounced (plots b to d), leading to poor forecasts. The use of covariance regularization results in a match improved if compared to the respective traditional approach (compare plot e with c and f with d); however, case 6, probably because of more detailed information on reservoir states given by a higher resolution in seismic data, provides a much better forecast than case 5.

Figure 5.11 shows the oil rate for producer 6. As for the previous figures, the prior mean is not far from the truth, although there is certainly room for improvement (plot a). Case 2 (plot b) presents already a slight divergence of the update from the truth, which is exacerbated by the use of seismic data (plot c&d): as observed in the previous figure, the divergence is proportional to the number of measurements, becoming more evident going from case 3 to 4. The consequence is an incorrect forecast. The localization of production and seismic data (plots e&f) leads to an increase in the ensemble spread improving both the match and prediction.

As in the previous chapter, the RMSE averaged over all the producing wells

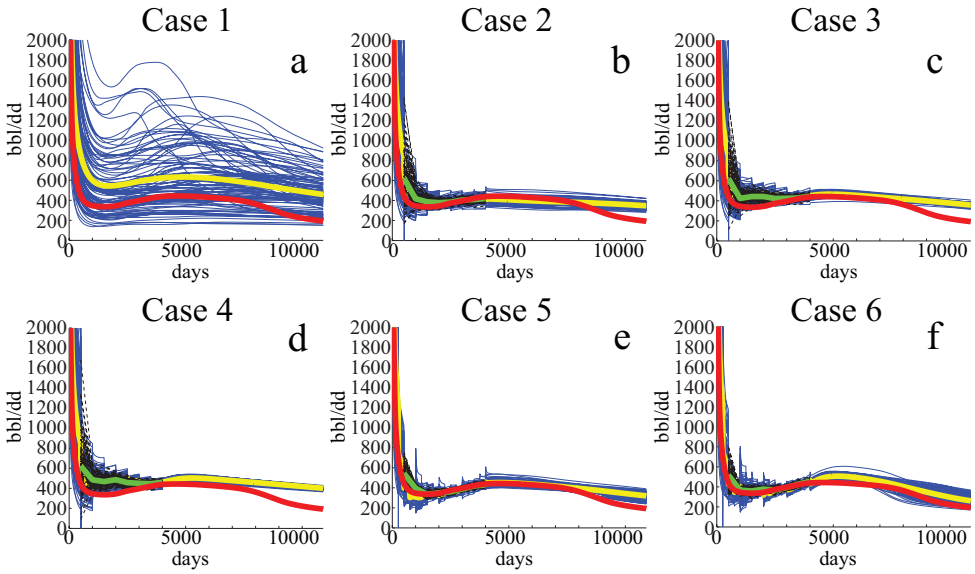

Figure 5.11: *Oil rates from producer 6 obtained with the different cases. The ensemble members forecast is plotted in blue, the ensemble mean in yellow, the ensemble update in black and in green the update mean; the observations are plotted in red.*

Case 1	Case 2	Case 3	Case 4	Case 5	Case 6
609.7	672.5	673.1	674.9	665.8	663.3

Table 5.3: *RMSE error in the oil production averaged over all the producers. The error is calculated over the whole time of the simulations and it expressed is in days.*

might be used to evaluate the performance of the different cases in matching the truth oil production. This error is defined as in equation 4.1. Table 5.3 reports the RMSE averaged over all the producers from the different cases; the rates are sampled at various timesteps from time 0 to time 30 years and it is expressed in days. In general the use of only production data or production and and non-localized seismic data leads to large errors; the error decreases with the use of localization, but still higher than in the prior case.
Figure 5.12 shows the true and the ensemble mean permeability at layer 1 and 3 for the different cases at the end of the history match period; for each case, two plots are presented, the upper one referring to layer 1 and lower one to layer 3. Plots a&b present the truth permeability; in the prior (c&d) no structure is present. With the assimilation of production data the

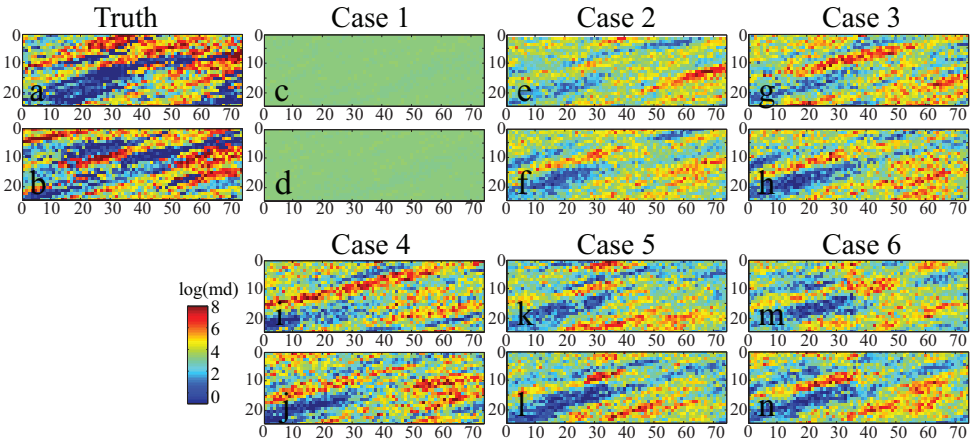

Figure 5.12: *True and estimated permeability from the different cases for layers 1 and 3. For each case two plots are presented, the upper one referring to layer 1 and lower one to layer 3. The numbers denote the gridpoint indexes in the $X-$ and $Y-$ directions.*

predominant permeability trend is recovered although the more extreme permeability values are not captured. Case 3 to 6 (plots g&h to m&n) present a similar permeability estimate as case 2, although the extreme values are better recovered than in the case where only production data are used. The localization of vertically averaged seismic data (k&l), with respect to case 3, seems to better define the permeability field in the central part of the layer 3, where there is a dense succession of thin high/low permeability structures (see area between gridpoints with X-index 20 and 50, in the upper part of the plot). The estimate from case 6 (plots m&n), with respect to that from case 4 (plots i&j) seems to contain less extreme values; furthermore, the estimate from case 4 is not overall correct (for example, in layer 1, the high permeability streak beginning at gridpoint with X-index 15 extending towards NE is prolonged towards SW up to the model edge); the use of covariance regularization seems to improve the permeability estimate at least in those areas. Although cases 2 to 6 all recover the general trend from the truth case, in no case a fully satisfactory match with the reference case can be observed.
Figure 5.13 plots the histograms of the mean (log-)permeability updated at the end of the history match period from the different cases. The true spectrum covers a quite broad range of permeability values and a distribution not perfectly Gaussian. The prior mean presents a very narrow spectrum, while all the other estimates presents a perfectly Gaussian spectrum, much broader than the prior. This translates into a more heterogeneous permeabil-

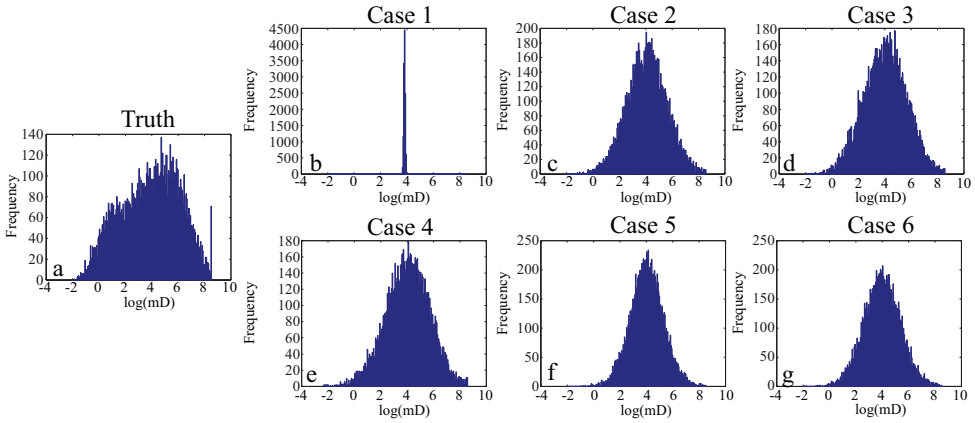

Figure 5.13: *True and estimated (log-)permeability histograms from the different cases. The truth has a broad spectrum and an overall distribution not perfectly Gaussian; The prior has a very narrow spectrum, while all the other cases present a completely Gaussian, broader spectrum which can better reproduce the truth flow pattern.*

Case 1	Case 2	Case 3	Case 4	Case 5	Case 6
2.421	2.677	2.665	2.664	2.422	2.412

Table 5.4: *RMSE error in the (log-)perm at the end of the history match period for the different cases.*

ity structure (as observed in figure 5.12), more able to capture the true flow; however, no case presents a broad spectrum as the truth.
Table 5.4 lists the RMSE for the mean (log-)permeability estimates from the different cases at the end of the history match period; the error is expressed in log(mD). Case 2,3 and 4 present comparable RMSE, higher than the prior; the error is lowered if localization on seismic and production data is used (cases 5 and 6). The use of localization results in an error similar to the prior but not smaller, even though, as seen from the previous figure, its spectrum is extremely narrow compared to the truth one.

5.4 Discussion

From the presented results it appears clear that the introduction of a large number of seismic observations (like in cases 2,3, and 4) is likely to cause an excessive ensemble covariance contraction and therefore, filter divergence.

In case the seismic resolution is lower and seismic can only provide vertically averaged observations, the reduction in the ensemble is not so extreme; hence, defining case 3 as a representative example of filter divergence appears dubious. Despite this, in this chapter a covariance localization applied on the assimilation of vertically averaged seismic data has been included; the motivation is, apart from increasing the effective ensemble size, to evaluate the effect of Kalman gain regularization in cases averaged measurements are provided. This procedure, although common in reality, is not sufficiently documented in literature (Leeuwenburgh *et al.*, 2011); therefore, it requires more investigation.

5.5 Conclusions and recommendations

This chapter shows an example of assimilation of time-lapse changes in saturation and in pressure with the EnKF from a synthetic, realistic 3D model. Different simulations were compared. Results indicate that the assimilation of production data only might be sufficient to cause filter divergence; as a consequence, if localization is not applied, the match and the prediction of well data might be poor, as well as the final estimate of the permeability field. The introduction of seismic data, either vertically averaged or with the resolution equal to the model gridblocks thickness, may exacerbate the process of filter divergence, degrading the match for some wells and the overall permeability estimate.
Kalman gain regularization through covariance localization has been applied for the assimilation of production and seismic data in order to avoid the filter divergence and improve the match with well data. The used localization functions are of Furrer type, aiming at smooth updates. The localization radii for the different covariances have been chosen according to some rules-of-thumbs obtained by previous covariance studies; those studies investigated the extension of the non-zero cross-covariance region of state and parameters variables with production and seismic measurements, and these were conducted on smaller 2D models with a regular well pattern (five-spot repeated).
The introduction of covariance localization avoids filter divergence, improving the match with well data; results indicate also an improvement in the estimate of the water breakthrough time especially for wells distant from the original OWC, that is with a late water breakthrough time. With the use of localization also the permeability estimate slightly improves, even though in none of the cases a fully accurate estimate is obtained, or at least the improvement is not as clear as in the 2D case (chapter 4).

As the improvements in the model update from the use of localization in the assimilation of production and seismic data on this 3D case is not so evident, in the next chapter, an alternative, innovative approach for the assimilation of 4D seismic observations with the EnKF will be presented.

Chapter 6

Seismic History Matching of fluid fronts using the Ensemble Kalman Filter[i]

TIME-LAPSE seismic data provide information on the dynamics of multi-phase reservoir fluid flow in places where no production data from wells are available. This information could in principle be used to estimate unknown reservoir properties. However, the amount, resolution and character of the data has long posed significant challenges for quantitative use in assisted history matching workflows. Previous studies have therefore generally investigated methods for updating single models with reduced parameter uncertainty space. Recent developments in ensemble-based history matching methods have shown the feasibility of multi-model history matching of production data while maintaining a full uncertainty description. Here we introduce a robust and flexible reparameterization for interpreted fluid fronts or seismic attribute isolines that extends these developments to seismic history matching. The seismic data set is reparameterized in terms of arrival times at observed front positions, thereby significantly reducing the number of data, while retaining essential information. A simple 1D example is used to introduce the concepts of the approach. A synthetic 3D example with spatial complexity that is typical for many water floods is examined in detail. History matching cases based on both separate and combined use of production and seismic data are examined. It is shown that consistent multi-model history matches can be obtained without the need for reduction of the para-

[i]This chapter has been accepted for publication as a journal paper in *SPE Journal* (Trani *et al.*, 2012). Note that minor changes have been introduced to make the text consistent with the other chapters of this thesis.

meter space or for localization of the impact of observations. The quality of forecasts based on the history matched models is evaluated by simulating both expected production and saturation changes throughout the field for a fixed operating strategy. It is shown that bias and uncertainty in the forecasts of both production at existing wells and of the flooded area are reduced considerably when both production and seismic data are incorporated. The proposed workflow therefore enables better decisions on field developments that require optimal placement of infill wells.

6.1 Introduction

Time variations in reflection seismic data can be attributed to changes in pore saturation and pressure, when ignoring compaction and repeatability issues. Time-lapse seismic data therefore provide information on the dynamics of multi-phase reservoir fluid flow in places where no direct measurements from wells are available. While this has led to time-lapse seismic becoming a valuable qualitative monitoring tool, for example in oil recovery projects -e.g. de Waal & Calvert (2003), Foster (2007)-, quantitative use of seismic data in assisted history matching workflows still remains challenging. Often a single solution in terms of seismic properties (i.e. seismic velocities and/or densities or seismic impedances) is derived through seismic inversion without a formal error estimate. Moreover, the interpretation in terms of pressures and saturations requires additional rock physics models, of which the uncertainty is difficult to quantify. Model based stochastic inversion methods such as proposed by Leguijt (2001, 2009) can take the non-uniqueness and the uncertainty of the solution properly into account. However, it is not common practice yet to combine such results quantitatively with assisted history matching methods. Practical and computational constraints posed by the available seismic inversion and history matching algorithms or software tools are often the reason.

Several studies have been reported over the past 10 years in which quantitative approaches were investigated for incorporating the large numbers of data associated with seismic acquisition into existing workflows for assisted history matching of production data (Arenas *et al.*, 2001; van Ditzhuijzen *et al.*, 2001; Gosselin *et al.*, 2006; Fagervik *et al.*, 2001; Dong & Oliver, 2003; Portella & Emerick, 2005; Haverl *et al.*, 2005; Stephen & MacBeth, 2006; Roggero *et al.*, 2007; Dadashpour *et al.*, 2007). For computational reasons the workflows used in most of these studies require significant reduction of the uncertainty space, or produce only a single history matched model.

Parallel to these efforts, new algorithms to solve the mathematical data-

assimilation problem have been explored that offer the possibility of proper handling of all uncertainties as well as multi-model history matching. One example of such algorithms is the Ensemble Kalman Filter (see e.g. Aanonsen *et al.* (2009) for a recent review). The Ensemble Kalman Filter (EnKF) was introduced as a method for solving reservoir parameter estimation problems by Nævdal *et al.* (2002), after having been successfully applied to dynamic state estimation problems in fields such as meteorology and oceanography. It has since been shown to be well suited for reservoir history matching under many different settings. Some of the attractive features as a method for history matching are its sequential nature, which enables the incorporation of new data without the need to reconsider all previous data, the representation of uncertainty through the use of a model ensemble, the consistent time-evolving weighting of model and data contributions based on model and measurement error covariances, the flexible treatment of any kind and number of data or uncertain parameters, a large and active research community, and a rigorous theoretical basis. The main assumptions underlying the EnKF model update are that the errors in all variables approximately adhere to a multi-variate Gaussian distribution and that this uncertainty can be adequately characterized by an ensemble of models (or 'realizations') of limited size.

Application of the EnKF to seismic history matching has been studied in both synthetic and real field settings (Skjervheim *et al.*, 2007; Haverl & Skjervheim, 2008; Fahimuddin *et al.*, 2011; Leeuwenburgh *et al.*, 2011). While several successes could be reported, different authors have noted that incorporation of very large numbers of data may cause gradual loss of rank in the ensemble, leading to unreliable uncertainty estimates and eventually to filter divergence. The standard approach to address this problem is localization, which aims to increase the effective dimension of the solution space as well as reduce sampling errors -for applications in reservoir contexts see e.g. Arroyo-Negrete *et al.* (2006); Chen & Oliver (2010); Emerick & Reynolds (2010)-. A potential disadvantage of localization is the introduction of geologically unrealistic discontinuities in the property fields.

Results from 2D and 3D synthetic studies (Skjervheim *et al.*, 2006; Leeuwenburgh *et al.*, 2011) have suggested that when the base survey data is properly incorporated and local updating is performed, the extraction of information from grid-based time-lapse seismic may still not be as effective as one would perhaps expect. Possible reasons are the fact that the error variance of difference data is twice that of the individual data, and accumulation of errors in the estimated initial state, or in the simulated base survey data, due to non-linearity or non-Gaussianity (Zhao *et al.*, 2008). The strongly non-Gaussian

distribution of both states (saturation) and seismic attributes at fluid contacts and flood fronts violates a basic assumption underlying Kalman-type filters. Some solutions have been proposed for dealing with non-Gaussian state updates, including the use of constrained and Gaussian mixture versions of the EnKF (Phale & Oliver, 2011; Dovera & Della Rossa, 2010), and transformation or reparameterization of state variables (Gu & Oliver, 2007; Chen *et al.*, 2009). The latter study proposed a time reparameterization for saturation states near the front position, similar to the concept of time-of-flight used in methods based on streamline simulation. Unlike amplitude sensitivities, travel-time sensitivities have been shown to be quasilinear with respect to reservoir properties (He *et al.*, 2001) and to follow a more Gaussian distribution (see figure 5 of Chen *et al.* (2009)). Wu & Datta-Gupta (2002) used this result to introduce a generalized travel-time reparameterization of production data for use in history matching with finite-difference simulators. Their inversion method involved sensitivity-based optimization of the time-shift in the simulated WCT profile. Kretz *et al.* (2004) suggested that the time-of-flight concept could be used for seismic history matching as well. They proposed a method based on streamline simulation and applied it to matching of water flood fronts resulting from a classification of 'seismic facies' in simple 2D cases. The geostatistical properties of the permeability field were lost however as updates were primarily determined by the streamline pattern. Jin *et al.* (2011) recently also considered the use of flood front information for seismic history matching. They used a global optimization method to estimate a small number of parameters by minimization of the difference between observed and simulated flooded area. No further details of their approach were provided.

In this chapter we describe a new and robust approach to multi-model seismic history matching of displacement-type recovery processes that combines the strong points of the EnKF with those of approaches based on time reparameterization, and can be used with full-physics finite-difference reservoir simulators. In particular, we argue that any type of seismic attribute data grid can be reparameterized into travel times for any number of isolines of that particular attribute, and that these can subsequently be incorporated into an ensemble of models using the Ensemble Kalman Filter. This approach potentially has several strong points. The isoline corresponding to the fluid front position can in most cases be reliably detected from any seismic attribute. This means in principle that no inversion of seismic amplitudes to reservoir properties is required. The specification of a limited number of isolines (one corresponding to the case where only the flood front is identified) results in a severe reduction in the number of data while still capturing the

most reliable and important information contained in the data. The number of isolines can be chosen based on the accuracy of the data. The EnKF enables adherence to specified two-point geostatistics as well as improved uncertainty management because of the use of an ensemble of models. Finally, both the more favorable distribution and the reduction in the number of data are expected to enhance the functioning of the EnKF relative to alternative, computationally expensive or otherwise sub-optimal approaches.

Good examples of time-lapse seismic anomalies that can be attributed to saturation changes, and that can easily be transformed into front position data are extensive in the literature (for an overview, see Calvert (2005)). In particular the example of the Draugen field (Gabriels *et al.*, 1999) is representative of the type of reservoir that will be investigated in this study. The same technique could probably be applied for CO_2 storage in aquifers as well, where similar fronts could be discerned. This is exemplified in a study carried out at (Arts *et al.*, 2009).

The chapter is organized as follows. First, we introduce the basic ideas behind the proposed approach with a simple example. Next, we apply the method to a realistic 3D reservoir case. We describe a series of history matching experiments that include both production and seismic data and discuss the quality of both history match and production forecasts obtained with the updated models. Finally, we investigate the quality of forecasts of fluid front positions and discuss the potential for improved reservoir management.

6.2 Methodology

In order to introduce the ideas behind the proposed method, we will start by considering a quasi-1D oil reservoir with a length of 1000 m and a width and height of 25m. For simulation purposes the reservoir is discretized into 250 grid cells of 4 m length each. An injection and a production well, operated at constant pressures of 300 and 250 bar respectively, are positioned at opposite ends of the reservoir. We assume that the permeability in the reservoir is not known exactly, and that an ensemble of 250 log-normally distributed permeability realizations adequately represents the uncertainty (figure 6.1d). One additional realization is chosen as the truth. A weakly non-linear poro-perm relationship is used to generate porosity values. Incompressible and immiscible flow dynamics are used to simulate the replacement of the oil by water flooding. Figure 6.1a shows the water saturation profiles for the model ensemble and truth after 1.6 years. The variability in permeability values produces a wide range of front positions for different ensemble members. The position of the oil-water front is easily identified as the distance from

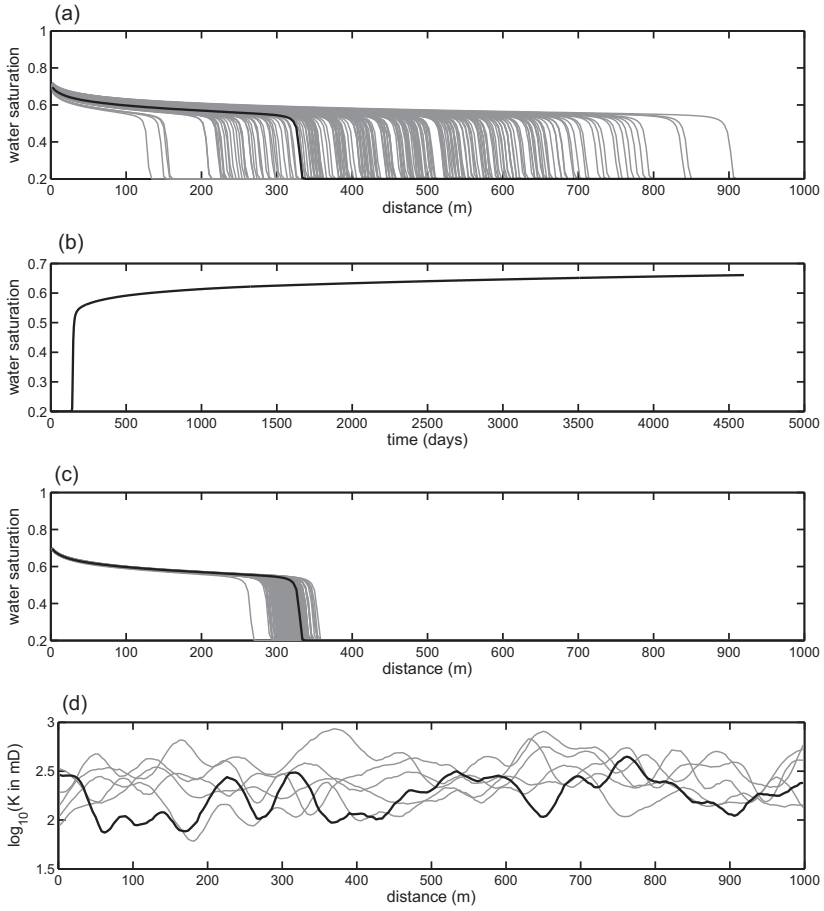

Figure 6.1: *Water saturation and permeability profiles for a quasi-1D oil reservoir with a water injector and a producer positioned 1000 m apart. The gray lines correspond to a model ensemble and the black line represents the true profile. (a) Water saturation profiles after 1.6 years. (b) Change of water saturation with time at a fixed location. (c) Water saturation profiles after a single permeability update with the EnKF based on front arrival times. Fronts are defined as the 0.35 saturation points and the observed front position is interpreted from the true saturation profile. The observed arrival time at this position corresponds to the time of the survey, i.e. 1.6 years. (d) True permeability and and five randomly chosen ensemble profiles before updating.*

the injector at which a sharp jump is observed in the saturation. In this example, the front position is defined as the distance at which the saturation equals 0.35.

Some quick observations can already be made based on figure 6.1; (1) by far the largest change in saturation is observed right at the front, (2) saturation levels behind the front increase monotonically with the distance to the front, (3) behind the front, the saturation curves level off quite rapidly, and subsequently show a very small rate of increase in saturation over time, (4) precise saturation levels behind the front may be very difficult to resolve from the data considering typical measurement error magnitudes, (5) if the front has not yet arrived at a specific location, the saturation at that location does not provide any information on the actual position of the front.

We note that while in the 1D case the position of the front corresponds in a unique way to the distance from the injector, this is not necessarily the case in 2D or 3D, or in cases with multiple injection wells. An alternative measure that may be used in such general cases is the time at which the simulated oil-water front arrives at the observed position. Figure 6.2a shows the ensemble distribution of the log time of arrival of simulated fronts at the position indicated by the solid black line in figure 6.1. It can be seen that the distribution of simulated log arrival times is close to Gaussian, in agreement with the conclusion of He *et al.* (2001) that the sensitivity of the travel-time along streamlines is quasilinear with respect to reservoir properties.

As already mentioned, this may not exactly be the case in more complex reservoir settings in which different flow paths may be followed in different model realizations, but it is likely to be a good first order approximation. Note that some additional simulation time is generally required to obtain arrival times for all ensemble members, similar to the requirement for use of generalized travel-times to match water cut data.

The Gaussian character of the ensemble distribution of the data after reparameterization in terms of time makes it particularly suitable for history matching with the EnKF. One model ensemble update was performed with the EnKF based on a single measurement of the front arrival time at the observed position. The implementation of the EnKF used in this study is based on the perturbation form introduced by Burgers *et al.* (1998). In this scheme the uncertainty in the data is taken into account by generating an ensemble of measurements by adding random perturbations proportional to the measurement error to the measured value. For further details on the EnKF we refer to Aanonsen *et al.* (2009). Here, a measurement error of 0.1 was assumed (this value can be compared with the ensemble distribution shown in figure 6.2a, suggesting that the measurement in this case is more

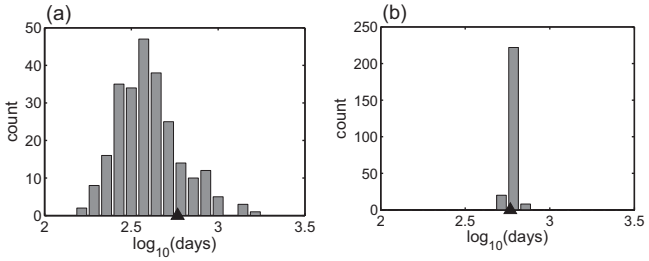

Figure 6.2: *Histograms showing the distribution of simulated front arrival times. The true value is indicated by the triangle. (a) Prior ensemble. (b) Posterior ensemble after one EnKF update.*

accurate than the model forecast). Figure 6.1c shows the water saturation profiles resulting from simulating the updated ensemble again for 1.6 years, while figure 6.2b shows the updated distribution of log arrival times. The plots confirm that the updated models reproduce the observed saturation profile quite well by repositioning of the front.

In the above example, the front is identified as the position where the saturation equals 0.35. In 2D this would be a closed contour, while in 3D the front positions would constitute a surface. If the accuracy of the data is such that variations in saturation values could be resolved behind the front, additional saturation thresholds can be specified as secondary, tertiary etc. fronts. Arrival times associated with these secondary fronts can then be incorporated in exactly the same way as for the primary front. Some consideration should be given here to the estimation of appropriate measurement errors for the secondary front arrival times. Assuming for example that saturation values can be interpreted from the seismic data with an accuracy of 0.1, in the 1D example this will translate to a positioning uncertainty of the primary front of a few 10s of meters at most, since the jump from initial to front saturation is typically much larger than this (almost 0.4 in the above example). Accurate positioning of a secondary front becomes much more difficult, however, since a saturation error of 0.1 easily translates to several hundreds of meters in lateral displacement for thresholds higher than the front saturation. These positioning errors translate to large errors in arrival time of the secondary front (figure 6.1b). In order to test the added value of incorporating secondary front information, a second EnKF update was performed with the 1D model using the time that the 0.6 threshold was exceeded as a measurement. A modestly increased measurement error of 1.0 was assumed. The resulting update was found to be very weak and simulated saturation profiles were

visually almost indistinguishable from those based on incorporation of the primary front arrival time only (not shown). This suggests that, even when high-accuracy seismic data are available, history matching of the primary front arrival time will be by far the most effective way to incorporate the information that can be extracted from (time-lapse) seismic data.

6.3 Realistic 3D test case

In this section we will apply the proposed methodology to a realistic synthetic 3D reservoir. The reservoir has an anticlinal structure, and the geometry is based on the synthetic Brugge Field (Peters *et al.*, 2009). The reservoir model consists of $74 \times 24 \times 7$ grid blocks, with average grid block size of $150 \times 150 \times 4.5$ m, corresponding to a total area of approximately 11.1×3.6 km. The reservoir rock is assumed to consist of sandstones with Gaussian distributed porosity between values of 0.05 and 0.34, and log-normally distributed permeability values between 5 and 5000 mD. A poro-perm relationship links porosity and permeability. Sequential Gaussian Simulation (SGS) is used to generate realizations of porosity and permeability to define both a synthetic truth and an ensemble of 100 models to be used with the EnKF. The ensemble is not conditioned to the properties of the synthetic truth at well locations. The variogram used for the SGS has major and minor horizontal correlation lengths of 5000 m and 500 m respectively, and a vertical correlation length of 30 m, which corresponds roughly to the thickness of the reservoir. The azimuth used for the synthetic truth is 80^oW while random azimuths between 65^oW and 90^oW are used for the ensemble members in order to introduce additional uncertainty. The same poro-perm relationship is used for the synthetic truth and for the ensemble members. Figure 6.3 shows the permeability and the porosity for layers 1 and 6 of the synthetic truth. Figure 6.4 shows the permeability and the porosity for an arbitrary ensemble member. Elongated features with relatively strong property contrasts are present, which are expected to result in highly variable preferential flow paths and front positions.

The reservoir is filled with water and undersaturated oil, with the initial oil-water contact (OWC) positioned about 90 m below the top of the anticline. A total of 17 producing wells are located on the crest, and 10 water injectors are positioned along the initial OWC in order to maintain sufficient pressure for the gas to remain completely dissolved during production. A boundary fault and a non-permeable top layer seal the reservoir completely, allowing in- and outflow to occur only at the wells. During the simulation, the producers are constrained by fixed bottom hole pressure, and the injectors by fixed

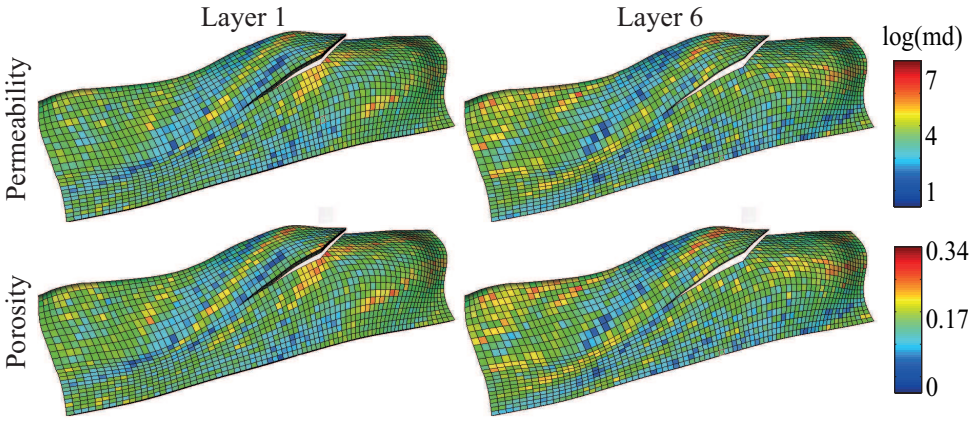

Figure 6.3: *Natural logarithm of permeability and porosity for layers 1 and 6 of the synthetic truth.*

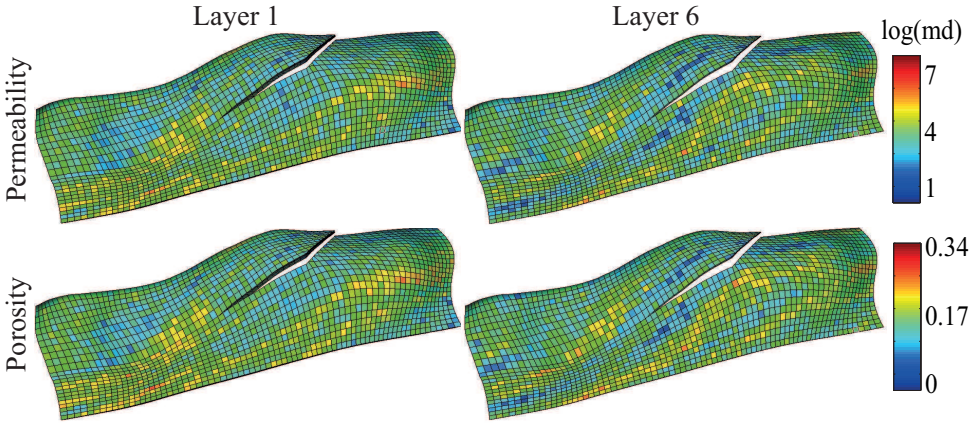

Figure 6.4: *Natural logarithm of permeability and porosity for layers 1 and 6 of ensemble member 50.*

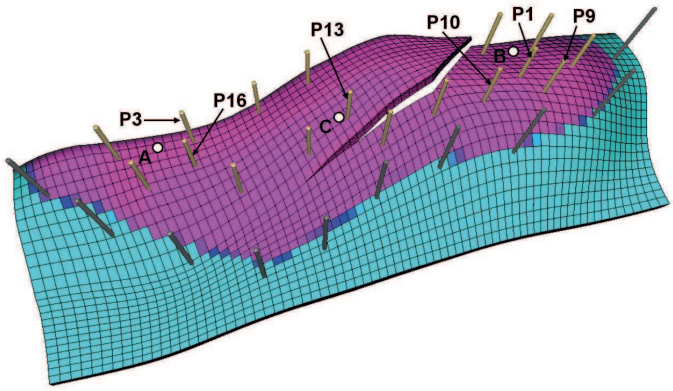

Figure 6.5: *Well configuration and initial saturation for the 3D model. The injectors (dark gray) are positioned along the initial OWC. The producers (light brown) penetrate the top of the anticline. The white circles indicate the positions of grid blocks A, B, and C.*

injection rate. Production wells are not shut in after reaching high water cuts. The positions of the wells are shown in figure 6.5.

Figure 6.6 shows map views of the water saturation in layer 1 (the top layer) after 5000 days of production for the synthetic truth and two arbitrary ensemble members. Also indicated by contours are the positions of the water front in layers 1 and 6. The front (OWC) can be seen to advance progressively towards the top of the anticline. Differences in apparent position of the front in the top and bottom layers can be related to the slope and thickness of the reservoir. The strong heterogeneity in the reservoir properties causes a highly uneven lateral front and saturation profile behind the front. Here and in later experiments, the front is identified with the contour where the variation in saturation is 0.1. The grid cells corresponding to this contour are identified by a search through the grid for cells fulfilling the conditions that they have a saturation value higher than the front saturation value and at the same time also have neighboring cells with saturations lower than this value.

6.4 Description of history matching experiments

The 3D reservoir model discussed in the previous section will be used in a series of history matching experiments. In this section both the production and seismic measurements will be described.

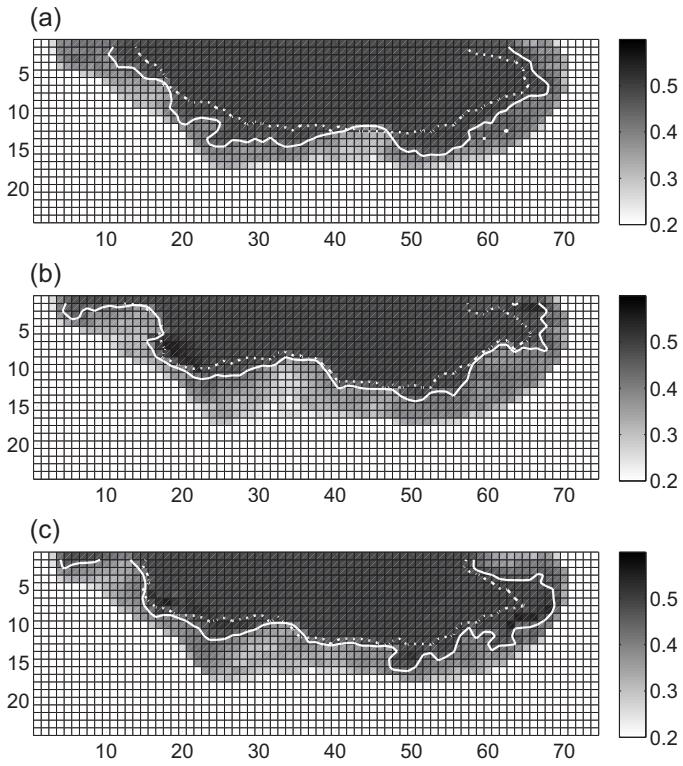

Figure 6.6: *Water saturation in the top layer (gray scale) and front positions in the top layer (solid contour) and layer 6 (dashed contour) after 5000 days. (a) true reservoir (b) ensemble member 2 (c) ensemble member 3.*

Bottom hole pressures (BHP), water rates (WR), and oil rates (OR) are measured at all wells, with measurement error standard deviations of 50 psi for BHP, and 10% relative errors for rates. Because of the rate and pressure constraints imposed, a total of 10 independent BHP and 34 independent rate measurements are assumed to be acquired at 500 day intervals.

In addition to well data, four maps of saturation changes, as obtained for example by inversion of time-lapse seismic data, are assumed to be available from seismic surveys at 2500 day intervals. Note that any attribute could be used, but we use saturation since it is already available after simulating the true reservoir model. The observed position of the fluid front at the time of each seismic survey is determined from the corresponding saturation map as described in the previous section. In our model this results in identification of respectively 812, 693, 673 and 623 front positions at the four repeat survey times. The ensemble realizations are subsequently simulated in order to determine the times at which the simulated fronts arrive at the observed front position. This is done by monitoring the saturation levels at the grid cells corresponding to the observed front and registering the time at which the front saturation is first exceeded. This simple procedure can be implemented with most, if not all, industry-standard simulators. For the front cells for which no arrival time has been obtained 20000 days after the time of the seismic survey t_i, a value of $t_i + 20000$ is assigned in order to limit computation time. Note that in general, additional simulation time can be further restricted by the user if desired. A $\log_{10}$ transformation is applied to all time values and a standard deviation of 0.3 is prescribed for the measurement error. Note that at 10^4 days, this corresponds to an uncertainty of several hundreds of days. In practice, the value of the measurement error will be related to the spatial resolution of the seismic data, systematic and random noise, and inversions errors. We will defer detailed consideration of such errors for now.

Several history matching cases were defined, in which production and seismic data were matched either individually or simultaneously. In Case 1 no data matching and model updating is performed. It illustrates the performance of the prior model ensemble, based only on information about the geostatistical properties of the reservoir. Case2 refers to the case where only production data are matched with the EnKF. Case 3 is the case where only seismic data are matched, and Case 4 refers to the case where production and seismic data are matched simultaneously. The different cases are summarized for reference in Table 1.

In order to maintain consistency between reservoir parameters and dynamic states, only static reservoir parameters are updated and the simulations are restarted from the initial time after each update -see e.g. Wang

case 1	case 2	case 3	case 4
no history matching	well data only	seismic data only	well and seismic data

Table 6.1: *Summary of the experimental cases. Well data are oil and water rates and bottom hole pressures, seismic data are saturations at individual grid blocks. Data errors are as described in the text.*

et al. (2010) and Emerick & Reynolds (2011)-. Initial saturations and pressures are assumed to be known exactly. After the final update at the end of the history match period (day 10000) all updated ensemble models are simulated from day 0 to day 40000. The period from day 10000 to 40000 (i.e. 30000 days in total) after the history match period is subsequently used to verify the predictive power of the updated model ensemble by comparing the predicted production and front movement with that resulting from operating the true reservoir.

6.5 History match and prediction at producing wells

Figure 6.7 shows profiles of the watercut (WCT) of three producing wells (P9, P10, and P1) over the history matching period for the four cases. All three wells experience water breakthrough during the history match period. The figure illustrates that history matching with the EnKF has produced a match to measured production data that from visual inspection appears statistically consistent, i.e. the measured data (true value plus random noise in this synthetic case) continuously lie within the uncertainty band represented by the ensemble.

Figure 6.8 shows time series of the WCT of three different producing wells covering both history match and forecast periods. In each plot the individual ensemble member profiles are represented by gray lines, the ensemble mean is indicated by the dashed line, and the true WCT is indicated by the solid black line. The three wells (P16, P3 and P13) experience water breakthrough only after the history matching period and at substantially varying times during the forecast period. The main factors controlling early breakthrough are the position of the producer with respect to the original OWC, and the heterogeneity of the permeability field. At all three wells the prior model ensemble (case 1) has a large spread, due to the uncertainty in porosity and permeability, and is biased towards early water breakthrough times. Both bias and ensemble spread are generally reduced during the forecast after history matching to any type of data (cases 2 to 4). Incorporation

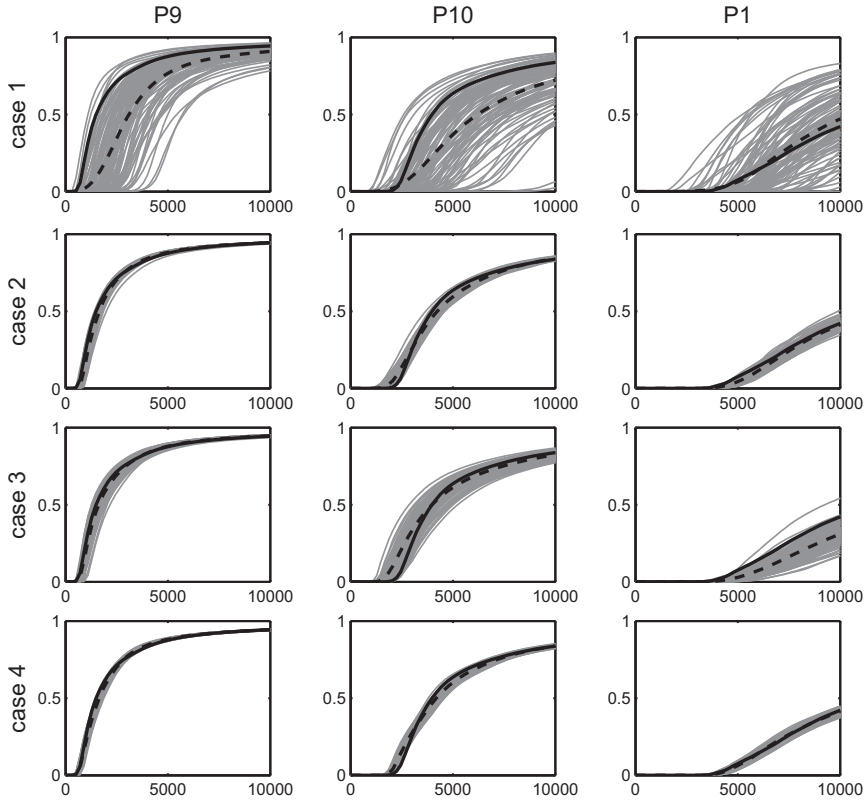

Figure 6.7: *Time series of water cut (vertical axis) for wells P9, P10, and P1 during the history match period (time is in days on the horizontal axis). The individual ensemble members are plotted in gray, the ensemble mean is indicated by the dashed line, and the solid black curve is the true water cut.*

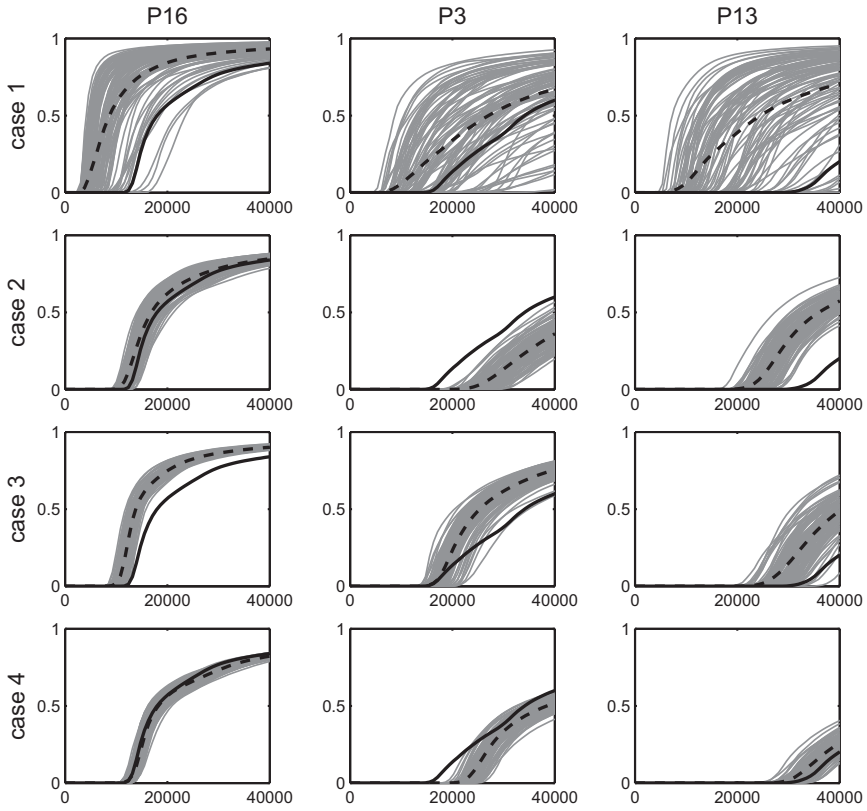

Figure 6.8: *Time series of water cut (vertical axis) for wells P16, P3, and P13 during the entire simulation period, including a 30000 day forecast period (time is in days on the horizontal axis). The individual ensemble members are plotted in gray, the ensemble mean is indicated by the dashed line, and the solid black curve is the true water cut.*

case 1	case 2	case 3	case 4
8066	3081	1124	797

Table 6.2: *RMSE of water breakthrough time in days for the different cases.*

of production data only (case 2) has improved the prediction for well P16 significantly. The prediction for the other two wells, however, remains rather poor due to substantial bias. The suggested uncertainty in the forecast, as indicated by the ensemble spread, is consistently underestimated as evidenced by the fact that the true values are not covered by the ensemble at any time during the forecast period. While the water cut profile for P16 has improved considerably, the estimation of the timing of the water breakthrough at wells P3 and P13 is still rather poor. This can be understood from the positions of the latter two wells, which are situated further away from the original OWC as well as from the position of the front at the end of the history match period. As stated in observation (5) of the Methodology section, the saturation (or in this case, WCT) does not provide any information on the position of the water front since it has not yet arrived at these well positions. Therefore no direct improvement coming from data can be expected at these locations. The assimilation of seismic data only (case 3) improves the timing of the water breakthrough for all wells relative to the unconditioned ensemble. In particular the prediction for the two wells located far from the OWC has improved considerably. The case with production data only provides a poorer prediction than the case with seismic data only, except for well P16, in which water breakthrough occurs shortly after the history match period. The combined use of production and seismic data (case 4) is seen to result in a compromise between the positive contributions of each data type. The prediction of the WCT for P16 and P13 are in fact better than the predictions based on production or seismic alone. Except for the period immediately following water breakthrough at well P3, the forecast uncertainty is consistent with the true values.

Table 6.2 lists the root-mean-square error (RMSE) in days for the prediction of the water breakthrough times in all production wells provided by the four different cases. While incorporation of production data considerably reduces the forecast error relative to the prior ensemble, seismic data is seen to be particularly valuable in improving the forecast. The reason for this will become clear when we consider the effect of the repositioning of the front in the next section.

Figure 6.9 shows the true and the estimated natural logarithm of per-

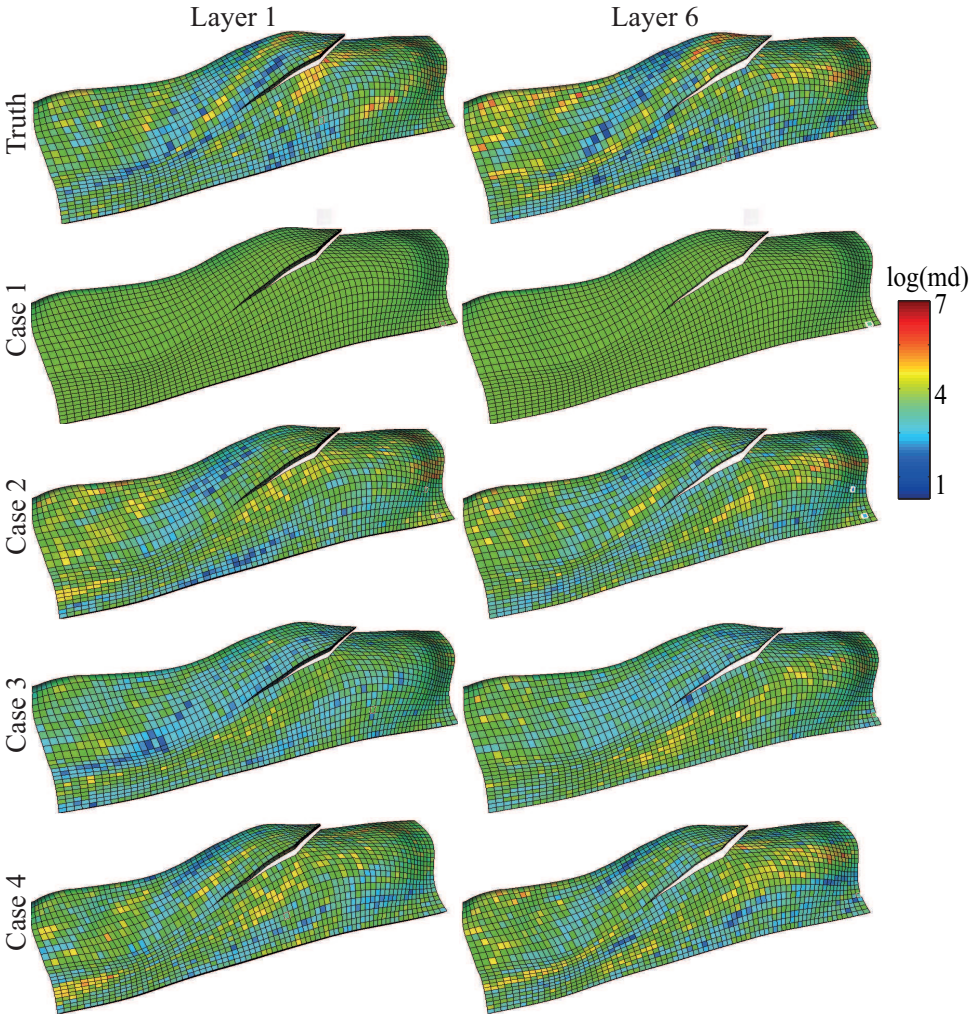

Figure 6.9: *True natural logarithm of permeability in mD of layer 1 and 6 and the corresponding estimates at the end of the history match for the four cases.*

meability for layers 1 (left column) and 6 (right column) at the end of the history match for the four different cases. The field represent the mean over all ensemble members. The prior mean does not show any predominant structure due the fact that no conditioning was done at the well locations, resulting in a nearly homogeneous field. Elongated structures, similar to those seen in the synthetic truth, are recovered in all three history match cases. Visual inspection suggests that magnitudes and scales of the permeability structures are in agreement with those of the truth. Since the global EnKF analysis used here can be shown to be a linear combination of the prior ensemble members, we expect scales to remain consistent with the a priori specified geostatistics. We do not see over-estimation of amplitudes.

6.6 History match and water front prediction

So far we have assessed the quality of the history match and the subsequent forecast in terms of behavior in the producing wells, and by the similarity of the estimated property distribution in the reservoir with that of the synthetic truth. In this section we will investigate the reason for the relatively poor forecast resulting from the use of production data only, and for the substantial improvements obtained by the use of front information.

Figure 6.10 illustrates the uncertainty in the position of the front in layers 1 and 6 for a forecast up to time 40000 for all four cases. The uncertainty is indicated by the dark gray zone and represents the collection of front cells in the entire ensemble. For reference both the true position and the initial OWC are also indicated in each panel . The forecast based on the prior ensemble produces a very large spread in front positions. Incorporation of production data only is sufficient to reduce the spread considerably. However, the remaining spread represents an uncertainty of up to 0.5 km in the front position and 10000 days in front arrival time. The two cases incorporating front arrival time information result in a further reduction of the uncertainty, and a repositioning of the ensemble fronts around the true position.

These results are further quantified in Table 6.3, which lists both the mean value and the standard deviation of the errors in the simulated front arrival times calculated for all grid cells along the observed front position at time 40000 days. Both the error in the mean forecast and the estimated forecast uncertainty (spread around the mean) are reduced by incorporating data, with the smallest errors obtained when both production and seismic are used. It should be noted here that the estimated forecast uncertainty appears to consistently underestimate the actual forecast error, and at this point should therefore probably be used with caution. Further discussion on

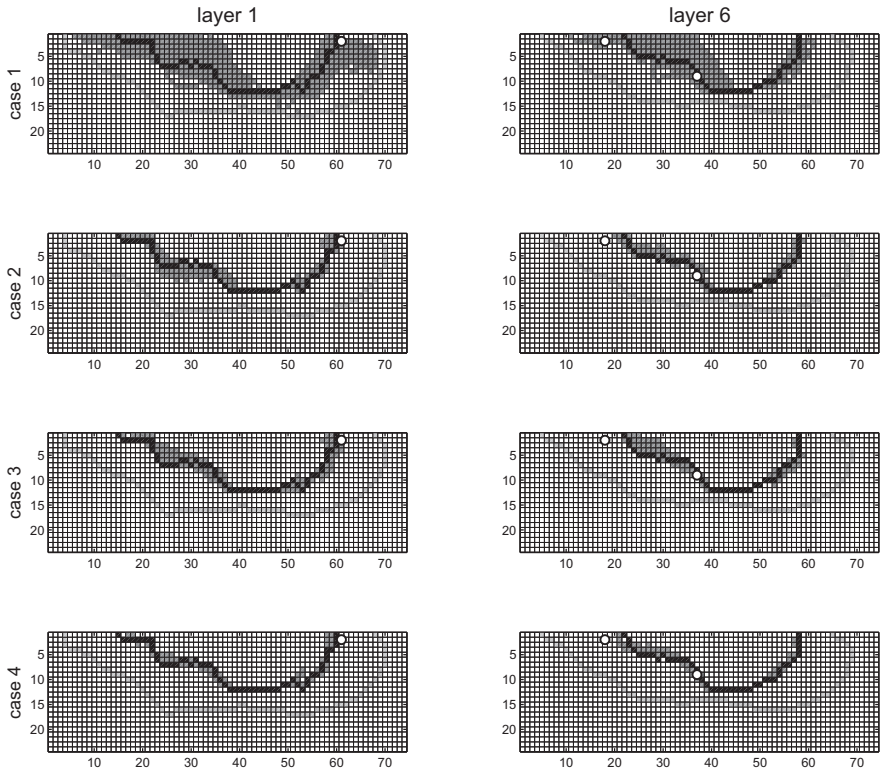

Figure 6.10: *Prediction of the water front position in layers 1 and 6 (top view) at time 40000 days for the four cases. The original OWC is indicated in light gray. The collection of ensemble front positions is shown in dark gray, and the true front position is shown in black. The circles indicate the positions of the grid blocks A, B and C.*

	case 1	case 2	case 3	case 4
STDV	0.213	0.065	0.057	0.039
RMSE	0.641	0.582	0.591	0.580

Table 6.3: *Average standard deviation of ensemble spread in predicted front arrival time along the grid cells of the observed front (STDV), and root-mean-squared error in the predicted front arrival time at the grid cells of the observed front (RMSE). Both values are in $\log_{10}$ days and are determined at the end of the forecast period (40000 days).*

the reliability of forecast uncertainty in the EnKF can be found in Lorentzen *et al.* (2011) and Thulin *et al.* (2011).

Figure 6.11 shows predictions of the change in saturation over time in the 3 grid blocks labeled A, B and C in figure 6.5. As for the three wells shown in figure 6.8, the grid blocks were selected based on the different times at which the front (or OWC) arrives at these locations. In all three grid blocks, the front arrives a significant time after the end of the history match period, thus providing a good means to validate the predictive power of the history matched models. As in figures 6.7 and 6.8, the saturation profiles for the ensemble members are plotted in light gray, the ensemble means are indicated by the dashed black lines, and the true change in saturation is indicated by the solid black line. The results are very similar to those found for the prediction of the water breakthrough at producing wells. The spread in the prior ensemble reflects the huge uncertainty associated with the property distribution in the reservoir, and at points B and C is strongly biased towards too early arrival times. The incorporation of production data leads to a reduced front progression, but predictions remain systematically biased, and uncertainty estimates are inconsistent with the true data at points A and C, as indicated by poor overlap between the ensemble and true saturation profiles. Only proper use of seismic data is able to eliminate this inconsistency at all three points, where the combined use of production and seismic data also tends to remove the bias, and additionally produces the forecast with the smallest uncertainty.

Finally, figure 6.12 shows the distribution of water front arrival times at the three grid points A, B and C, before and after incorporation of both production and seismic data. Note that these grid positions do not correspond to any of the well positions, and therefore highlight the forecast capability outside of existing wells. The light gray histogram shows the distribution of times simulated by the prior model ensemble, while the dark gray histogram shows the times simulated by the history matched ensemble. The ensemble mean arrival times are indicated by a downward pointing triangle and asterisk, and the measured arrival time is indicated in each panel by an upward pointing triangle. While the prior distribution generally looks somewhat less like a Gaussian, or at least a little more irregular, than in the 1D example, the updated ensemble produces histograms that are nearly Gaussian, a well known property of stochastic (i.e. perturbation based) EnKF algorithms. More importantly, while the arrival time forecast from the prior ensemble is heavily biased at points B and C, the updated ensemble appears to correctly predict the arrival of the water flooding front at all three positions.

Figures 6.10 to 6.12 suggest that field development decisions involving

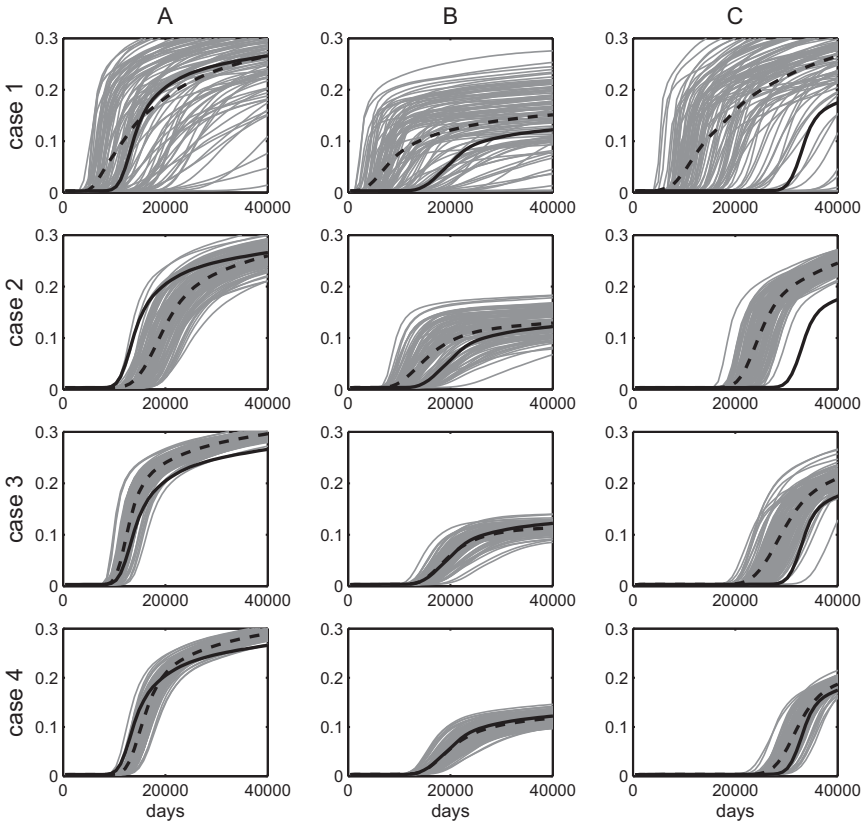

Figure 6.11: *Time series of saturation change at the same grid blocks (A, B, and C) as in figure 6.12. The individual ensemble members are plotted in gray, the ensemble mean is indicated by the dashed line, and the solid black curve is the true saturation change profile.*

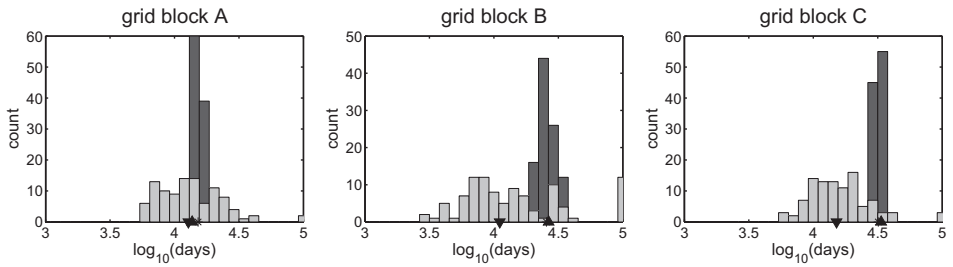

Figure 6.12: *Histograms showing the ensemble distribution of simulated front arrival times at 3 different grid blocks (A, B and C). The prior distribution is shown in light gray, and the posterior distribution after history matching to production and seismic data (case 4) is shown in dark gray. The sum of all counts equals the ensemble size which is 100. The downward pointing triangle indicates the prior mean, and the upward pointing triangle the true value. An asterisk indicates the mean after history matching.*

the placement of infill wells can be taken with significantly higher confidence when seismic data are properly incorporated in the history match. By reducing the uncertainty in the front position, a better estimate of optimal locations can be made at the time of any revision in the development plan. Moreover, production scenarios for existing well configurations can be optimized based on estimated arrival times of the front. These results are consistent with those of Peters (2011), who demonstrated that a good history match and prediction for existing wells based on production data only does not guarantee an accurate prediction for new infill wells.

6.7 Discussion

A reparameterization of seismic data into front arrival times, and subsequent incorporation in an ensemble-based assisted history matching scheme was presented. Such a reparameterization could be compared with the approach taken in streamline-based history matching -for reviews and references see e.g. Datta-Gupta & King (2007); Thiele *et al.* (2007); Stenerud (2007)-. In the streamline-based approach, streamline simulation is used to identify streamtubes that carry a fixed volumetric flux. Within each tube, the flow problem is transformed into 1D, with the state variable being the time of flight. By adjusting the permeability along the streamlines, the time of flight, or the travel time of water along the streamlines, can be influenced very efficiently since streamline simulators are generally fast. Their advantages may disappear to some extent for cases that involve changing well or field

conditions that affect drainage areas, or more general, in cases where the flow is less defined as in capillary and gravity dominated flow or in strong compressibility induced flow (Thiele *et al.*, 2010).

In the EnKF-based approach the parameters that are to be estimated are not limited to grid block properties along flow paths such as porosity and permeability. No approximations are required in the physics, although this leads to some additional computational cost relative to the streamline approach. Furthermore, the method includes an automatic implicit assessment of uncertainty, and consistent weighting of models and data types, that may evolve over time with both the dynamics in the reservoir and with changes in the well configuration.

The reparameterization of seismic data into front arrival times is similar to the reparameterization of WCT data into travel-times of Wu & Datta-Gupta (2002). They noted that the quasilinear sensitivity of travel-time misfit to reservoir properties will speed up iterative minimization procedures. We find that it also has several advantages for the functioning of the EnKF. It enables the transformation into a quantity with a more continuous and, most probably, more Gaussian-like distribution than saturation or simulated seismic attributes. This motivated the use of a similar reparameterization of saturation by Chen *et al.* (2009) for the purpose of updating dynamic reservoir model states with the EnKF. Furthermore, it enables the reduction of the data set to a select number of isolines only. It has been observed that the huge amount of data associated with seismic surveys may have a detrimental effect on the functioning of the EnKF. Including fewer seismic measurements, while preserving the most relevant information, improves the functioning of the filter without the need for remedies like localization and inflation.

In this study we considered the availability of inverted saturation maps only. In general, neglecting compaction or subsidence effects, time-lapse variations of seismic attributes are the combined expression of changes both in saturation and in pressure (Landrø, 2001; Trani *et al.*, 2011). We focused on waterflooding fieldcases, where changes are predominantly ascribed to changes in saturation -e.g. Gabriels *et al.* (1999)-. Other potential applications are related to $C0_2$ injection experiments like at Sleipner (Arts *et al.*, 2009) for which the main changes in seismic attributes are predominantly caused by saturation changes. In such cases explicit inversion into saturation changes is not necessary, and seismic attributes can be reparameterized directly into front arrival times. In cases where the front can not be sharply resolved from the data, e.g. bottom drives with a vertically climbing front, inversion of the seismic waveforms to some type of attribute will ultimately

still result in an estimate of volume displacement, and therefore indirectly a contact displacement, at a particular location. So while the front or contact cannot perhaps be directly detected in the data, its position is typically inferred through alternative routes. While this would take away the benefit of not requiring explicit seismic inversion, the benefits of the reparameterization for the functioning of the history matching scheme will still hold.

In this synthetic experiment the prescribed measurement error for reparameterized seismic data was chosen somewhat arbitrarily for the purpose of demonstrating the proposed method. In actual field cases, the error in the arrival time measurement results from the limited accuracy of the seismic data, including uncertainties in (time-lapse) acquisition, processing and interpretation. The main source of uncertainty in acquisition and processing can be attributed to the lack of repeatability, whereas the interpretation of time-lapse results requires some understanding of the processes through an underlying rock physics model. Other acquisition errors are in principle associated with the fact that the seismic survey may take several days to be completed, however this period is very short relative to reservoir processes such as water flooding and this error contribution is therefore expected to be very small. The spatial accuracy with which the position of the front can be picked is also related to the resolution of the seismic data. This spatial resolution is generally sufficient to allow a clear identification of the front. More difficult may be the association of the interpreted front with e.g. a particular saturation value. On the coarse grid resolution of a typical reservoir model, a small error in saturation value may be related to a significant error in arrival time for a specific grid block. Also, this error may be systematic rather than random along the front. Since such a bias translates to a bias in the flooded area, for prescribed water injection totals, this could be interpreted as a bias in pore volume behind the front. Further study may be required into ways to identify and correct such systematic errors. Factors that affect the validity of the reservoir model flow dynamics include relative permeabilities, well constraints, initial OWC, structural uncertainty etc. None of these uncertainties were included in this study, and only uncertainty in grid block properties was considered. It should be pointed out, however, that all of these types of uncertainties can be handled by the EnKF, as demonstrated by numerous examples from the literature. It should be obvious that application of the methods described in this manuscript to actual field cases would require consideration of uncertainties relevant for each individual case.

6.8 Conclusions

In this study a new robust approach to seismic history matching was proposed that combines a reparameterization of seismic data into front arrival times with incorporation in an ensemble-based assisted history matching scheme. It was demonstrated in synthetic 1D and more realistic 3D examples that the method performs very well and produces models with improved match to both production and seismic data and with considerably improved forecast skill both at and in between wells. The proposed approach builds on earlier work on reparameterization of both states and data, and incorporates features of streamline-based approaches while maintaining the flexibility and full physics options of finite difference simulators. The method can be implemented with any industry-standard simulator and offers interesting potential advantages with respect to alternative approaches that have been presented elsewhere: the reparameterization into arrival times enables a very large reduction in number of data while retaining the essential information content, there is no need for a seismic inversion when only the primary front is interpreted, the flexibility to define any desired number of secondary fronts depending on the quality of the data, a more linear sensitivity to reservoir properties and a more Gaussian distribution of simulated measurements, which tends to improve the functioning of inversion methods, while use of the EnKF in particular provides an efficient means to obtain a multi-model history match that incorporates and retains geological information formulated in terms of two-point geostatistics. Any additional simulation time relative to conventional EnKF workflows can be controlled by the user. No localization was required in the experiments and the ensemble spread remained a reliable estimate of model uncertainty.

Chapter 7

Conclusions and recommendations

The main objective of this thesis is to provide an accurate estimate of changes in saturation and pore pressure induced by waterflooding in case of EOR, and to improve the flow model through the assimilation of time-lapse seismic data with the Ensemble Kalman Filter.
This chapter presents the conclusions of this thesis and gives recommendations for future research.

7.1 Conclusions

In order to achieve the first part of the research objective, a 4D seismic inversion scheme is presented. This is based on a modified form of Landrø's (2001) equations and extended with two additional equations expressing the time-shift induced by P- and S-wave velocity changes as functions of pore pressure and saturation changes. This thesis demonstrates that:

- Inversion results of time-lapse seismic data to pressures and saturations improve considerably when taking time-shifts into account. However, the importance of a proper incorporation of lateral variations of porosity remains important.
- By replacing the P-wave gradient equation with the approximation related to the time-shift equation, the leakage between the two estimated variables almost disappears; if time-shift data are not available, the leakage effect is strongly reduced in case the second order terms in relative changes in seismic properties are added in the gradient equation.
- The final estimates seem to be relatively robust to seismic noise. Changes in saturation and pressure present fairly high accuracy in the presence

of random noise up to 15%; in presence of systematic noise, final estimates show biased errors but their main features can still be recognized clearly.

The second part of the research objective has been achieved by proposing two innovative approaches for the assimilation of seismic measurements with the Ensemble Kalman Filter.
The first one is the assimilation of time-lapse changes in fluid saturation and pore pressure. It is well known from literature, that if the number of observations to assimilate is large with respect to the ensemble size, the filter cannot work properly. This effect is called 'filter divergence'. The most successful remedy to this drawback, and probably the best documented in literature, is covariance localization.
The second approach consists of assimilating water front arrival times. This method can be considered as a time-reparameterization of saturation data at the front location.
The conclusions from this study are:

- When the initial ensemble spans the true uncertainty range, the use of seismic measurements, vertically averaged or per gridcell, improves the history matching and the forecast of production data, and the porosity/permeability fields characterizations.

- Covariance localization applied to the Kalman gain is a very effective remedy to filter divergence caused by an excessive number of observations to assimilate. In order to be optimally applied, covariance localization would require the knowledge of the true covariance of measurements with the parameters/states to update. In this thesis it is demonstrated that the covariance of time-lapse changes in saturation and in pressure with the permeability, saturation and pressure fields is influenced by the permeability structure, the past history match (time), and the wells disposition.

- If correctly applied the localized ensemble Kalman filter update outperforms the standard approach with or without any seismic information. Compared to both cases, the localized ensemble Kalman filter update largely improves the history match and the forecast for production data. Furthermore, it improves the porosity and the permeability fields estimates.

- The reparameterization into arrival times enables the assimilation of seismic data with no need for a seismic inversion when only the primary front is interpreted (assuming the waterfront position can be properly identified on time-lapse seismic data). This approach allows the flexibility to define any desired number of secondary fronts. With respect to using saturation data per gridcells, history matching the fluid front arrival time largely reduces the number of data to assimilate, while retaining the essential information content.

- The reparameterization into arrival times presents a more linear sensitivity to reservoir properties, and a more Gaussian distribution of simulated measurements. This tends to improve the functioning of the EnKF which provides an efficient means to obtain a multi-model history match that incorporates and retains geological information formulated in terms of two-point geostatistics.

- The information contained in the arrival times is in itself sufficient to improve the production data fit, resulting in improved estimations of water breakthrough time over both the history match and forecast periods. Furthermore, the combination of production and seismic data provides very accurate predictions of the watercuts at well locations and of front positions. Improving the prediction of the front location is of large value for infill well planning.

7.2 Suggestions for future research

Suggestions for future research are proposed:

- The inversion scheme presented in this thesis should be applied on a real case. This would validate the robustness of the method to real data conditions.

- A study investigating the true covariance between state/parameters to update and seismic measurements might be performed on different 2D and 3D realistic models. This would confirm the guidelines for optimal localization functions as proposed in this thesis or provide suggestions on how to modify those guidelines according to different well configurations, model sizes, geological structures.

- Alternative reparameterization techniques for the assimilation of seismic measurements should be investigated (such as using the distance to the water front, instead of time). Rules-of-thumb for the use of different EnKF parameterizations would be highly appreciated by the oil industry.

Appendix A

The Gauss-Newton method applied to the inversion scheme

According to Newton's method the zeros of a function can be iteratively found with the following formula:

$$x_{n+1} = x_n - \frac{f(x_n)}{f'(x_n)}. \tag{A.1}$$

For an optimization problem Newton's method can also be used to find the zeros of the derivative (minimum):

$$x_{n+1} = x_n - \frac{f'(x_n)}{f''(x_n)}. \tag{A.2}$$

Given m functions ($f1, f2, ..fm$) in n variables $s = (\alpha, \beta, \gamma, ...)$, with m $\geq$ n, the Gauss-Newton algorithm finds the minimum of the sum of squares

$$T(s) = \sum_{i=1}^{m} f_i^2(s). \tag{A.3}$$

The recurrence relation for minimizing the function, according to Newton's method is

$$\mathbf{s^{n+1}} = \mathbf{s^n} - \mathbf{H^{-1}G}, \tag{A.4}$$

where **G** denotes the gradient and **H** the Hessian of T.
The gradient is given by:

$$g_j = 2\sum_{i=1}^{m} f_i \frac{\delta f_i}{\delta s_j}, \tag{A.5}$$

or in matrix notation

$$\mathbf{G} = 2\mathbf{J}^{\mathbf{T}}\mathbf{f} \tag{A.6}$$

Elements of the Hessian are calculated by differentiating the gradient elements with respect to s_k:

$$H_{jk} = 2\sum_{i=1}^{m}\left(\frac{\delta f_i}{\delta s_j}\frac{\delta f_i}{\delta s_k} + f_i\frac{\delta^2, f_i}{\delta s_j \delta s_k}\right), \tag{A.7}$$

or in matrix notation (ignoring the second order derivatives)

$$\mathbf{H} = 2\mathbf{J}^{\mathbf{T}}\mathbf{J}. \tag{A.8}$$

These expressions, substituted into the recurrence relation give

$$\mathbf{s^{n+1}} \approx \mathbf{s^n} - \left(\mathbf{J}^{\mathbf{T}}\mathbf{J}\right)^{-1}\mathbf{J}^{\mathbf{T}}\mathbf{f}, \tag{A.9}$$

where $\mathbf{f}$ is the vector containing the non linear equations in known values (initial guess) of pressure and saturation, and $\mathbf{J}$ the partial derivatives in those values.
The diagonal elements of the 2-by-2 Hessian matrix contain the sum of the squared derivatives of seismic inputs (ΔR_0, ΔG, ΔT_{pp}, and ΔT_{ss}) with respect to ΔS and ΔP. Since these values are nonzero (the derivative of the linear terms in the unknowns are constants) the inversion needs no stabilizing parameter. Furthermore, if pressure is calculated in MPa, no scaling factor is required as the order of magnitude of ΔP is comparable with the one of ΔS.
The method shows convergence if the initial guess is sufficiently close to the minimum (exact ΔS and ΔP) and the functions are weakly non-linear, in order to render valid the approximation of the Hessian.

Appendix B

Reflectivity change including second order terms

Eq. 2.1 describes the reflection coefficient at the top reservoir level for the baseline survey. At the time of the monitor survey the reflection coefficient reads

$$R_1(\theta) = \frac{1}{2}\left(\frac{\delta\rho'}{\rho'} + \frac{\delta\alpha'}{\alpha'}\right) - \frac{2\beta'^2}{\alpha'^2}\left(\frac{\delta\rho'}{\rho'} + \frac{2\delta\beta'}{\beta'}\right)\sin^2(\theta) + \frac{\delta\alpha'}{2\alpha'}\tan^2(\theta), \quad \text{(B.1)}$$

where $\delta\alpha' = \delta\alpha + \Delta\alpha$ and $\alpha' = \alpha\,(1 + \Delta\alpha/2\alpha)$ with $\Delta\alpha$ being the change in P-wave velocity in the reservoir induced by changes in pore saturation and pressure. The same notation holds for β and ρ. Assuming that the relative changes in seismic properties $\Delta\alpha/\alpha \ll 1$, $\Delta\beta/\beta \ll 1$, $\Delta\rho/\rho \ll 1$, and neglecting higher order terms or combinations thereof, $R_1(\theta)$ can be rewritten as:

$$\begin{aligned} R_1(\theta) = {} & \frac{1}{2}\left(\frac{\delta\rho}{\rho} + \frac{\delta\alpha}{\alpha}\right) - \frac{2\beta^2}{\alpha^2}\left(\frac{\delta\rho}{\rho} + \frac{2\delta\beta}{\beta}\right)\sin^2(\theta) + \frac{\delta\alpha}{2\alpha}\tan^2(\theta) \\ & + \frac{1}{2}\left(\frac{\Delta\rho}{\rho} + \frac{\Delta\alpha}{\alpha}\right) - \frac{2\beta^2}{\alpha^2}\left(\frac{\Delta\rho}{\rho} + \frac{2\Delta\beta}{\beta}\right)\sin^2(\theta) + \frac{\Delta\alpha}{2\alpha}\tan^2(\theta) \end{aligned} \quad \text{(B.2)}$$

The time-lapse change in reflectivity $\Delta R(\theta)$ is obtained by subtracting $R_0(\theta)$ (eq.2.1) from $R_1(\theta)$; from $\Delta R(\theta)$ the change in zero-offset reflectivity as well as the change in gradient reflectivity can be extracted (eqs.2.2 and 2.3).
Eq. B.2 has been largely simplified by removing higher order terms in $\Delta\alpha/\alpha$, $\Delta\beta/\beta$, $\Delta\rho/\rho$ or combinations of them. However, if these terms are included, the complete reflectivity at the time of the monitor survey would read (using

Taylor expansion to the first degree for α',β',ρ')

$$\begin{aligned} R_1(\theta) &= \frac{1}{2}\left[\left(\frac{\delta\rho+\Delta\rho}{\rho}\right)\left(1-\frac{\Delta\rho}{2\rho}\right)+\left(\frac{\delta\alpha+\Delta\alpha}{\alpha}\right)\right. \\ &\left.\times\left(1-\frac{\Delta\alpha}{2\alpha}\right)\right]-\frac{2\beta^2\left(1+\frac{\Delta\beta}{2\beta}\right)^2}{\alpha^2\left(1+\frac{\Delta\alpha}{2\alpha}\right)^2} \\ &\times\left[\left(\frac{\delta\rho+\Delta\rho}{\rho}\right)\left(1-\frac{\Delta\rho}{2\rho}\right)+2\left(\frac{\delta\beta+\Delta\beta}{\beta}\right)\right. \\ &\left.\left(1-\frac{\Delta\beta}{2\beta}\right)\right]\sin^2(\theta)+\frac{1}{2}\left(\frac{\delta\alpha+\Delta\alpha}{\alpha}\right)\left(1-\frac{\Delta\alpha}{2\alpha}\right)\tan^2(\theta) \end{aligned} \tag{B.3}$$

To the second order, Eq.B.3 can be rewritten as

$$\begin{aligned} R_1(\theta) &= R_0(\theta)+\frac{1}{2}\left(\frac{\Delta\rho}{\rho}+\frac{\Delta\alpha}{\alpha}\right)-\frac{2\beta^2}{\alpha^2}\left(\frac{\Delta\rho}{\rho}+\frac{2\Delta\beta}{\beta}\right)\sin^2(\theta) \\ &+\frac{\Delta\alpha}{2\alpha}\tan^2(\theta)-\frac{1}{4}\left(\frac{\delta\rho\Delta\rho}{\rho^2}+\frac{(\Delta\rho)^2}{\rho^2}+\frac{\delta\alpha\Delta\alpha}{\alpha^2}+\frac{(\Delta\alpha)^2}{\alpha^2}\right) \\ &-2\frac{\beta^2}{\alpha^2}\left[\frac{\Delta\beta}{\beta}\frac{\delta\rho}{\rho}+\frac{\Delta\beta}{\beta}\frac{\Delta\rho}{\rho}+\frac{\Delta\beta}{\beta}\frac{\delta\beta}{\beta}+\left(\frac{\Delta\beta}{\beta}\right)^2\right. \\ &-\frac{\Delta\alpha}{\alpha}\frac{\delta\rho}{\rho}-\frac{\Delta\alpha}{\alpha}\frac{\Delta\rho}{\rho}-2\frac{\Delta\alpha}{\alpha}\frac{\delta\beta}{\beta}-2\frac{\Delta\alpha}{\alpha}\frac{\Delta\beta}{\beta}-\frac{\delta\rho\Delta\rho}{2\rho^2} \\ &\left.-\frac{(\Delta\rho)^2}{2\rho^2}\right]\sin^2(\theta)-\frac{1}{4}\left(\frac{\delta\alpha\Delta\alpha}{\alpha^2}+\frac{(\Delta\alpha)^2}{\alpha^2}\right)\tan^2(\theta). \end{aligned} \tag{B.4}$$

By subtracting $R_0(\theta)$ and the terms with no angle dependence from eq. B.4, we obtain the gradient reflectivity change. Assuming that the relative changes in seismic velocities are the sum of changes in pressure and in pore saturation, while the relative change in density is only due to saturation variations (see eqs. 2.4-2.6), from eq.B.4 the change in the gradient coefficient

can be rewritten as

$$\begin{aligned}
\Delta G \;=\; & \frac{\Delta\alpha_F}{2\alpha} - \frac{2\beta^2}{\alpha^2}\left(\frac{\Delta\rho_F}{\rho} + \frac{2\Delta\beta_F}{\beta}\right) \\
& -\frac{2\beta^2}{\alpha^2}\left[\frac{\Delta\beta_F}{\beta}\frac{\delta\rho}{\rho} + \frac{\Delta\beta_F}{\beta}\frac{\Delta\rho_F}{\rho} + \frac{\Delta\beta_F}{\beta}\frac{\delta\beta}{\beta} + \left(\frac{\Delta\beta_F}{\beta}\right)^2\right. \\
& \left. -\frac{\Delta\alpha_F}{\alpha}\frac{\delta\rho}{\rho} - \frac{\Delta\alpha_F}{\alpha}\frac{\Delta\rho_F}{\rho} - 2\frac{\Delta\alpha_F}{\alpha}\frac{\delta\beta}{\beta} - 2\frac{\Delta\alpha_F}{\alpha}\frac{\Delta\beta_F}{\beta} - \frac{\delta\rho\Delta\rho_F}{2\rho^2} - \frac{(\Delta\rho_F)^2}{2\rho^2}\right] \\
& -\frac{1}{4}\left(\frac{\delta\alpha\Delta\alpha_F}{\alpha^2} + \frac{(\Delta\alpha_F)^2}{\alpha^2}\right) \\
& +\frac{\Delta\alpha_P}{2\alpha} - \frac{2\beta^2}{\alpha^2}\left(\frac{\Delta\rho_P}{\rho} + \frac{2\Delta\beta_P}{\beta}\right) \\
& -\frac{2\beta^2}{\alpha^2}\left[\frac{\Delta\beta_P}{\beta}\frac{\delta\rho}{\rho} + \frac{\Delta\beta_P}{\beta}\frac{\Delta\rho_P}{\rho} + \frac{\Delta\beta_P}{\beta}\frac{\delta\beta}{\beta} + \left(\frac{\Delta\beta_P}{\beta}\right)^2\right. \\
& \left. -\frac{\Delta\alpha_P}{\alpha}\frac{\delta\rho}{\rho} - \frac{\Delta\alpha_P}{\alpha}\frac{\Delta\rho_P}{\rho} - 2\frac{\Delta\alpha_P}{\alpha}\frac{\delta\beta}{\beta} - 2\frac{\Delta\alpha_P}{\alpha}\frac{\Delta\beta_P}{\beta} - \frac{\delta\rho\Delta\rho_P}{2\rho^2} - \frac{(\Delta\rho_P)^2}{2\rho^2}\right] \\
& -\frac{1}{4}\left(\frac{\delta\alpha\Delta\alpha_P}{\alpha^2} + \frac{(\Delta\alpha_P)^2}{\alpha^2}\right).
\end{aligned} \tag{B.5}$$

The relative changes in seismic properties induced by saturation or pressure changes can be rewritten in a similar way as in eqs.2.7-2.9. However, in this case, we use a linear expansion with respect to changes in both parameters as showed in the following equations:

$$\frac{\Delta\alpha_F}{\alpha} = k_\alpha \Delta S, \tag{B.6}$$

$$\frac{\Delta\alpha_P}{\alpha} = l_\alpha \Delta P, \tag{B.7}$$

$$\frac{\Delta\beta_F}{\beta} = k_\beta \Delta S, \tag{B.8}$$

$$\frac{\Delta\beta_P}{\beta} = l_\beta \Delta P, \tag{B.9}$$

$$\frac{\Delta\rho_F}{\rho} = k_\rho \Delta S, \tag{B.10}$$

$$\frac{\Delta\rho_P}{\rho} \approx 0 \tag{B.11}$$

and grouping similar terms, the coefficient of the gradient reflectivity change becomes

$$\begin{aligned}\Delta G &= \frac{1}{4}k_\alpha \Delta S\left(2-\frac{\delta\alpha}{\alpha}-k_\alpha\Delta S\right)-\frac{2\beta^2}{\alpha^2}\Delta S\left[-k_\alpha\left(\frac{\delta\rho}{\rho}+k_\rho\Delta S+2\frac{\delta\beta}{\beta}+2k_\beta\Delta S\right)\right.\\ &\quad \left.+k_\beta\left(2+\frac{\delta\rho}{\rho}+k_\rho\Delta S+\frac{\delta\beta}{\beta}+k_\beta\Delta S\right)+k_\rho\left(1-\frac{\delta\rho}{2\rho}-\frac{1}{2}k_\rho\Delta S\right)\right]\\ &\quad +\frac{1}{4}l_\alpha\Delta P\left(2-\frac{\delta\alpha}{\alpha}-l_\alpha\Delta P\right)-\frac{2\beta^2}{\alpha^2}\Delta P\left[-l_\alpha\left(\frac{\delta\rho}{\rho}+2\frac{\delta\beta}{\beta}+2l_\beta\Delta P\right)\right.\\ &\quad \left.+l_\beta\left(2+\frac{\delta\rho}{\rho}+\frac{\delta\beta}{\beta}+l_\beta\Delta P\right)\right].\end{aligned} \tag{B.12}$$

Equation B.12 represents, according to Smith & Gidlow (1987), the time-lapse change in gradient reflectivity including second order terms in relative changes in seismic properties rewritten as functions of ΔS and ΔP. Although these functions are linear, eq.B.12, because of the quadratic order or the product between the relative changes, becomes a quadratic expression in both parameters.

Bibliography

Aanonsen, S. I., Nævdal, G., Oliver, D. S., Reynolds, A. C., & Valles, B. 2009. The Ensemble Kalman Filter in reservoir engineering-A review. *SPE Journal*, **14**, 393–412.

Agarwal, B., Hermansen, H., Sylte, J. E., & Thomas, L. K. 2000. Reservoir characterization of Ekofisk field: a giant, fractured chalk reservoir in the Norwegian sea- history match. *SPE Reservoir Evaluation Engineering*, **36**, 534–543.

Agbalaka, C., & Oliver, D. S. 2008. Application of the EnKF and localization to automatic history matching of facies distribution and production data. *Mathematical Geosciences*, **40**, 353–374.

Anderson, B. D., & Moore, J. B. 2005. *Optimal Filtering*. Dover.

Anderson, J. L. 2007. Exploring the need for localization in ensemble data assimilation using a hierarchical ensemble filter. *Physisca D; Nonlinear Phenomena*, **230**.

Anderson, J. L. 2009. Ensemble Kalman Filters for large geophysical applications. *IEE Control Systems Magazine*, **29**, 66–82.

Arenas, E., van Kruijsdijk, C., & Oldenziel, T. 2001. Semi-automatic history matching using the pilot point method including time-lapse seismic data. *SPE Reservoir Evaluation & Engineering (SPE-71634)*.

Arroyo-Negrete, A., Devegowda, D., & Datta-Gupta, A. 2006. Streamline assisted ensemble Kalman filter for rapid continuous reservoir model updating. *SPE International Oil and Gas Conference and Exhibition (SPE 104255)*.

Arts, R., Elsayed, R., van der Meer, L., Eiken, O., Ostmo, S., Chadwick, A., Kirby, G., & B., Zinszner. 2002. Estimation of the mass of injected CO2 at Sleipner using time-lapse seismic data. *64th EAGE Conference & Exhibition incorporating SPE EUROPEC, Expanded Abstracts*.

Arts, R., Eiken, O., Chadwick, A., Zweigel, P., van der Meer, L., & Kirby, G. 2004. monitoring at the Sleipner underground CO_2 storage site (North Sea). *Geological storage of CO_2 for emissions reduction: Geological Society, London, Special Publication*, **233**, 181–191.

Arts, R. J., Chadwick, R. A., Eiken, O., Dortland, S., Trani, M., & van derMeer, L.G. H. 2009. Acoustic and elastic modeling of seismic time-lapse data from the Sleipner CO_2 storage operation. In: M. Grobe, J. C. Pashin, and R. L. Dodge, eds., Carbon dioxide sequestration in geological media-State of the science. *In: AAPG Studies in Geology*.

Aurox, A. 2006. Several data assimilation methods for geophysical problems. *Indian Journal of Pure Applied Mathematics*, **37**, 41–58.

Bengtsson, T., Snyder, C., & Nycha, D. 2003. Toward a nonlinear ensemble filter for high dimensional systems. *Journal of Geophysical Research*, **108**, 35–45.

Bennett, A.F. 2002. *Inverse modeling in the ocean and atmosphere*. Cambridge, UK: Cambridge University Press.

Bertino, L., Evensen, G., & Wackernagel, H. 2003. Sequential data techniques in oceanography. *International Statistical Review*, **71**, 223–241.

Burgers, G., van Leeuwen, P. G., & Evensen, G. 1998. Analysis scheme in the Ensemble Kalman Filter. *Monthly Weather Review*, **126**.

Calvert, R. 2005. 4D Technology: where are we, and where are we going? *Geophysical Prospecting*, **53**, 161–171.

Chen, Y., & Oliver, D. S. 2010. Cross-covariances and localization for EnKF in multiphase flow data assimilation. *Computational Geosciences*, **14**, 579–601.

Chen, Y., & Oliver, D.S. 2009. Ensemble-based closed-loop opyimization applied to the Brugge Field. *SPE Reservoir Evaluation & Engineering (SPE-118926)*.

Chen, Y., Oliver, D. S., & Zhang, D. 2009. Data assimilation for nonlinear problems by ensemble Kalman filter with reparameterization. *Journal of Petroleum Geosciences and Engineering*, **66**, 1–14.

Cohn, S. E. 1997. An introduction to estimation theory. *Journal of the Meteorological Society of Japan*, **75**.

Courtier, P., & Talagrand, O. 1987. Variational assimilation of meteorological observations with the adjoint vorticity equation. II: Numerical Results. *Quarterly Journal of the Royal Meteorological Society*, **113**, 1329–1347.

Courtier, P., Anderson, E., Heckley, W., Pailleux, J., Vasilijevic, D., Hamrud, M., Hollingsworth, A., & Rabier, F. 1998. The ECMWF implementation of three-dimensional variational assimilation (3D-VAR). Part I, formulation. *Quarterly Journal of the Royal Meteorological Society*, **124**, 1783–1807.

Dadashpour, M., J., Kleppe, & Landrø, M. 2007. Porosity and Permeability Estimation by Gradient-Based History Matching using Time- Lapse Seismic Data. 15^{th} *SPE Middle East Oil and Gas Show and Conference (SPE 104519).*

Dake, L.P. 1978. *Fundamentals of Reservoir Engineering.* Elsevier.

Datta-Gupta, A., & King, M. J. 2007. *Streamline simulation, Theory and practice, SPE TextbookSeries Vol. 11.* SPE.

de Waal, H., & Calvert, R. 2003. Overview of global 4D seismic implementation strategy. *Petroleum Geosciences*, **9**, 1–6.

de Wit, A.J.W., & van Diepen, C.A. 2007. Crop model data assimilation with the ensemble Kalman filter for improving regional crop yield forecasts. *Agricultural and Forest Meteorology*, **146**.

Devegowda, D., Arroyo-Negrete, A., Datta-Gupta, A., & Douma, S. G. 2007. Efficient and robust reservoir model updating using ensemble Kalman filter. *SPE reservoir simulation symposium (SPE 106144).*

Dong, Y., & Oliver, D. S. 2003. Quantitative use of 4D seismic data for reservoir description. *SPE Reservoir Evaluation & Engineering (SPE-84571).*

Dong, Y., Gu, Y., & Oliver, D. S. 2006. Sequential assimilation of 4D seismic data for reservoir description using ensemble Kalman filter. *Journal of Petroleum Geosciences and Engineering*, **53**, 83–99.

Doucet, A., de Freitas, N., & Gordon, N. 2001. Sequential Monte Carlo methods in practice.

Dovera, L., & Della Rossa, E. 2010. Multimodal ensemble Kalman filtering using Gaussian mixture models. *Computational Geosciences*, **15**, 307–323.

Dræge, A., Jakobsen, M., & Johansen, T. A. 2006. Rock physics modelling of shale diagenesis. *Petroleum Geoscience*, **12**, 1–49.

Dvorkin, J., & Nur, A. 1996. Elasticity of high porosity sandstones: Theory for two North Sea datasets. *Geophysics*, **61**, 1363–1370.

Eigbe, U., Beck, M. B., Wheather, H. S., & Hirano, F. 1998. Kalman filtering in groundwater glow modeling: problems and prospects. *Stochastic Hydrology and Hydraulics*, **12**, 15–32.

Emerick, A., & Reynolds, A. 2010. Combining sensitivities and prior information for covariance localization in the ensemble Kalman filter for petroleum reservoir applications. *Computational Geosciences*, **15**, 251–269.

Emerick, A., & Reynolds, A. C. 2011. History matching a field case using the ensemble Kalmn filter with covariance localization. *SPE Reservoir Evaluation & Engineering*, **14**, 423–432.

Evensen, G. 1994. Sequential data assimilation with a nonlinear quasigeostrophic model using Monte Carlo methods to do forecast error statistics. *Journal of Geophysical research*, **99**, 10143–10162.

Evensen, G. 2004. Sampling strategies and square root analysis schemes for the EnKF. *Ocean Dynamics*, **54**, 539–560.

Evensen, G. 2009. Data assimilation - The ensemble Kalman filter.

Evensen, G., & van Leeuwen, P. J. 2000. An ensemble Kalman smoother for nonlinear dynamics. *Monthly Weather Review*, **128**, 1852–1867.

Evensen, G., Hove, J., Meisingset, H. C., Reiso, E., Seim, K. S., & Espelid, S. O. 2007. Using the EnKF for Assisted History matching of a North Sea reservoir. *SPE reservoir simulation symposium (SPE 106184)*.

Fagervik, K., Lygren, M., Valen, T.S., Hetlelid, A., Berge, G., Dahl, G.V., Sonneland, L., Lie, H. E., & Magnus, I. 2001. A method for performing history matching of reservoir flow models using 4D seismic. *69th SEG International Exposition and Annual Meeting, Expanded Abstract*, 1636–1639.

Fahimuddin, A., Aanonsen, S., & Skjervheim, J. A. 2011. Ensemble based 4D seismic history matching- Integration of different levels and types of seismic data. *72th EAGE Conference & Exhibition incorporating SPE EUROPEC, Expanded Abstracts (SPE 131453)*.

Ferris, J.G., Knowles, D. B., & Stallman, R. W. 1962. Theory of aquifer tests. *US Geological Water Supply Paper*, **1536**.

Fertig, E. J., Hunt, B. R., Ott, E., & Szunyogh, I. 2007. Assimilating non-local observations with a local ensemble Kalman filter. *Tellus*, **59**.

Foster, D. G. 2007. The BP 4-D story: Experience over the last 10 years and current trends. *International Petroleum Technology Conference (IPTC-11757)*.

Furrer, R., & Bengtsson, T. 2007. Estimation of high-dimensional prior and posterior covariance matrices in Kalman filter variants. *Journal of Multivariate Analysis*, **98**, 227–255.

Gabriels, P. W., Horvei, N. A., Koster, J. K., Onstein, A., Geo, A., & R., Staples. 1999. Time-lapse seismic monitoring of the Draugen field. 18^{th} *SEG International Exposition and Annual Meeting, Expanded Abstract*, 2035–2037.

Gaspari, G., & Cohn, S. E. 1999. Construction of correlation functions in two and three dimensions. *Quarterly Journal of the Royal Meteorological Society*, **125**, 723–757.

Gassmann, F. 1951. Über die Elastizitat poroser Medien. *Vier der Natur. Gesellschaft in Zrich*, **96**, 1–23.

Ghaderi, A., & Landrø, M. 2009. Estimation of thickness and velocity changes of injected carbon dioxide layers from prestack time-lapse seismic data. *Geophysics*, **74**, 017–028.

Ghil, M. 1989. Meteorological data assimilation for oceanographers. Part I: description and theretical framework. *Dynamics Atmospheric Ocean*, **13**, 171–218.

Ghil, M., & Malanotte-Rizzoli, P. 1991. Data assimilation in meteorology and oceanography. *Advanced Geophysics*, **23**, 141–265.

Gordon, N. 1993. *Bayesian methods for tracking.* Ph.D. thesis, University of London.

Gosselin, O., van den Berg, S., & Cominelli, A. 2006. Integrated history-matching of production and 4D seismic data. *SPE Annual Technical Conference and Exhibition (SPE 71599)*.

Greaves, R. J., & Fulp, T. J. 1987. Three-Dimensional seismic monitoring of an enhanced oil recovery process. *Geophysics*, **52**, 1175–1187.

Gu, Y., & Oliver, D. S. 2005. History Matching of the PUNQ-S3 Reservoir model using the Ensemble Kalman Filter (SPE 89942). *SPE Journal*, **10**, 217–224.

Gu, Y., & Oliver, D. S. 2006. The Ensemble Kalman Filter for continuous updating of reservoir models. *Journal of Energy Resources Technology*, **128**, 79–87.

Gu, Y., & Oliver, D. S. 2007. An iterative ensemble Kalman filter for multiphase fluid flow data assimilation. *SPE Journal (SPE 108438)*, **18**(9), 438–446.

Hacker, P. J., Anderson, J. L., & Pagowski, M. 2007. Improved vertical covariance estimate for ensemble-filter assimilation of near-surface observations. *Monthly Weather Review*, **135**, 1021–1036.

Hamill, T. M., Whitaker, J. S., & Snyder, C. 2001. Distance-dependent filtering of background error covariance estimates in an ensemble Kalman filter. *Monthly Weather Review*, **129**, 2776–2790.

Hanea, R. 2005. *Bayesian methods for tracking*. Ph.D. thesis, Delft University of Technology.

Hashin, Z., & Shtrikman, S. 1963. A variational approach to the elastic behavior of multiphase materials. *Journal of the Mechanics and Physics of Solids*, **11**, 127–140.

Haverl, M., & Skjervheim, J. A. 2008. 4D seismic modeling integrated with the ensemble Kalman filter method for history matching of reservoir simulation model. 11^{th} *EAGE European Conference on the Mathematics of Oil Recovery, Expanded Abstract*.

Haverl, M. C., Aga, M., & Reiso, E. 2005. Integrated workflow for quatitative use of time-lapse seismic data in history matching: A North Sea field case. *SPE Reservoir Evaluation & Engineering (SPE-94453)*.

He, Z., Datta-Gupta, A., & Yoon, S. S. 2001. Streamline-based production data integration under changing field conditions. *SPE Annual Technical Conference & Exhibition (SPE-71333)*.

Houtekamer, P. L., & Mitchell, H. L. 1998. Data assimilation using an ensemble Kalman filter technique. *Monthly Weather Review*, **126**, 796–811.

Houtekamer, P. L., & Mitchell, H. L. 2001. A sequential ensemble Kalman filter for atmospheric data assimilation. *Monthly Weather Review*, **129**, 123–137.

Houtekamer, P. L., & Mitchell, H. L. 2005. Ensemble Kalman filtering. *Quarterly Journal of the Royal Meteorological Society*, **131**, 3269–3290.

Houtekamer, P. L., & MItchell, H. L. 2006. Ensemble Kalman filtering. *Quarterly Journal of Meteorological Society*, **131**, 3269–3289.

Hunt, B. R., Kostelich, E. J., & Szunyogh, I. 2007. Efficient data assimilation for spatiotemporal chaos: a local ensemble transform Kalman filter. *Physica*, **D230**, 112–126.

IEO. 2011. International Energy Outlook 2011, Technical Report doe/eia(2011). *Energy Information Administartion, U.S. Department of Energy*.

Jafarpour, B., & McLaughlin, D. B. 2007a. Efficient permeability parameterization with the Discrete Cosine Transform. *SPE Reservoir Simulation Symposium (SPE 106453)*.

Jafarpour, B., & McLaughlin, D. B. 2007b. History matching with an ensemble Kalman filter and Discrete Cosine parameterization. *SPE Annual Technical Conference (SPE 108761)*.

Jansen, J. D., Brouwer, D. R., Nævdal, G., & van Kruijsdijk, C. P. J. W. 2005. Closed-loop reservoir management. *First Break*, **23**, 43–48.

Jansen, J. D., Bosgra, O. H., & Van den Hof, P. M. J. 2008. Model-Based Control of Multiphase Flow in Subsurface Oil Reservoirs. *Journal of Process Control*, **18**(9), 846–855.

Jansen, J. D., Douma, S. G., Brouwer, D. R., Van den Hof, P. M. J., Bosgra, H., & Heemink, A. W. 2009a. Closed-loop reservoir management. *Reservoir Simulation Symposium (SPE 119098)*.

Jansen, J. D., Van Doren, J. F. M., Fyrozjaee, M. H., & Yortsos, Y. C. 2009b. Front controllability in two-phase porous media flow. *Pages 203–219 of:* Van den Hof, P. M. J., Scherer, C., & Heuberger, P. S. C. (eds), *Model-Based Control: Bridging Rigorous Theory and Advanced Technology*. New York: Springer.

Jin, L., Castineira, D., Fu, S., van den Hoek, P., Pirmez, C., Fehintola, T., Tendo, F., & Olaniyan, E. 2011. 4D Seismic History Matching Using Flood Front Information. 73^{th} *EAGE Conference & Exhibition incorporating SPE EUROPEC, Expanded Abstracts*.

Kalman, R. E. 1960. A new approach to linear filtering and prediction problems. *Transactions of the ASME-Journal of Basic Engineering*, **82**.

Kepert, J. D. 2009. Covariance localization and balance in an ensemble Kalman filter. *Quarterly Journal of the Royal Meteorological Society*, **135**, 1157–1176.

Keppenne, C. L., & Rienecker, M. M. 2002. Initial testing of a massively parallel ensemble Kalman filter with the Poseidon isopycnal ocean circulation model. *Monthly Weather Review*, **130**, 2951–2965.

Keppenne, C. L., & Rienecker, M.M. 2003. Assimilation of temperature into an isopycnal ocean general circulation model using a parallel ensemble kalman filter. *Journal of Marine System*, **40**.

Kotecha, J. H., & Diurić, P. M. 2003. Gaussian sum particle filtering. *IEEE*, **51**, 2602–2612.

Kretz, V., Valles, B., & Sonneland, L. 2004. Fluid Front History Matching Using 4D Seismic and Streamline Simulation. *SPE Annual Technical Conference and Exhibition (SPE 90136)*.

Landrø, M. 1999. Discrimination between pressure and fluid saturation changes from time-lapse seismic data. *69th SEG International Exposition and Annual Meeting, Expanded Abstract*, 1651–1654.

Landrø, M. 2001. Discrimination between pressure and fluid saturation changes from time-lapse seismic data. *Geophysics*, **66**, 836–844.

Landrø, M. 2002. Uncertainty in quantitative time-lapse seismic analysis. *Geophysical Prospecting*, **50**, 527–538.

Landrø, M., & Stammeijer, J. 2004. Quantitative estimation of compaction and velocity changes using 4D impedance and traveltime changes. *Geophysics*, **69**, 949–957.

Landrø, M., Digranes, P., & Strønen. 2001. Mapping reservoir pressure and saturation changes using seimic methods- possibilities and limitations. *First Break*, **19**, 671–577.

Lawson, W. G., & Hansen, J. A. 2002. Implications of stochastic and deterministic filters as ensemble based data assimilation methods in varying regimes of error growth. *Monthly Weather Review*, **132**, 1966–1981.

Le Dimet, F. X., & Talagrand, O. 1985. Variational algorithms for analysis and assimilation of meteorological observations: theoretical aspects. *Tellus*, **38**.

Leeuwenburgh, O. 2007. Validation of of an EnKF system for OGCM initialization assimilating temperature, salinity and surface height measurements. *Monthly Weather Review*, **135**.

Leeuwenburgh, O., Evensen, G., & Bertino, L. 2005. The impact of Ensemble filter definition on the assimilation of temperature profiles in the Tropical Pacific. *Quarterly Journal of the Royal Meteorological Society*, **131**, 3291–3300.

Leeuwenburgh, O., Brouwer, J. H., & Trani, M. 2011. Ensemble-based conditioning of reservoir models to seismic data. *Computational Geosciences*, **15**, 359–378.

Lefebvre, T., Bruynickx, H., & De Schutter, J. 2004. Kalman filters for non linear systems: a comparison of performance. *International Journal of Control*, **77**, 639–653.

Leguijt, J. 2001. A promising approach to subsurface information integration. *63rd EAGE Conference & Exhibition*.

Leguijt, J. 2009. Seismically constrained probabilistic reservoir modeling. *The Leading Edge*, **28**, 1478–1484.

Lewis, J. M., & Derber, J. C. 1985. The use of adjoint equations to solve a variational adjustment problem with convective constraints. *Tellus*, **37**.

Li, G., & Reynolds, A. C. 2009. Iterative Ensemble Kalman filters for data assimilation. *SPE Journal (SPE 109808)*, **14**.

Lorenc, A. A. 1981. A global three-dimensional multivariate statistical interpolation scheme. *Monthly Weather Review*, **109**, 701–721.

Lorenc, A. C. 2003. The potential of the Ensemble Kalman filter for NWP-a comparison with 4D var. *Quarterly Journal of the Royal Meteorological Society*, **129**, 3183–3203.

Lorentzen, R. J., & Naevdal, G. 2011. An iterative ensemble Kalman filter. *IEEE Transactions on Automatic Control*, **56**, 1990–1995.

Lorentzen, R. J., Fjelde, K. K., Frøyen, J., Lage, A.C. V. M., & Naevdal, G. 2001. Underbalanced and low-Head Drilling Operations: Real Time data interpretation and decision support (SPE 71384). *SPE Annual Technical Conference and Exhibition.*

Lorentzen, R. J., Naevdal, G., Valles, B., Berge, A., & Grimstad, A.-A. 2011. Analysis of the ensemble Kalman filter for the estimation of permeability and porosity in reservoir models. *SPE Annual Technical Conference & Exhibition (SPE 96375).*

Maybeck, P. S. 1979. *Stochastic models,estimation and control volume 1.* New York: Mathematics in Science and Engineering, Academic Press.

Meadows, M. 2001. Enhancements to Landro's method for separating time-lapse pressure and saturation changes. *71st SEG International Exposition and Annual Meeting, Expanded Abstract*, 1652–1655.

Mindlin, R. D. 1949. Compliance of elastic bodies in contact. *Journal of Applied Mechanics*, **16**, 259–268.

Moore, A. M. 1991. Data assimilation in a quasi-geostrophic open-ocean model of the Gulf-Stream region using the adjoint model. *Journal of Physical Oceanography*, **21**, 398–427.

Mysrseth, I., Saetrom, J., & Omre, H. 2012. Resampling the ensemble Kalman filter. *Submitted to Geophysics.*

Nævdal, G., Mannseth, T., & Vefring, E. 2002. Instrumented wells and near-well reservoir monitoring through ensemble Kalman filter. 8^{th} *EAGE European Conference on the Mathematics of Oil Recovery, Expanded Abstract.*

Naevdal, G., Johnsen, L. M., Aanonsen, S. I., & Vefring, E. H. 2005. Reservoir monitoring and continuous model updating using Ensemble Kalman Filter (SPE 84372). *SPE Journal*, **10**, 66–74.

Nævdal, G., Brouwer, D. R., & Jansen, J. D. 2006. Waterflooding using closed-loop control. *Computational Geosciences*, **10**, 66–74.

Oliver, D. S., & Chen, Y. 2009. Improved initial sampling for the ensemble Kalman filter. *Computational Geosciences*, **13**, 13–26.

Peters, E. 2011. Performance of the ensemble Kalman filter outside of existing wells for a channelized reservoir. *Computational Geosciences*.

Peters, E., Arts, R. J., Brouwer, G. K., Geel, C. R., Cullick, S., Lorentzen, R. J., Chen, Y., Dunlop, K. N. B., Vossepoel, F. C., Xu, R., Sarma, P., Alhutali, A. H., & Reynolds, A. C. 2009. Results Of The Brugge Benchmark Study For Flooding Optimisation And History Matching. *SPE Reservoir Evaluation & Engineering (SPE paper 119094)*, **13**, 391.

Phale, H. A., & Oliver, D. S. 2011. Data Assimilation Using the Constrained Ensemble Kalman Filter. *SPE Journal (SPE 108438)*, **16**(2), 331–342. DOI: 10.2118/125101-PA.

Portella, R.C.M., & Emerick, A.A. 2005. Use of quantitative 4D-seismic data in automatic history matching. *SPE Reservoir Evaluation & Engineering (SPE-94650)*.

Reynolds, A., Zafari, M., & Li, G. 2006. Iterative Forms of the Ensemble Kalman Filter. *In: 10th European Conference on the Mathematics of Oil Recovery*.

Roggero, F., Ding, D.Y., Berthet, P., Lerat, O., Cap, J., & Schreiber, P.E. 2007. Matching of production history and 4D seismic data - Application to the Girassol field, offshore Angola. *SPE Reservoir Evaluation & Engineering (SPE-109929)*.

Rojas, E. 2008. Vp-Vs sensitivity to pressure, fluid, and lithology changes in tight gas sandstones. *First Break*, **26**, 83–86.

Røste, T., Stovas, A., & Landrø, M. 2006. Estimation of layer thickness and velocity changes using 4D prestack seismic data. *Geophysics*, **71**, S219–S234.

Sakov, P., & Bertino, L. 2011. Relation between two common localization methods for the EnKF. *Computational Geosciences*, **15**, 225–237.

Sakov, P., & Oke, P. R. 2008. A deterministic formulation of the Ensemble Kalman Filter: an alternative to ensemble square-root filters. *Tellus*, **60A**, 361–371.

Sakov, P., Evensen, G., & Bertino, L. 2010. Asynchronus data assimilation with the EnKF. *Tellus*, **62**, 24–29.

Sarma, P., Durlofsky, L. J., Aziz, K., & Chen, W. H. 2006. Efficient real-time reservoir management using adjoint-based optimal control and model updating. *Computational Geosciences*, **10**(1), 3–36.

Schroter, J., Seiler, U., & Wenzel, M. 1993. Variational assimilation of Geosat data into an eddy-resolving model of the Gulf Stream area. *Journal of Physical Oceanography*, **23**, 925–953.

Schulze-Riegert, R., Krosche, M., & Pajonk, O. 2009. Hybrid optimization coupling EnKF and evolutionary algorithm for history matching: a case example. *SPE EUROPEC/EAGE Annual Conference (SPE 121965)*.

Sheinbaum, J., & Anderson, D. L. T. 1990. Variational assimilation of XBT data. *Journal of Physical Oceanography*, **20**, 672–688.

Skjervheim, J. A., & Ruud, B. O. 2006. Combined inversion of 4D seismic waveform data and production data using ensemble Kalman filter. *SEG International Exposition and Annual Meeting, Expanded Abstract*, 1776–1779.

Skjervheim, J. A., Aanonsen, S.I., Ruud, B. O., Evensen, G., & Johansen, T. A. 2006. Using the ensemble Kalman filter with 4D data to estimate properties and lithology of reservoir rocks. 10^{th} *EAGE European Conference on the Mathematics of Oil Recovery, Expanded Abstract*, **A028**.

Skjervheim, J. A., Evensen, G., Aanonsen, S.I., Ruud, B. O., & Johansen, T. A. 2007. Incorporating 4D seismic data in reservoir simulation models using ensemble Kalman filter. *SPE Journal (SPE 95789)*.

Smith, G., & Gidlow, P. M. 1987. Weighted stacking for rock property estimation and detection of gas. *Geophysical Prospecting*, **25**, 993–1014.

Stenerud, V. R. 2007. *Multiscale-streamline inversion for high-resolution reservoir models*. Ph.D. thesis, Norwegian University of Science and Technology.

Stephen, K. D., & MacBeth, C. 2006. Reducing reservoir prediction uncertainty using seismic history match. *SPE Europec/ EAGE Annual Conference and Exhibition (SPE 100295)*.

Stordal, A. S., Karisen, H. A., Nævdal, G., Skaug, H. J., & Vallés, B. 2011. Bridging the Ensemble Kalman Filter and Particle filters: the adaptive Gaussian mixture field. *Computational Geosciences*, **15**, 293–305.

Talagrand, O., & Courtier, P. 1987. Variational assimilation of meteorological observations with the adjoint vorticity equation. I: Theory. *Quarterly Journal of the Royal Meteorological Society*, **113**, 1311–1328.

Tarantola, A. 2005. *Inverse problem theory and methods for model parameter estimation.* SIAM, Philadelphia.

Tavassoli, Z., Carter, J. N., & King, P. R. 2004. Errors in History Matching. *SPE Journal (SPE 86883-PA)*, **9**(3), 352–361.

Thacker, W. C., & Long, R. B. 1988. Fitting dynamics to data. *Journal of Geophysical Research*, **93**, 1227–1240.

Thiele, M. R., Fenwick, D. H., & Batycky, R.P. 2007. Streamline-assisted history matching. *9th International Forum on Reservoir Simulation, December 9th-13th.*

Thiele, M. R., Batycky, R. P., & Fenwick, D. H. 2010. Journal of Petroleum Technology. *Monthly Weather Review*, **62**, 64–70.

Thulin, K., Li, G., Aanonsen, S. I., & Reynolds, A. C. 2007. Estimation of initiasl fluid contacts by assimilation of production data with EnKF. *SPE Annual Technical Conference (SPE 109975).*

Thulin, K., Naevdal, G., Skaug, H. J., & Aanonsen, S. I. 2011. Quantifying Monte Carlo uncertainty in the Ensemble Kalman Filter. *SPE Journal*, **16**, 172–182.

Tippett, M., Anderson, J. L., Bishop, C. H., Hamill, T. M., & Whitaker, J. S. 2003. Ensemble square-root filters. *Monthly Weather Review*, **131**, 1485–1490.

Trani, M., Arts, R., Leeuwenburgh, O., Brouwer, J., & Douma, S. 2009a. The importance of localization for the assimilation of 4D seismic using the EnKF. 79^{th} *SEG International Exposition and Annual Meeting, Expanded Abstract*, 3835–3889.

Trani, M., Arts, R., Leeuwenburgh, O., Brouwer, J., & Douma, S. 2009b. The value of the Streamline-based localization in the assimilation of 4D seismic data with the EnKF. 71^{st} *EAGE Conference & Exhibition incorporating SPE EUROPEC, Expanded Abstracts.*

Trani, M., Arts, R. J., O., Leeuwenburgh, & H., Brouwer J. 2011. Estimation of changes in saturation and pressure from 4D seismic AVO and time-shift analysis. *Geophysics*, **76**, C1–C17.

Trani, M., Arts, R. J., & O., Leeuwenburgh. 2012. Seismic History Matching of fluid fronts using the Ensemble Kalman Filter. *SPE Journal (accepted for publication,SPE-163043-MS).*

Tura, A., & Lumley, D. E. 1999. Estimating pressure and saturation changes from time-lapse AVO data. *69th SEG International Exposition and Annual Meeting, Expanded Abstract*, 1655–1658.

Tura, A., Barker, T., Cattermole, P., Collins, C., Davis, J., Hatchell, P., Koster, K., Schutjens, P., & Wills, P. 2005. Monitoring primary depletion reservoirs using amplitudes and time-shifts from high repeat seismic surveys. *The Leading Edge*, **24**, 1214–1221.

Vallés, B., & Naevdal, G. 2009. Revisisting Brugge case study using a hierarchical ensemble Kalman filter. *International Petroleum Technology Conference.*

Van den Hof, P. M. J., Van Doren, J. F. M., & Douma, S. G. 2009. Identification of parameters in large scale physical model structures, for the purpose of model-based operations. *Pages 125–146 of:* Van den Hof, P. M. J., Scherer, C., & Heuberger, P. S. C. (eds), *Model-Based Control: Bridging Rigorous Theory and Advanced Technology.* New York: Springer.

van Ditzhuijzen, R., Oldenziel, T., & Van Kruijsdijk, C.P.J.W. 2001. Geological parameterization of a reservoir model for history matching incorporating time-lapse seismic based on a case study of the Stafjord field. *SPE Reservoir Evaluation & Engineering (SPE-71318).*

Wang, X., Bishop, C. H., & Julier, S. J. 2004. Which is better, an ensemble of positive-negative pairs or a centered spherical simplex ensemble? *Monthly Weather Review*, **132**, 1590–1605.

Wang, Y., Li, G., & Reynolds, A. C. 2010. Estimations of fluuid contacts and relative permeability curves by history matching using iterative ensemble-Kalman smoothers. *SPE Journal*, **15**, 509–525.

Wen, X. H., & Chen, W. H. 2006. Real-time reservoir model updating using ensemble Kalman filter with confirming option. *SPE Journal (SPE 92991)*, **11**, 431–442.

Wen, X. H., & Chen, W. H. 2007. Some practical issues on real-time reservoir model updating using ensemble Kalman filter. *SPE Journal (SPE 111571)*, **12**, 156–166.

Whitaker, J. S., & Hamill, T. M. 2002. Ensemble data assimilation without perturbed observations. *Monthly Weather Review*, **130**, 1913–1924.

Whitcombe, D. N. 2002. Elastic impedance normalization. *Geophysics*, **67**, 60–62.

Williams, M. A., Keating, J. F., & Barghouty, M. F. 1998. The stratigraphic method: a structured approach to history matching complex simulation models. *SPE Reservoir Evaluation Engineering*, **1**, 169–176.

Wu, Z., & Datta-Gupta, A. 2002. Rapid history matching using a generalized travel-time inversion method. *SPE Journal (SPE-78359)*, **7**, 113–222.

Wunsch, C. 1996. *The ocean circulation inverse problem*. Cambridge University Press.

Zafari, M., & Reynolds, A. C. 2007. Assessing the uncertainty in reservoir description and performance predictions with the Ensemble Kalman Filter. *SPE Journal*, **12**, 382–391.

Zhang, Y., & Oliver, D. S. 2011a. Evaluation and error analysis: Kalman gain regularization versus covariance regularization. *Computational Geosciences*.

Zhang, Y., & Oliver, D. S. 2011b. Improving the ensemble estimate of the Kalman gain by bootstrap-sampling. *Mathematical Geosciences*, **42**, 327–345.

Zhao, Y., Reynolds, A. C., & Li, G. 2008. Generating facies maps by assimilating production data and seismic data with the ensemble Kalman filter. *SPE Improved Oil Recovery Symposium (SPE 113990)*.

Zupanski, M. 2005. Maximum likelihood ensemble filter. *Monthly Weather Review*, **133**, 1710–1726.

Summary

THE world energy demand still increases every year. As a consequence, the demand for fossil fuels, by far the first energy source, is increasing, while easily accessible fossil fuel resources are decreasing. This has stimulated research and development to the optimization of hydrocarbon recovery from existing reservoirs over the last decade. Waterflooding for enhanced oil recovery is one approach to increase the recovery of an oil reservoir. In this thesis the monitoring of waterflooding using time lapse seismic data in combination with production data is used to improve the representative flow models of the reservoir. Such models are then used to optimize production strategies.

When constraining a reservoir model to observations, the measurement uncertainty plays a key role. The first part of this thesis is dedicated to developing an inversion methodology leading to more accurate estimates of changes in saturation and pore pressure induced by waterflooding from 4D seismic data.
Waterflooding processes induce time-lapse changes in reservoir fluid saturation and in pore pressure. These are reflected in 4D variations of seismic attributes like changes in amplitudes and time-shifts.
The improvement of the proposed 4D seismic inversion method resides in a more correct, and possibly unbiased, estimate of time-lapse changes in saturation and pore pressure. Existing methods often suffer from bias and leakage between the different estimated parameters. By making use of different combinations of time-lapse seismic attributes based on four equations: two expressing changes in pre-stack AVO attributes (zero-offset and gradient reflectivities), and two expressing post-stack time-shifts of compressional and shear waves as functions of production induced changes in fluid properties, the estimates can be considerably improved. The impact of using different combinations of these equations is tested on a synthetic, though realistic 3D model, where seismic data have been simulated at various steps during the 30 years lifetime of the waterflooded reservoir.

Results show that the inversion accuracy increases if higher order terms in the description of the P-wave gradient reflectivity are not neglected, or if, in case S-wave data are available, the S-wave time-shift equation replaces the equation related to the P-wave gradient reflectivity. As in all inversion methods, the influence of prior porosity estimates remains very high and results improve considerably, in case lateral variations of porosity are properly taken into account. The effect of noise on the inversion results is also investigated, with the conclusion that the method seems to be quite robust to random noise, while the introduction of systematic noise decreases the inversion accuracy more severely.

The second part of this thesis is dedicated to the investigation of the possibilities to obtain an accurate model characterization, particularly in terms of flow, through the assimilation of seismic measurements with the Ensemble Kalman Filter.
The mathematical process which identifies the parameter values that minimize a cost-function representing the mismatch between modeled and observed data is called Data Assimilation (or History Matching). In Data Assimilation, parameter estimations for the entire reservoir model, are often based only on the information related to sparsely distributed production data. It is obvious that in such a case the number of observations is much smaller than the number of parameters to estimate, making history matching a strongly ill-posed problem. The additional information acquired from (time-lapse) seismic data can be utilized to narrow the solution space down when minimizing the misfit between gathered measurements and their forecasts from numerical models.
Although in literature numerous data assimilation methods have been presented, in this thesis the Ensemble Kalman Filter has been chosen for several reasons. Firstly, the method is computationally feasible for large systems and is relatively simple to implement making use of existing simulators. Secondly, it presents a flexible treatment of any kind and number of data or uncertain parameters. Thirdly, this method has a large and active research community, and a rigorous theoretical basis.
This thesis proposes two innovative approaches to assimilate seismic measurements with the Ensemble Kalman Filter.
The first approach concerns the assimilation of time-lapse changes in fluid saturation and pore pressure available for every reservoir gridblock. This method builds directly on the results of the first part of this thesis. In this case the number of observations to assimilate can be very high, causing the problem of 'filter divergence'. Filter divergence is a consequence of an excess-

ive reduction of ensemble parameter covariance. The most effective method to circumvent this problem is Covariance regularization through Localization. This approach consists of multiplying the ensemble covariances element-wise by a local support matrix, resulting in a localized covariance estimate.
For a correct application, localization requires the knowledge of the real covariance between measurements and states/parameters to update. Through a 2D synthetic study rules of thumb for the definition of adequate localization functions have been determined. Afterwards these rules have been successfully applied on a 3D reservoir.
The second approach of seismic data assimilation is based on the assimilation of fluid front arrival times. The major advantage of the method is, that no full inversion of seismic data to saturations for each grid block is required. The focus is only on the fronts, where changes in time lapse seismic response can be observed. In this case saturation data, impedance maps, or even simple amplitude change maps can be assimilated as waterfront arrival times. This approach enables a very large reduction in number of data while retaining the essential information content. Furthermore, it offers a more linear sensitivity to reservoir properties and a more Gaussian distribution of simulated measurements than using saturation data. This tends to improve the functioning of the EnKF, which represents a multi-model history match that incorporates and retains geological information formulated in terms of two-point geostatistics. This method has also been successfully applied on a slightly modified version of the benchmark Brugge field, a synthetic study reflecting to a great extent the complexity of a real field.

Samenvatting

De wereldwijde vraag naar energie stijgt nog steeds jaarlijks. Hierdoor stijgt ook de vraag naar fossiele brandstoffen, nog steeds de belangrijkste energiebron, terwijl tegelijkertijd de voorraden gemakkelijk winbare olie afnemen. Dit heeft het afgelopen decennium onderzoek en ontwikkeling naar het optimaliseren van olie- en gaswinning uit bestaande velden enorm gestimuleerd. Een bekende manier om meer olie uit reservoirs te halen is middels waterinjectie. Dit proces kan in kaart gebracht en gevolgd worden door in de tijd herhaalde seismische metingen, ook vaak 4D seismiek genoemd. In dit proefschrift is het monitoren met 4D seismiek in combinatie met productie data gebruikt om de representativiteit van stromingsmodellen van het reservoir te verbeteren. Deze modellen worden vervolgens dan weer gebruikt om productie strategieën te optimaliseren.

Voor het beperken van het aantal mogelijke oplossingen van een reservoir model met behulp van observaties speelt de onzekerheid op de metingen een cruciale rol. Het eerste deel van dit proefschrift is dan ook gericht op het ontwikkelen van een inversie methode van 4D seismische gegevens, die leidt tot een nauwkeuriger schatting van veranderingen in druk en saturatie ten gevolge van waterinjectie in een oliereservoir. Waterinjectie zorgt voor ruimtelijke veranderingen in de tijd van reservoir vloeistof saturatie en druk. Deze veranderingen kunnen opgepikt worden als 4D veranderingen in seismische attributen, zoals bijvoorbeeld veranderingen in signaalsterkte of tijdsverschuivingen in looptijden.
De verbetering van de voorgestelde 4D seismische inversie methode leidt vooral tot een meer correcte, voor zover mogelijk zonder bias, schatting van in de tijd veranderende saturatie en druk. Bestaande methodes hebben vaak als tekortkomingen de introductie van een bias en het "lekken" van de ene naar de andere geschatte parameter. Door gebruik te maken van verschillende combinaties van seismische attributen kunnen schattingen aanzienlijk verbeterd worden. De basis hiervoor zijn vier (seismische) vergelijkingen, waarvan twee

de veranderingen in "pre-stack" AVO (de zero-offset en de gradient reflectiviteit) beschrijven, en twee de "post-stack" looptijdvertragingen van de druk- en schuifgolven, als functie van de door productie geïnduceerde veranderingen in de vloeistofeigenschappen. De gevolgen van het gebruik van verschillende combinaties van deze vergelijkingen zijn getest op een synthetisch, doch zeer realistisch 3D model, waarbij op een aantal tijdstappen eveneens seismische data zijn gesimuleerd gedurende de dertig jaar productietijd van het reservoir.
Resultaten laten zien hoe de nauwkeurigheid van de inversieresultaten toeneemt, wanneer hogere orde termen in de beschrijving van de drukgolf gradient reflectiviteit meegenomen worden. Hetzelfde gebeurt, wanneer in geval van de beschikbaarheid van schuifgolfdata, de schuifgolf looptijdveranderingsvergelijking gebruikt wordt in plaats van de drukgolf gradient reflectiviteit. Zoals geldig voor alle inversie methodes, blijft ook hier de invloed van de a-priori porositeitsschatting erg groot, waarbij resultaten aanzienlijk verbeteren wanneer ruimtelijke variaties van de porositeit netjes meegenomen worden. Tevens zijn de effecten van ruis op de inversieresultaten onderzocht. De belangrijkste conclusies hiervan zijn, dat de methode robuust is voor random ruis, maar dat systematische ruis het resultaat behoorlijk kan verslechteren.

Het tweede deel van dit proefschrift is gewijd aan onderzoek naar de mogelijkheden om een goed reservoir model te schatten, geschikt voor vloeistofstroming, door seismische metingen te assimileren met het Ensemble Kalman Filter. Het mathematische proces om parameters te schatten, die het verschil tussen data en model minimaliseren, wordt data assimilatie of history matching genoemd. In data assimilatie is het niet ongebruikelijk, dat parameters voor een heel reservoir model geschat worden slechts gebaseerd op zeer beperkte ruimtelijke informatie zoals productiegegevens. In een dergelijk geval is het aantal observaties dus veel kleiner dan het aantal te schatten parameters. Dit maakt history matching tot een ondergedetermineerd systeem. De additionele informatie afkomstig van in de tijd herhaalde seismische data kan dan ook gebruikt worden om de oplossingsruimte te verkleinen door het verschil tussen metingen en de voorspelde metingen uit de numerieke modellen te minimaliseren.
Hoewel in de literatuur een scala aan data assimilatie methodes gevonden kan worden, is in dit proefschrift duidelijk voor het Ensemble Kalman Filter gekozen. In de eerste plaats is dit gedaan vanwege de geschiktheid van deze methode om grote systemen door te rekenen en de relatief gemakkelijke implementatie, waarbij geen aanpassing van bestaande simulatoren vereist is. In de tweede plaats is deze methode uiterst flexibel, waarbij verschillende

types gegevens in willekeurige aantallen en ieder met een eigen onzekerheid meegenomen kunnen worden. Tenslotte is de theoretische basis van deze methode goed onderbouwd en is er een zeer actieve onderzoeks-gemeenschap actief.
Dit proefschrift introduceert twee nieuwe benaderingen om seismische gegevens te assimileren met het Ensemble Kalman Filter. De eerste aanpak gaat uit van assimilatie van in de tijd veranderende druk en saturatie per reservoir gridblok. Deze methode is een rechtstreeks en logisch vervolg op de resultaten uit het eerste deel van dit proefschrift. Voor deze methode kan het aantal observaties, dat geassimileerd moet worden, erg groot worden en dit kan leiden tot zogenaamde filter divergentie. Dit wordt veroorzaakt door een excessieve reductie van de parameter covariantie in een ensemble. Een effectieve manier om dit probleem te omzeilen is door covariantie regularisatie met behulp van lokalisatie. Deze aanpak bestaat uit een vermenigvuldiging van ieder elementje van de ensemble covarianties met een lokale ondersteuningsmatrix, resulterend in een lokale covariantie schatting. Voor een correcte toepassing van lokalisatie is echter kennis van de echte covariantie tussen metingen en de bij te werken toestanden/parameters noodzakelijk. Middels een 2D synthetische studie zijn vuistregels afgeleid voor de definitie van geschikte lokalisatie functies, die vervolgens ook op een 3D reservoir toegepast kunnen worden. Dit laatste is succesvol uitgeprobeerd.

De tweede voorgestelde aanpak van seismische data assimilatie is gebaseerd op het assimileren van vloeistoffront aankomsttijden. Het grote voordeel van deze methode is, dat geen volledige inversie van seismische data naar saturatie per gridblok nodig is. De nadruk ligt echt op de frontinformatie, waar veranderingen in seismische signalen als functie van de tijd waargenomen kunnen worden. Dit betekent in praktijk, dat ofwel saturatie gegevens, ofwel impedantie data, ofwel simpele amplitude veranderingen of zelfs andere seismische attributen getransformeerd kunnen worden naar vloeistoffront aankomsttijd informatie en vervolgens geassimileerd kunnen worden. Deze aanpak leidt tot een enorme reductie van de hoeveelheid gegevens, maar waarbij de essentie bewaard blijft. Verder vertoont deze methode een meer lineaire gevoeligheid ten opzichte van reservoir eigenschappen en volgt de verdeling van de gesimuleerde metingen meer een Gauss verdeling dan in het geval van saturatie data rechtstreeks. Dit leidt tot een betere werking van het EnKF, dat gezien kan worden als een multi-model history matching procedure waarin geologische informatie geformuleerd is in termen van tweepunts geostatistiek. De aanpak is succesvol toegepast op een licht gemodificeerde versie van het benchmark Brugge veld, een synthetische

studie met de ingebouwde complexiteit van een echt veld.

Acknowledgments

THIS research was carried out within the context of the ISAPP Knowledge Centre. ISAPP (Integrated Systems Approach to Petroleum Production) is a joint project of TNO, Shell International Exploration and Production, and Delft University of Technology. A special thank is for Shell International Exploration and Production for allowing the use of MoReS to perform reservoir simulations.

The years spent on this thesis were quite intense; there are so many people I would like to acknowledge for their contribution, either to my academic achievements or to my personal development. I hope I will be able to mention them all with in this page, without forgetting anyone.
First, I would like to thank my supervisor Prof. Dr. Ir. Rob Arts for believing in me, for believing that a geologist with a very weak mathematical background could succeed in completing a PhD research like the one I did. Also, I would like to thank Rob for his constant support, numerous advices both on technical and non-technical issues, and last, but not least, for all the lifts to TNO-although a bit too early in the mornings...
Another special thank is to Dr Olwijn Leeuwenburgh, my daily supervisor in Reservoir Enginering. Thank you Olwijn for dedicating so much time on detailed explanations about the mathematics of the EnKF. That time was indeed an investment, and it paid off. Also, I wanna thank Olwijn for showing me how to surf: it was a pretty unique experience and I will never forget the cold blue water of Cascais.
Another immense thank is to all of my former colleagues at TNO, who were always available to help me and share with me a bit of their experiences and skills. In particular, I want to thank Remus Hanea for his initial input on the EnKF and various advices on publications/thesis structure. Also I want to thank Remus for the nice job he did as being my paranimph. Then, Dr Lies Peters for her numerous small helps in running MoReS. Also, I want to thank Gulnazira Kunakhbayeva (Gulnaz) who taught me how to use the

Petrel geological modeling tool, and Dr Mei Zhang, for all showing me numerous useful tricks in Matlab, for the useful advices on job interviews skills, and for the nice chats/breaks we had in our room.

I also would like to thank Prof. M. Landrø for his feedback and inputs on my 4D seismic inversion work.
Another special thank is for all of my colleagues at TUD who were always there to help me, to support me and to have a break with me when necessary. In particular, I wanna thank Dr Jürg Hunziker for teaching me how to use Latex and Adobe Illustrator. Jurg, the complete layout of this thesis is what comes out of your teachings!
I also wanna thank other two persons for all the times they helped me/showed me tricks in Matlab. These are Dr. Christiaan Schoemaker and Dr Matgorzata Kaleta (Gosia) and Dr Ali Vakili.
I also wanna thank the CITG secretary office for the help I received in solving practical/administrative problems and in improving my Dutch language skills. *Marlijn, Lydia, Margot, ik zal altijd Nederland oefenen!*
Not to forget is Mattia for his moral support ,especially in the last months of my PhD. Also, I wanna thank all my TUD colleagues for the fun we had at the EAGE conferences in Rome, Amsterdam, Barcelona, and at the SEG in Houston.
Last, I wanna thank my current managers at TOTAL E&P UK (Pierre Bergey, Gilles Drouillon and Richard Rivenq), for being so comprehensive, and my current colleagues in GRC for all the moral support they gave me during the last months, in particular Dick, Anahita, Henk, Evren.

I dedicate the next paragraph to thank all the friends who contribute to render this Dutch experience unforgettable. The first person to thank is Alex, for our nights out and support, then Francesco, who always helped me with technology (and smartphone related issues, even during our parties!!!!), and Willem for his wonderful lasagna! Guys, I never felt alone having you there, thank you.
A special thank is to my mates in Amsterdam. Guys, although I was always busy and worried about my PhD, thank you for inviting me to take a break, and for spending with me some of the best weekends out I ever had. *Jongens, ik zal nooit m'n 29e verjardag bij Dance Valley vergeten!*
Another big "thank you" is for my Italian friends (Andrea, Fabiana, Fiorella, Flavia, Donato, Gnegna & Karo, and all the others) who even tough far away, always supported me and never let me feel alone during my stay in Holland. Guys, I will always love you, no matter where my career will bring me, I will

never forget the moments we lived together!
Last, but most important is acknowledging my family for being always ready to help me and support me in every moment and occasion. The reader would forgive me if I address them in Italian:
Grazie mamma e papa per l'educazione che mi avete dato e la cultura che ho mi avete fatto apprendere. Non riuscirei mai a dirlo a voce ma ammiro tutti gli sforzi che avete sempre fatto per assicurarvi il nostro bene. Spero di riuscire a fare altrettanto in futuro.

About the author

Mario Trani was born on July 11, 1980 in Latina, Italy. He received his secondary education between 1994 and 1999 at the 'Liceo Scientifico Statale G.B. Grassi' in Latina. From 1999 to 2005 he studied Geology at 'La Sapienza' University of Rome. The title of his MSc thesis was 'Mapping and Interpretation of Seismic Anomalies related to shallow gas in the Southern North Sea'. This MSc thesis was carried at TNO under the joint supervision of Prof. S. Lombardi and Dr B. Schroot. He graduated with honors. Hereafter he joined the Technical University of Delft as a PhD student in the ISAPP program. During his PhD project he took graduate courses at the Dutch Institute for Systems and Control (DISC) and received the DISC certificate. Since 2011 he has been working as a research reservoir engineer for the GRC-Geosciences Research Center of Total Exploration and Production UK. He is currently working, in cooperation with geologists and geophysicists, on testing history matching research prototypes and on developing in-house tools for uncertainty quantification on time-lapse changes in water and gas saturations.

List of Publications

Journal papers

Trani, M., Arts, R. J. and Leeuwenburgh O.(2012). Seismic History Matching of fluid fronts using the Ensemble Kalman Filter. *SPE Journal* (SPE-163043-PA, Accepted for publication)

Trani, M., Arts, R. J., Leeuwenburgh O. and Brouwer J. H. (2011). Estimation of changes in saturation and pressure from 4D seismic AVO and time-shift analysis. *Geophysics*, **76** (2): C1-C17.

Leeuwenburgh, O., Brouwer, J. H. and Trani, M. (2011). Ensemble-based conditioning of reservoir models to seismic data. *Computational Geosciences*, **15** (2): 359-378.

Arts, R. J. and Chadwick, R. A. and Eiken, O. and Dortland, S. and Trani, M. and van derMeer, L.G. H. (2009). Acoustic and elastic modeling of seismic time-lapse data from the Sleipner CO_2 storage operation. *Carbon dioxide sequestration in geological media- State of the Science: AAPG Studies in geology*, **59**: 391-403 .

Conference proceedings

Trani, M., Arts, R., Leeuwenburgh, O., and Brouwer, J. (2010). Sensitivity of time-lapse changes in pressure and saturation to seismic AVO and time-shift. *72nd EAGE Conference and Exhibition*, **A026**, Barcelona, Spain.

Leeuwenburgh, O., Brouwer, J., and Trani, M. (2012). Ensemble-based reservoir characterization using time-lapse seismic waveform data. *72nd EAGE Conference and Exhibition*, **A026**, Barcelona, Spain.

Trani, M. and Arts, R. and Leeuwenburgh, O. and Brouwer, J. and Douma, S. (2009). The importance of localization for the assimilation of 4D seismic

using the EnKF *79th SEG International Exposition and Annual Meeting*, pp: 3835-3839, Houston, Texas.

Trani, M. and Arts, R. and Leeuwenburgh, O. and Brouwer, J. and Douma, S. (2009). The value of the Streamline-based localization in the assimilation of 4D seismic data with the EnKF *71st EAGE Conference & Exhibition*, **R023**, Amsterdam, The Netherlands.

Leeuwenburgh, O., Peters, L., Trani, M., and Brouwer, J. (2008). The value of seismic data for production history matching. *71st EAGE Conference & Exhibition*, **E033**, Rome, Italy.

Trani, M. and Arts, R. J. and Leeuwenburgh O. and Brouwer J. H. (2008). Estimation of pressure and saturation changes from 4D seismic AVO and time-shift analysis. *71st EAGE Conference & Exhibition*, **E003**, Rome, Italy.

Arts, R. J. and Chadwick, R. A. and Eiken, O. and Trani, M. and Dortland, S. (2007). Synthetic versus real time-lapse seismic data at Sleipner CO_2 injection site. *77th SEG International Exposition and Annual Meeting*, pp: 2974-2978, San Antonio, Texas